Magnetic Imaging by Spin-Polarized Scanning Tunneling Spectroscopy Applied to Ultrathin Fe/W(110) Films

vorgelegt von
Oswald Pietzsch
aus Hamburg

Hamburg
2001

gewidmet Herrn Prof. Dr. Ulrich Gradmann

Inhaltsangabe

Die Erforschung immer kleinerer magnetischer Strukturen bis hinab zur atomaren Skala ist aktuell von großem wissenschaftlichen Interesse. Zugleich ist dieser Forschungszweig von höchster technologischer Bedeutung für die Entwicklung magnetischer Datenspeicher extremer Dichte sowie für die Erschließung des neuen Gebiets der Magneto-Elektronik. Die in der vorliegenden Arbeit vorgestellte magnetisch sensitive Mikroskopie-Methode der spin-polarisierten Rastertunnelspektroskopie ist ein neues, äußerst leistungsfähiges Forschungswerkzeug, dessen routinemäßiger Einsatz hier zum ersten Mal zusammenhängend dargestellt wird. In seinem räumlichen Auflösungsvermögen übertrifft das Verfahren die bislang eingesetzten Methoden höchstauflösender magnetischer Mikroskopie um zwei Größenordnungen.

Nach einer im Kapitel 1 gegebenen allgemeinen Einführung werden die theoretischen Grundlagen der spin-polarisierten Rastertunnelmikroskopie im Kapitel 2 dargestellt. Es folgt in Kapitel 3 eine eingehende Beschreibung des instrumentellen Aufbaus des speziell für magnetische Untersuchungen konzipierten Rastertunnelmikroskops. An dicken (50 Monolagen) und dünnen (7 Monolagen) Gd-Filmen, epitaktisch gewachsen auf W(110), werden erste Untersuchungen zur magnetischen Sensitivität des Mikroskops durchgeführt und wichtige Erkenntnisse hinsichtlich der Anisotropie ferromagnetisch beschichteter Tunnelspitzen gewonnen; dies wird in Kapitel 4 beschrieben. Zur Einführung in die Untersuchung des Systems nano-skaliger Eisenstreifen auf einem gestuften W(110) Substrat wird in Kapitel 5 ein Überblick über bereits publizierte Ergebnisse gegeben, auf die im Weiteren aufgebaut wird. Das System von Eisenstreifen wird dann im Kapitel 6 als Modell genutzt, an dem praxisnah der magnetische Kontrastmechanismus des Mikroskops erläutert wird. Mit einem auf höchste laterale Auflösung optimierten Verfahren wird das magnetische Domänensystem der Eisenstreifen sodann im Detail untersucht, das durch ein kompliziertes Wechselspiel widerstreitender Anisotropien auf der Nanometer-Skala bestimmt ist. Es wird sowohl die in der Filmebene liegende Magnetisierung von Fe-Streifen einer Dicke von lediglich einer atomaren Lage beobachtet, als auch die senkrecht zur Filmebene stehende Magnetisierung von Streifen, die zwei atomare Lagen dick sind. Diese Ergebnisse sind im Kapitel 7 dargestellt. Das Kapitel 8 ist Beobachtungen gewidmet, die am System der Eisenstreifen in variablen magnetischen Feldern erzielt wurden. Es konnte eine vollständige Hysteresekurve bestimmt werden; die der Hysterese zugrunde liegenden Prozesse werden im Detail beobachtet. Damit wird zugleich die wichtige Tatsache demonstriert, dass spin-polarisierte Rastertunnelmikroskopie auch in starken Magnetfeldern uneingeschränkt einsetzbar ist.

Abstract

The exploration of magnetic structures at an ever smaller – ultimately atomic – scale is currently a topic of great scientific interest. It is also of highest technological relevance in engineering extreme density magnetic data storage devices and developing the new field of magneto-electronics. In this present work spin polarized scanning tunneling spectroscopy (SP-STS) is introduced as a new, extremely versatile investigation tool. For the first time, its application on a routine basis is comprehensively demonstrated. Regarding spatial resolution, this method surpasses other high resolution magnetic microscopy techniques by two orders of magnitude.

After a general introduction given in Chapter 1 the theoretical foundations of SP-STM will be presented in Chapter 2. The instrumental setup of a scanning tunneling microscope, custom designed for the purpose of magnetic investigations, is described in Chapter 3. First results in the study of the microscope's magnetic sensitivity were obtained on thick (50 monolayers) and thin (7 monolayers) Gd films grown epitaxially on W(110). These measurements also provided important insights into the magnetic anisotropies of tunneling tips coated by ferromagnetic thin films and will be discussed in Chapter 4. As an introduction to the investigation of the system of nano-scale iron wires grown on a stepped W(110) substrate an overview of previously published results will be given in Chapter 5. Arrays of Fe nanowires will then be used in Chapter 6 as a model to discuss the practical application and the magnetic contrast mechanism of the microscope. Optimized for highest spatial resolution, the method will then be applied to a detailed study of the magnetic domain structure of the Fe stripes which are characterized at the nanometer scale by a complicated interplay of competing anisotropies. In Chapter 7 observations of stripes of single atomic layer thickness and stripes of two layers thickness are described, the magnetization being in the film plane for the former, and perpendicular to the film plane for the latter. Chapter 8 is dedicated to observations made on the array of Fe stripes in variable external magnetic fields. A complete hysteresis loop is presented, acquired at the nano-scale. Also, details of the remagnetization process like domain wall motion, domain creation and annihilation, are observed. These results highlight the important fact that SP-STS can routinely be applied in strong magnetic fields.

Contents

Chapter 1

Introduction

The quest for an understanding of magnetism at an atomic length scale is one of the current frontiers in condensed matter and materials science. Thanks to great advances in ultrahigh vacuum (UHV) technology and molecular beam epitaxy (MBE) techniques during the past decade it has become possible to study magnetism under the condition of reduced dimensionality, such as in ultrathin films of magnetic material, in nanowires, clusters, or even single adatoms on a surface. Magnetic materials of two, one, or zero dimensions exhibit a large number of surprising properties. These are of great interest for fundamental research. Although considerable experimental and theoretical progress has been achieved in the last few years the subject matter is mainly still in the field of basic research. In recent years the main driving force in this field, however, came from applied physics and technology. The demand for ever higher data storage and processing capacity intensified the worldwide request for nano-techniques that promise to be able to tailor magnetic materials exhibiting well defined properties. The discovery of the giant magnetoresistance effect (GMR) [1–3] a decade ago has initiated a vast amount of research activities, and it also had an enormous impact on technology related to magnetic data storage. It is a unique situation that, despite the fact that many riddles still have to be solved, the technological applications already have reached the mass market, the perhaps most prominent example being IBM's hard disk read head which is based on the GMR effect.

Currently, the data storage industry reports an increase in areal data density of 60 percent annually. While, for future systems, the spin information of a single atom is conceived the ultimate physical unit to magnetically store a bit of information, the next serious obstacle to soon be approached *technologically* is the superparamagnetic limit. Decreasing bit sizes lead to signal energies becoming so small as to be comparable with the ambient thermal energy, resulting in a decay of the stored magnetic signal. The lower limit for the magnetic grain size (which is equivalent to a switching unit) has recently been estimated to 600 nm^3 in volume, or ~ 10 nm lateral extent [4].

In general, GMR devices rely on multilayer stacks of magnetic and non-magnetic metallic ultrathin films of nanometer thickness, i. e. on *vertical* magnetic nanostructures. The study of *laterally* structured nanomagnetic systems of only one or zero dimensions was hampered in the past by a lack of an adequate magnetic imaging technique being able to provide a resolution that could hold pace with the reduction in size of the entities that can be produced in a controlled fashion (for an overview on the relevance of such structures see, e. g., [5]).

In this work I will present spin polarized scanning tunneling spectroscopy (SP-STS) as a new, extremely versatile imaging tool for the study of surface and thin film magnetism. The new method combines the well known capability of a scanning tunneling microscope (STM) to achieve highest spatial resolution with a sensitivity for the spin of the tunneling electrons. In this way SP-STS allows to correlate structural, electronic, and magnetic properties of a sample at an unprecedented spatial resolution.

To put SP-STS in perspective, a short review of other magnetic imaging methods currently in use is given in the following. The most widely applied experimental method in the study of ultrathin ferromagnetic films is based on the magneto-optical Kerr effect (MOKE). A beam of polarized light is directed onto the magnetic sample, and the rotation of the polarization in the reflected light reveals the magnetic properties. The method is easy to employ, provides a resonable surface sensitvity (at a penetration depth of ~ 20 nm) and is robust in an applied external magnetic field. The spatial resolution of MOKE microscopy, however, is ultimately limited to about 300 nm by the wave length of the probing light. It is clear that the received signal is an average over the respective surface fraction. MOKE has been employed in scanning near-field optical microscopy (SNOM) in order to circumvent this limitation. A lateral resolution of approx. 50 nm has been obtained so far [6]. MOKE is the method of choice to measure spatially averaged hysteresis curves of thin films.

Scanning electron microscopy with polarization analysis (SEMPA) is an ultra-high resolution magnetic imaging technique. A finely focused beam of electrons is scanned across the surface, and the spin polarization of the secondary electrons emitted from the sample is analysed. The lateral resolution limit depends only on the beam width; the signal intensities, however, get extremely small eventually. This method allows to measure all three magnetization components simultaneously. The surface sensitivity is very high (~ 1 nm probing depth), and the lateral resolution is about 20 nm up to-date [7,8]. It is a severe drawback of this technique that measurements in strong applied magnetic fields are, except for very special cases, not possible.

In Lorentz microscopy a transmission electron microscope (TEM) is used to measure the deflection of an electron beam due to the magnetic induction as the electrons traverse the film. The signal is an average over the film thickness, and stray fields above and below the sample also contribute

leading to a cancellation of the signal in certain geometries. Several modes
of application are used, e.g. the defocused or *Fresnel* mode, or the differen-
tial phase contrast (DCP) mode, the latter reaching a resolution better than
10 nm [9]. A review of the various modes of operation is given in [10] and
references therein.

Using photons for probing and also for signal detection has the great
advantage that large external magnetic fields can be applied to the sample.
This has been demonstrated at X-ray wave lengths by magnetic transmission
X-ray microscopy (MTXM) [11]. The method relies on the X-ray magnetic
circular dichroism (XMCD) as a contrast mechanism and is unique in that
it provides chemical sensitivity. Absorption rates at element-specific core
levels exhibit a dependence on the projection of the magnetization onto the
photon propagation direction in ferromagnetic samples. A lateral resolution
of ~ 25 nm has been reported recently [12].

A new versatile technique for magnetic domain observation has been
developed by a combination of X-ray magnetic linear dichroism (XMLD)
spectroscopy and photoelectron emission microscopy (PEEM) [13]. The ex-
cited secondary electrons give rise to the signal in the PEEM and provide
a spatial resolution of ~ 20 nm. The sampling depth of XMLD-PEEM is
about 2 nm. Recently, it has been shown [14] by a combined application of
the linear and circular dichroism effect and an X-ray source tunable in energy
that measurements on both sides of an interface consisting of ultrathin layers
of antiferromagnets and ferromagnets can be carried out opening the door
for a better understanding of the *exchange bias effect* which is of high tech-
nological relevance for tailoring the characteristics of magnetic properties in
magneto-electronic devices.

In magnetic force microscopy (MFM) the external magnetic stray field
of the sample is probed by a magnetic tip fixed to a flexible cantilever. Two
modes of operation are in use. Either the magnetic dipolar force exerted on
the tip by the sample stray field is measured via the cantilever deflection, or
the force gradient is measured by oscillating the cantilever at its resonance
frequency and detecting the shift in frequency due to the stray field interac-
tion. The lateral resolution achieved so far is about 20–50 nm [15,16]. This
method has reached a considerable degree of industrial applications since,
if moderate resolution is sufficient, it can be applied at ambient conditions.
For a higher resolution ultra-high vacuum (UHV) is required.

Pierce [17] expected a scanning tunneling microscope to be the ultimate
microscopical magnetic investigation tool if the tip itself is a source of spin-
polarized electrons. Scanning tunneling microscopy (STM) and its derivative
scanning force microscopy (SFM) are the only techniques available providing
real space images of surfaces at the ultimate, atomic resolution. After first
reports on spin-polarized vacuum tunneling by Wiesendanger *et al.* [18–20]
ten years ago using magnetic tunneling tips no substantial progress towards
nano-scale magnetic imaging was achieved for several years. Spin-polarized

STM (SP-STM) studies are still extremely rare up to-date. This is owed partly to certain technical difficulties (e.g. one needs a reliable *in situ* tip exchange mechanism in order to compare measurements taken with "normal" tips to those taken with spin polarized tips), but the main problem is to unambigiously discriminate magnetically caused contrasts from those caused by other features of the electronic density of states near the Fermi level. Apart from the instrumental problems just mentioned the question of assigning the observed contrasts in SP-STM images to magnetic properties of a sample is of a more fundamental nature. In general, only a small modification of conventional STM images due to spin polarization was anticipated. Applying the argument that the tunneling current is dominated by the delocalized but only weakly polarized s, p electrons, Himpsel *et al.* [5] expected an appreciable spin-polarized contribution only at rather short tunneling distances, i.e. at high tunneling currents where localized $3d$ states of high polarization gain weight. However, the authors already pointed to d-like surface states identified by Stroscio *et al.* [21] at Fe and Cr surfaces using an STM in the spectroscopic mode of operation. Indeed, when Bode *et al.* [22] succeeded in resolving the magnetic domain structure of thin Gd films they operated their SP-STM in the spectroscopic mode, and it was the well-known spin-split surface state of Gd that gave rise to the magnetic signal. As will be described theoretically in Chapter 2 and further illustrated by experimental results in Chapters 4-8, SP-STS can directly address such highly polarized features by selectively evaluating their density of states at a properly chosen energy. Making use of the *spin valve effect* one can measure locally the *differential conductance* dI/dU which will be different for a parallel or an antiparallel configuration of the magnetization of tip and sample. By mapping the dI/dU signal as a function of the lateral tip position an image of the magnetic domain structure of the sample can be obtained. In this way domain imaging has become possible at an unprecedented spatial resolution. Moreover, since the topography of the sample can be imaged in conventional constant current imaging mode simultaneously to the dI/dU map the structural, electronic and magnetic properties of the sample can be correlated at high precision. An example is displayed in Fig 1.1. There is one important conclusion that can be drawn at first sight from a comparison of a constant current image and a simultaneously recorded dI/dU map: while an effect of spin polarization is hardly measurable in many cases in the topographic image, the magnetic contrast is most obvious in the dI/dU map. This conclusion will be supported by numerous examples presented later in this work.

In recent years, three different experimental concepts have been applied to achieve spin-polarized vacuum tunneling. (i) Ferromagnetic thin film probe tips have been used in the early experiments by Wiesendanger *et al.* [18, 19] and more recently by Bode *et al.* [22] to map the local (differential) conductance changes for parallel ($\uparrow\uparrow$) or antiparallel ($\uparrow\downarrow$) spin con-

Figure 1.1: STM images of 1.5 ML Fe on a stepped W(110) single crystal. **(a)** Topographic image acquired in constant current mode, **(b)** simultaneously measured $\mathrm{d}I/\mathrm{d}U$ map. The contrasts in (b) reveal the magnetic domain structure of the sample which is invisible in (a). Tunneling parameters: $I = 300$ nA, $U = -300$ mV.

figurations of tip and sample exploiting the *spin valve effect*. (ii) GaAs has been used as sample or as tip material because of its optical polarization properties. Alvarado *et al.* [23] injected spin polarized electrons from a bulk ferromagnetic tip and measured the circular polarization of the recombination luminescence. Jansen *et al.* [24, 25] applied GaAs tips as a source of spin polarized electrons by optically pumping with circularly polarized light. (iii) Using an amorphous magnetic tip material of low coercivity in conjunction with a small coil wound around the tip Wulfhekel *et al.* [26, 27] rapidly switched the tip magnetization by applying a high frequency a.c. current to the coil and measured the differential magnetic conductance $\mathrm{d}I/\mathrm{d}m_\mathrm{t}$ using a lock-in technique.

The experimental results reported in this work were achieved following Bode's approach. While in one of the early spin-resolved experiments tips made from bulk ferromagnetic material have been used [20], here conventional non-magnetic tungsten tips carrying an ultrathin film of ferromagnetic material are applied mainly for the advantage of a much lower stray field exerted by the highly reduced quantity of magnetic material at the tip. In order to use such tips it is mandatory to have facilities available to prepare tips *in situ*, i.e. to clean them in UHV from oxide layers, to grow epitaxial films on them in a controlled fashion, and to insert a tip into the STM without breaking the vacuum. These requirements are far from being trivial to fulfill, and there are but a small number of experimental setups available wordwide – if any – that allow for such an arrangement. In Chapter 3 I will describe in detail how these problems have been resolved.

The starting point for the experimental part of this work will be in Chapter 4 a presentation of some early results obtained on Gd films grown on W(110) in two ranges of thickness. Films of 50 monolayers (ML) Gd served as a first test system for the general magnetic sensitivity of the new microscope. Next, results from a film of only 7 ML Gd will be described. It has been chosen because of its out-of-plane anisotropy, a situation particularly suited for observing the effect of an external magnetic field applied perpen-

dicular to the sample plane. Although this study remained incomplete due to certain experimental problems the results turned out later to be of great value in a rather unexpected way. It provided the freedom of choice with regard to the magnetic anisotropy of the tip, and this is the main reason to present the data here.

The main focus throughout this work will be on the magnetic domain structure of the system of 1.5 ML Fe grown on a stepped W(110) substrate which will be covered in Chapters 5-8. This system, for a number of reasons, provides an excellent model to demonstrate the power of SP-STS. First of all, a comprehensive corps of literature is available, the majority of the publications being connected to the work of Ulrich Gradmann and Hans-Joachim Elmers. Thanks to the long term work of their groups the general magnetic structure of ultrathin Fe films on W(110) is well known. A short review will be given in Chapter 5. It is an important prerequisite for a new method in order to establish its validity that it is able to reproduce earlier confirmed results. Albeit, as I will show in Chapters 6-8, there is much more to discover in a system as complex as this one. As a second reason, the typical magnetic domain widths of the Fe films are below the resolution limit of established domain imaging techniques but are in a range which is particularly suited for STM imaging.

The magnetic characteristics of 1.5 ML Fe/W(110) are determined by an in-plane magnetization for areas covered by just a single atomic layer of iron whereas areas covered by two atomic layers are magnetized out-of-plane. When grown on a vicinal W(110) substrate at elevated temperatures, the iron film forms a sytem of stripes extending along the tungsten step edges. From the available literature it is known that the magnetization in adjacent double layer (DL) stripes points alternatingly up and down due to dipolar coupling. It was the main goal of the current study to resolve this out-of-plane magnetic structure of the DL stripes, and it eventually showed up as a strong bright-and-dark contrast (cf. Fig 1.1(b)). While in Chapter 6 emphasis will be put on the details of the imaging process, Chapter 7 is dedicated to a discussion of the magnetic domain structure of the sample.

As an ultimate proof of the *magnetic* origin of the observed contrasts I will present images which were acquired from a sample exposed to a variable external magnetic field. Next to its unrivaled spatial resolution it is a particular strength of the SP-STS technique that it can be applied in strong magnetic fields. In Chapter 8 this feature will be demonstrated along a detailed study of the magnetization reversal in ultrathin magnetic nanowires. Based on information acquired at the nano-scale, a complete hysteresis loop can be extracted from SP-STM images. Moreover, the processes *behind* hysteretic behavior, i.e. domain wall movement, domain creation and annihilation are observed in detail.

The experiments on the double layer system of Fe nanowires proved extremely exciting, since when performing experiments in order to scrutinize

more closely a previous discovery we repeatedly ran into more unexpected effects of either the sample or, of equal importance, of the ferromagnetic tunneling tips. Experimenting with different coating materials for the tips had a dramatic influence on the obtained magnetic images. A variation of the magnetic tip anisotropy allowed to observe either *domains* or *domain walls*, and in certain cases of both simultaneously. Surprisingly, even bare non-magnetic tungsten tips can be used to observe magnetically caused phenomena. Examples will be presented in Chapter 8.

Can atomic resolution be achieved in spin polarized scanning tunneling experiments? Yes, it can. Surprisingly, it is the conventional constant current imaging mode in conjunction with a ferromagnetically coated tip that has provided the first atomically resolved images of an antiferromagnetically ordered Mn monolayer on W(110), verifying a ten years old theoretical prediction by Blügel *et al.* [28] on the existence of two-dimensional antiferromagnetism in monolayer films. In this system the magnetic orientation changes from one atom to its next nearest neighbor, and atomic resolution is a prerequisite in order to gain magnetic information at all since the magnetic moments cancel at any larger scale. It was my great pleasure to take part in this experiment, "discovering the grail of magnetic imaging", as Stefan Heinze coined it. It has been described in detail in Ref. [29] and more comprehensively in the recently published Ph.D. thesis of Heinze [30] whom the brilliant theory is owed that guided the experiment. On the experimental side, the ground had been prepared by an earlier careful study of the growth of ultrathin Mn films on W(110) by Matthias Bode and co-workers [31]. Once the preparation of magnetic thin film tips had been mastered on a routine basis the actual experiment was performed in a rather straightforward manner. It is a rare condition that both theoretical and experimental expertise combine in such a fruitful way in one group as was the case here. For a review of the experiment I refer the reader to the literature cited.

Many of the results that will be presented in this work deserve a deeper theoretical analysis. This task ought to be tackled from two sides: (i) Classical micromagnetic theory, based on a continuum approach, can be applied in order to describe theoretically the experimentally observed domain structures; (ii) *ab-initio* calculations based on the full-potential linearized augmented plane wave (FLAPW) method have recently been applied with great success to a host of magnetic systems [32]. This approach is very promising in that it addresses directly the spin resolved electronic structure of a sample and can directly be related to the process of SP-STM imaging.

Chapter 2

Theory of Spin Polarized Scanning Tunneling Spectroscopy

2.1 The Tunnel Effect

A convenient starting point for the theory of scanning tunneling spectroscopy is the effect of *tunneling* in one dimension like it is introduced in virtually all basic quantum mechanics textbooks. The effect to be described is a result of the wave-particle dualism which is unknown to classical physics.

If a particle of total energy E impinges upon a potential barrier of height V_0 and finite width s it will, according to the laws of classical physics, only be able to pass the barrier if E is greater than V_0, otherwise it will be reflected. If the particle is of microscopic dimensions as, e.g., an electron, it must be described in terms of quantum physics, and the result is completely different. Even for the case $E < V_0$ there is a certain probability to find the particle behind the barrier, and this phenomenon is known as *tunneling*. The most simple situation is a single particle, let's say an electron of kinetic energy E, incident from the left upon a one-dimensional potential barrier. The
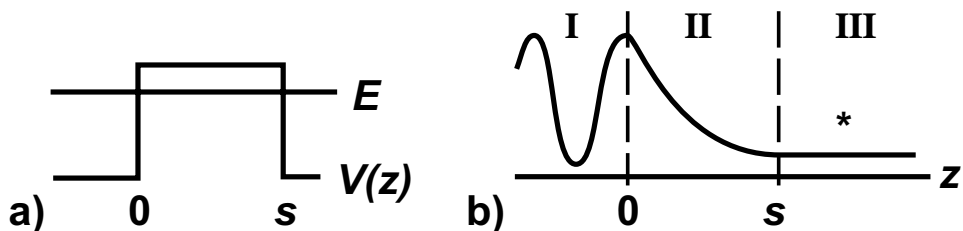
Figure 2.1: Schematics of a one-dimensional potential barrier.

9

potential can be written as follows

$$V(z) = \begin{cases} 0 & z < 0 \\ V_0 & 0 < z < s \\ 0 & z > s \end{cases} \qquad (2.1)$$

The electron is described by its wave function $\psi(z)$ which is a solution of the time-independent Schrödinger equation

$$\left(-\frac{\hbar^2}{2m} \frac{d^2}{dz^2} + V(z) \right) \psi(z) = E\psi(z). \qquad (2.2)$$

Here m is the electron mass, and $\hbar$ is Planck's constant divided by 2π. We can distinguish three regions (cf. Fig. 2.1): region I left of the barrier, $z < 0$, region II the barrier itself, $0 < z < s$, and region III right of the barrier, $z > s$. In the regions I and III $V(z) = 0$, and the electron wave function is that of a free particle, of the general form

$$\begin{aligned} \psi(z) &= Ae^{ikz} + Be^{-ikz} & z < 0 \\ \psi(z) &= Ce^{ikz} + De^{-ikz} & z > s \\ k &= \frac{\sqrt{2mE}}{\hbar}. \end{aligned} \qquad (2.3)$$

$A, B, C,$ and D are arbitrary constants. Inside the barrier, that is $0 < z < s$, $V(z) = V_0$, and the ansatz is

$$\begin{aligned} \psi(z) &= Fe^{ik'z} + Ge^{-ik'z} & 0 < z < s \\ k' &= \frac{\sqrt{2m(E-V_0)}}{\hbar}. \end{aligned} \qquad (2.4)$$

The total energy is negative in this region since $E < V_0$, thus k' is complex, and the exponents become real:

$$\kappa^2 = -k'^2 = \frac{2m(V_0 - E)}{\hbar^2}, \qquad (2.5)$$

therefore the exponentials are *real* functions describing waves which decay exponentially within the barrier.

In region I the general solution of the Schrödinger equation is a linear combination of a wave traveling to the right and a wave reflected at $z = 0$ traveling to the left which combine to a standing wave. At $z = 0$ the wave function penetrates into the classically forbidden barrier region II where it is exponentially damped but remains finite at $z = s$. In region III the transmitted wave travels to the right, and since no reflection occurs we can determine a first constant, $D = 0$. The overall wave function, in terms of its probability density $\psi^*\psi$, is depicted schematically in Fig. 2.1(b). The most important result obtained so far is the non-zero probability to find the electron behind the potential barrier.

$\psi(z)$ and also its first derivative $\frac{d}{dz}\psi(z)$ are required to be continuous for all z, and by matching the partial solutions found for the respective regions at the points $z = 0$ and $z = s$ (*wave matching method*) we can obtain a set of four equations that allows to determine the values for the remaining constants B, C, E, F in terms of A. This last constant can be chosen to normalize the wave function. Now we can gain an exact expression for the transmission coefficient, which is the ratio of the transmitted and the incident probability flux j_T and j_0, respectively:

$$T = \frac{j_T}{j_0} = \frac{1}{1 + (k^2 + \kappa^2)^2/4k^2\kappa^2 \sinh^2(\kappa s)} \tag{2.6}$$

In the limit of $\kappa s \gg 1$ this formula reduces to

$$T \approx 16\frac{k^2\kappa^2}{(k^2 + \kappa^2)^2} \exp(-2\kappa s) \tag{2.7}$$

When this last expression is a good approximation, T is extremely small. The most important result, however, is the exponential dependence of T on the width s of the potential barrier. It is this relationship that is exploited in the scanning tunneling microscope. It is the key to the extremely high resolution which allows for a study of conducting sample surfaces on a scale where individual atoms can be resolved.

2.2   The Tunneling Process in the STM

In an STM measurement a fine metallic tip is approached as close as a few Å ($1\text{Å} = 10^{-10}$ m) to the surface of a conducting sample. The tip is then scanned line by line across the surface by means of appropriate piezo-electric elements, and, with a small bias voltage applied, a tunneling current $I(U)$ can be measured which will, according to Eq. (2.7), vary exponentially as a function of the distance between tip and sample. This is an example of metal–vacuum–metal tunneling. The tunneling barrier between the two electrodes in this case is the vacuum gap.

Inside the metallic electrodes the electrons may be described in the free-electron-gas model. All electronic states are occupied up to the Fermi level (for simplicity, we assume a temperature of 0 K resulting in a sharp edge in the Fermi function, separating occupied and unoccupied states). The height V_0 of the insulating vacuum barrier is given by the work function ϕ of the metallic electrode, i.e. the energy required to extract an electron out of the surface into the vacuum. ϕ is a material parameter, and for simplicity we assume that tip and sample are made from the same metal thus having the same work function. The width of the barrier is given by the tip–sample distance. Without an applied bias voltage between the electrodes a tunneling of electrons can occur from the tip to the sample but also from the sample
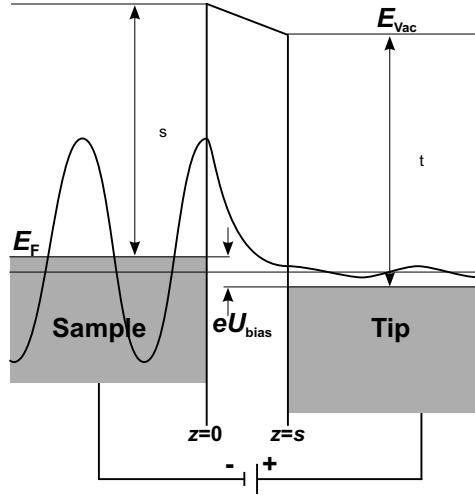
Figure 2.2: Schematics of the tunneling process in the STM. The barrier height is given by the work function of the electrodes, the barrier width corresponds to the tip–sample distance. An applied bias voltage U_{bias} shifts the Fermi levels of tip and sample relative to each other. Electrons can tunnel from the negatively biased sample to the tip. A change of bias polarity reverses the current direction. The sketch indicates the decay of a sample wave function in the barrier region.

to the tip, and the net tunneling current is zero. If we apply a small bias voltage U_{bias} between tip and sample the Fermi levels of the electrodes will shift accordingly with respect to each other (cf. Fig. 2.2). Now a tunneling current can flow. Throughout this work we will use the convention that the tip potential always is held grounded. Thus, for positive sample bias electrons will tunnel from occupied states of the tip into unoccupied states of the sample, and for negative sample bias the electrons come from occupied sample states and go to unoccupied tip states. Thus the direction of the current depends on the polarity of the applied bias voltage U_{bias}.

If we consider the limit of small bias voltage, i.e. $eU_{\mathrm{bias}} \ll \phi$, the energy of the tunneling electrons is approximately equal to the Fermi energy E_{F}. Inside the barrier the wave function of an electron decays:

$$\psi(z) = \psi(0)\exp(-\kappa z), \qquad \kappa = \sqrt{2m\phi/\hbar^2}, \qquad (2.8)$$

with κ the so-called *decay constant*. We can determine the probability density w of finding an electron at the tip position s by taking the square of the wave function:

$$w = |\psi(s)|^2 = |\psi(0)|^2 \exp(-2\kappa s), \qquad (2.9)$$

For a typical metal we may assume $\phi \approx 4$ eV. This results in a decay constant $\kappa \approx 1$ Å^{-1}. As a consequence, a given value of a tunneling current will be reduced by about 86 percent if the gap between tip and sample is

increased by 1 Å. These numbers illustrate the enormous vertical resolution that can be achieved by the STM. This feature allows to detect changes in the tip-sample distance of the order of 0.01 Å or less. Further, we can conclude from Eq. (2.8) the important fact that the tunneling current will be carried almost exclusively by the outermost atom at the tip apex while contributions from atoms of the next atomic layer within the tip crystallite can in most cases be neglected. Therefore, the tunneling process in an STM is highly localized in the sense that it occurs between one atom at the tip and the sample spot right below it. Thus, when scanned across a sample surface, the tip probes *local* properties of the sample with a lateral and vertical resolution that allows, in general, to resolve individual atoms.

Until now, we have considered tunneling only in the picture of a one-dimensional model. This model was sufficient to introduce some basic mechanisms that allow an understanding of the tunneling process in general. But already the term "local", introduced in the last paragraph, requires an explanation that can not be given based on this simple model. Furthermore, we did not discuss the properties of the probing tip at all. It was introduced just as a conducting electrode being located a distance s away from the sample surface. In most cases, our major concern will be the properties of the sample, and only in second place we want to know the tip. In an STM experiment, the ideal of a non-intrusive measurement would be a point probe with an arbitrarily localized wave function [33]. A realistic tip, however, is made from a certain material having its atoms at the apex arranged in a particular way, i.e. it has a certain geometry in space and a more or less extended wave function which will be different from that of a free atom but also from that of a solid. In other words, the tip has an electronic structure that has to be accounted for in a 3-dimensional approach.

In 1961, twenty years before the invention of the STM by Binnig, Rohrer and co-workers [34], in his investigation of the tunneling process between two planar electrodes separated by an oxide layer, Bardeen [35] developed an expression for the tunneling current, based upon time-dependent perturbation theory, that has since been used as a fundament to many fruitful approaches towards a theory of the tunneling process in the STM. Here, it is presented in the formulation of Tersoff and Hamann [33,36], adopted for a system of tip and sample separated by a vacuum barrier, and the limits of small bias voltage and low temperature are assumed. In this model the tunneling current is given by

$$I = \frac{2\pi}{\hbar} e^2 U \sum_{\mu v} |M_{\mu v}|^2 \delta(E_\mu - E_\mathrm{F}) \delta(E_v - E_\mathrm{F}), \qquad (2.10)$$

with e the electron charge, and the indices μ and v refer to the tip and the sample, respectively. The δ functions warrant that only elastic tunneling is considered, i.e. the energy of a tunneling electron is conserved. The central
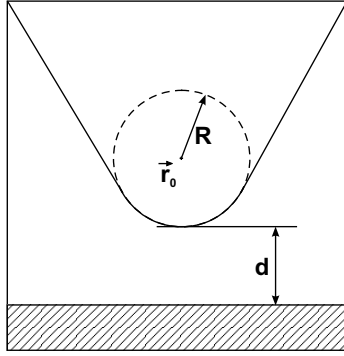
Figure 2.3: Model tip as introduced by Tersoff and Hamann [33]. The tip shape is arbitrary but spherical at its lower end. R is the radius of curvature, the center of curvature at $\vec{r}_0$. Distance of nearest approach to the sample surface (shaded) is d.

problem is the calculation of the tunneling matrix element $M_{\mu v}$ of the transition between states ψ_v of the sample before tunneling and ψ_μ of the tip after tunneling, and E_μ (E_v) is the energy of state ψ_μ (ψ_v) in the absence of tunneling. According to Bardeen, the matrix element is given by

$$M_{\mu v} = -\frac{-\hbar^2}{2m} \int d\vec{S} (\psi_\mu^* \vec{\nabla} \psi_v - \psi_v \vec{\nabla} \psi_\mu^*). \tag{2.11}$$

The integration has to be carried out over a surface which is located entirely within the barrier. In order to calculate the matrix element the energy levels and wave functions of both tip and sample need to be known. This requires a knowledge of their respective atomic structure. While, in general, this information will be (or can be made) available for the surface, it is almost impossible to know the details of the microscopic atomic structure of the tip since a tip is prepared in a relatively uncontrolled and nonreproducible manner.[1] However, some simplifying assumptions have been introduced that allowed to successfully interpret STM images qualitatively in a wide range of applications. Tersoff and Hamann proposed a model tip of arbitrary shape but with a lower end being a spherical potential well with a radius of curvature R, the center of curvature located at a position $\vec{r}_0$, the spherical tip a distance d above the sample surface, cf. Fig. 2.3.[2]

In the Tersoff-Hamann model, the simplest possible wave function for this tip is assumed, a spherical s-wave function while wave functions with an angular dependence ($l \neq 0$) are neglected. Now the matrix element can

---

[1] One way to obtain information on the tip's atomic structure is field ion microscopy (FIM). However, a spontaneous rearrangement of the tip apex atoms is not unusual during scanning, showing up as a change in imaging quality, leaving the experimentator again with a tip of unknown atomic structure.

[2] We recall that the tunneling current is carried almost exclusively by the one tip atom closest to the sample surface. This might intuitively suggest a spherical tip apex. In the Tersoff-Hamann model this case is considered the limit of smallest possible radius of curvature, i.e. a tip of maximum sharpness; the model is, however, not restricted to this case and applies, more generally, to any reasonable effective tip of radius R.

be evaluated and thus the tunneling current which is then proportional to

$$I \propto U n_{\mathrm{t}} \exp(2\kappa R) \sum_v |\psi_v(\vec{r}_0)|^2 \delta(E_v - E_{\mathrm{F}}), \qquad (2.12)$$

where U is the applied voltage, n_{t} is the constant density of states of the tip at the Fermi level. The quantity

$$n_{\mathrm{s}}(\vec{r}_0, E_{\mathrm{F}}) = \sum_v |\psi_v(\vec{r}_0)|^2 \delta(E_v - E_{\mathrm{F}}). \qquad (2.13)$$

is the *local density of states* (LDOS) of the surface at the Fermi level E_{F}, evaluated at the center of curvature $\vec{r}_0$ of the effective tip. The sample wave functions decay exponentially into the vacuum (the z direction is normal to the surface):

$$|\psi_v(\vec{r}_0)|^2 \propto \exp(-2\kappa s), \qquad (2.14)$$

and the tip–sample distance is defined by $s = d + R$. Furthermore, both the vertical and the lateral resolution of the STM can be shown to be determined by a characteristic length $L = [(d + R)/\kappa]^{1/2}$ [33,36,37].

The Tersoff-Hamann model leads to some remarkable results. The most important is that the tunneling current is determined by sample properties alone while the role of the tip is reduced simply to that of a probe. The most widely applied mode of STM operation makes direct use of this remarkable feature. In the *constant current mode* a feedback loop regulates the tip-sample distance $z = z_0 + \Delta z$ as to keep the tunneling current at a chosen set-point value while the tip is scanned across the sample surface. The values of the corrugation $\Delta z(x, y)$ can be plotted as a function of the lateral tip position (x, y). Constant-current STM images now can be interpreted as contour maps of constant sample LDOS, and to a first approximation these constant LDOS contours follow the topography of the sample surface. In this way the details of the surface geometry like step edges, islands, defects, surface reconstructions etc. can be made visible. After its invention the STM was most widely applied in the study of structural properties of surfaces. This new microscopy technique allowed to address questions that were previously not accessible by other surface sensitive methods which rely on the reflection of electromagnetic or matter waves at periodic structures.

However, the simple interpretation of the constant current data as a topographic image of the sample has to be used with some care. This is especially true when the level of atomic resolution is being approached. At this level the Tersoff–Haman model is still able to reproduce the lattice periodicity of close-packed metal surfaces but fails to reproduce the experimentally observed corrugation amplitudes if realistic tip radii and tunneling distances are assumed. This deficiency of the Tersoff–Hamann model is well understood; according to a theoretical model proposed by Chen [38] the experimental corrugation values can be explained by an inclusion of localized tip orbitals of

d_{z^2} symmetry. Chen's model also nicely fits another observation frequently made in atomic resolution experiments: during a scan at low tunneling resistance often a sudden drastic enhancement of the observed contrast can be noticed which, using Chen's picture, can be understood intuitively as a switching from an s-orbital to a d-orbital at the tip.

But also at a length scale greater than the surface lattice constant the topographic interpretation of constant current images requires some caution. Due to the local character of the probe the STM is sensitive to local variations in the electronic structure of the sample that may arise e.g. from the presence of adsorbates, alloying, or, in the case of ultrathin films, from different local coverages. Not in all cases these variations can be interpreted simply as a variation in height of the sample as is suggested by the constant current images. Different chemical species at a surface will exhibit different work functions. Certain adsorbates on top of a surface may even appear not as protrusions but as depressions giving rise to *anticorrugation*. This can often be observed for oxygen adatoms on metal surfaces. Any alteration of the local electronic structure will more or less modify the constant current image. What appears as a further complication at first sight, however, turns out as an opportunity to gain access to highly valuable information about the surface under study. It is the *local electronic structure* rather than the mere topography that is addressed by the *scanning tunneling spectroscopy* mode of STM operation, and as we will see later, this mode plays a key role in the process of magnetic imaging.

2.3   Scanning Tunneling Spectroscopy

Eq. (2.12) was derived in the limit of small bias voltage It can be written

$$I(\vec{r}_0, U) \propto eU \rho_s(\vec{r}_0, E_{\mathrm{F}}). \qquad (2.15)$$

In the range of a few millivolts the tunneling current is linearly proportional to the applied voltage U. For higher voltages, this is no longer true. The Ohmic behavior is replaced by a more or less complicated non-linear dependence $I = I(U)$. This is the result of the particularities in the electronic structure of the sample surface, the details of which can be studied locally by scanning tunneling spectroscopy. As will be shown next, curves of the differential conductance $\mathrm{d}I/\mathrm{d}U$ versus U reveal the LDOS structure within the probed energy range $E_{\mathrm{F}} \pm eU$.

In general, the effect of a finite bias voltage will be a distortion of the wave functions of both tip and sample, and also the energy eigenvalues will be modified, which is difficult to account for. Therefore, the undistorted zero-voltage wave functions and eigenvalues are usually taken as a first approximation [39]. Applying a bias voltage U then results in the Fermi levels of tip and sample being rigidly shifted with respect to each other by an

amount of $|eU|$, and any structure in the LDOS will be included in the shift. In this approximation the result of Tersoff and Hamann is modified to the energy integral

$$I \propto \int_0^{eU} n_{\mathrm{t}}(\pm eU \mp \varepsilon) n_{\mathrm{s}}(\varepsilon) T(\varepsilon, eU) \mathrm{d}\varepsilon, \tag{2.16}$$

where n_{t} and n_{s} are the densities of states of tip and sample, respectively, and all energies are taken with respect to E_{F}. Here, the energy and bias voltage dependence of the transmission coefficient T enters to account for the fact that the decay length κ depends on these parameters. T is given by

$$T(\varepsilon, eU) = exp \left\{ -2s \left[\frac{2m}{\hbar^2} \left(\frac{\phi_t + \phi_s}{2} + \frac{eU}{2} - \varepsilon \right) \right]^{1/2} \right\}. \tag{2.17}$$

Since, however, the increase of T with increasing bias is smooth and monotonic it appears as a background on which the LDOS structure information is superimposed [18].

If we assume $n_{\mathrm{t}} = \mathrm{const.}$ we yield from differentiating Eq. 2.16 with respect to U:

$$\frac{\mathrm{d}I}{\mathrm{d}U}(U) \propto n_{\mathrm{t}}(0) n_{\mathrm{s}}(eU) T(eU) + \int_0^{eU} n_{\mathrm{t}}(\pm eU \mp \varepsilon) n_{\mathrm{s}}(\varepsilon) \frac{\mathrm{d}T(\varepsilon, eU)}{\mathrm{d}U} \mathrm{d}\varepsilon. \tag{2.18}$$

The second term describes the background variation due to the bias voltage dependence of the transmission coefficient, and the bias voltage dependent LDOS structure can be attributed to the first term. The differential conductance $\mathrm{d}I/\mathrm{d}U(U)$ is the central quantity we are interested in when we perform an STS experiment. The details of the LDOS can be probed at high spatial resolution by varying the bias voltage. By choosing a fixed tip–sample separation and ramping the voltage between, e.g., $+1$ V and -1 V and measuring the $\mathrm{d}I/\mathrm{d}U(U)$ signal as a function of bias voltage we obtain a spectrum of the LDOS in the energy interval. An example is displayed in Fig. 2.4, revealing the characteristics in the electronic structure of ultrathin Fe films at three different coverages on a W(110) substrate.

There is, however, another effect related to the transmission coefficient that has to be taken into account which depends on the polarity of the applied bias voltage. This effect is illustrated in Fig. 2.5. When far away from each other, the Fermi levels of tip and sample are independent. When brought into tunneling contact they will acquire an equilibrium, i.e. the Fermi levels of tip and sample will eventually be equal. A bias voltage shifts the Fermi levels with respect to each other. At positive sample bias, tunneling will occur from occupied tip states into empty sample states (Fig. 2.5a), while at negative sample bias the flux is from occupied sample states into empty tip states (Fig. 2.5b). In both cases, electronic states close to the Fermi level of the negatively biased electrode will contribute most to the total tunneling
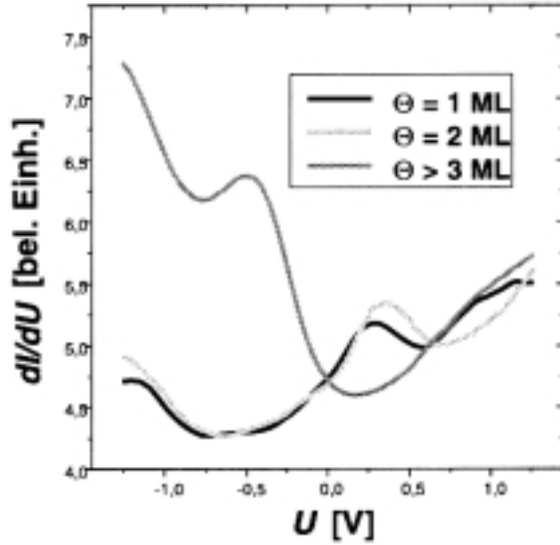
Figure 2.4: Tunneling spectra taken at sample locations exhibiting three different coverages of Fe/W(110) revealing maxima in the differential conductance at energies characteristic for the respective coverage regimes [40].

current, since these electrons "feel" a lower tunneling barrier height than electrons from states lying lower in energy. This is indicated in Fig. 2.5 by arrows of different size. This effect introduces an asymmetry in the measurement process when the polarity of the bias is changed: If, for example, we are interested in two features of the sample LDOS, one being energetically located at, say, +800 mV (unoccupied sample states) and the other at −800 mV (occupied sample states) with respect to the sample Fermi level, we can easily probe the feature having positive binding energy, since the tunneling process into the region of interest (RoI) is most effective at this bias. In order to probe the other feature we have to switch the bias polarity. Our region of interest now lies in an energetic range where tunneling is least efficient; instead, the spectral characteristics will be increasingly moulded by contributions which are due to *empty tip states*, and the assumption of a tip with an contourless electronic structure becomes increasingly questionable. But still the condition holds that the tip electronic structure will stay unaltered during a measurement while the sample LDOS features will vary as a function of lateral position (x, y), thus allowing in most cases to separate tip effects in the spectra as a constant background against the spatial variations of sample LDOS properties.

In general, there are a number of experimental procedures that can be applied for a spectroscopic measurement. The procedure used throughout this work is the following: Simultaneously to the recording of a constant current image a measurement of the local conductance $I(U)$ and the local differential conductance dI/dU is carried out. At every pixel the value $\Delta z(x, y)$ is measured, providing the data base for the constant current topography of the sample. Still positioned at the same pixel, the tip is then stabilized at preselected values for the bias voltage and the tunneling current (constant
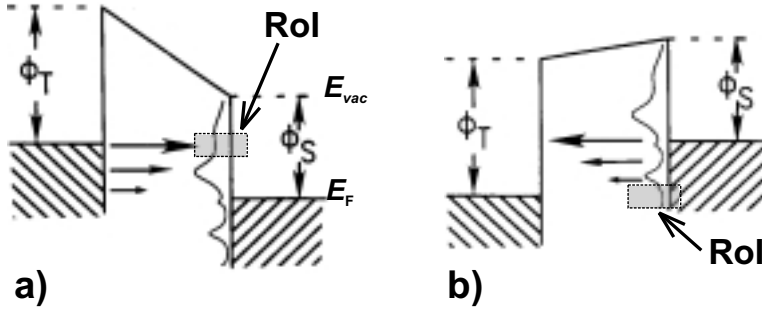
Figure 2.5: Schematics of the polarity effect of the transmission coefficient. The region of interest (RoI) is indicated by a shaded rectangle. **a)** At positive sample bias, unoccupied states of the sample are effectively probed. **b)** At negative sample bias, occupied sample states take part in tunneling. The region of interest, however, is now in a disadvantageous energetic range. Instead, unoccupied tip states gain weight (after Hamers [41]).

tunneling resistance U/I). Typical stabilization values used during the experiments are $U = 1$ V and $I = 300$ pA. The feedback loop is then switched off, and the voltage is ramped from, e.g. $+1$ V to -1 V while the tunneling current $I = I(U)$ is measured. From this curve the differential conductance $\mathrm{d}I/\mathrm{d}U$ can, in principle, be obtained by numerical differentiation. Since around $U = 0$ V the current becomes extremely small, the signal-to-noise ratio will be unsatisfactory. This problem can be circumvented by applying a lock-in technique: while ramping the d.c. voltage a small a.c. signal (~ 30 mV, $f_{\mathrm{mod}} \sim 1.8$ kHz) is added, and the in-phase current modulations, i.e. the $\mathrm{d}I/\mathrm{d}U$ signal, are detected by a lock-in amplifier. Signal variations due to noise are effectively filtered since they do not follow the constant modulation frequency and phase. The $\mathrm{d}I/\mathrm{d}U$ versus U curve then provides a spectrum of the LDOS. Since this measurement is carried out at every pixel the complete set of data provides a stack of spectroscopic layers $\mathrm{d}I/\mathrm{d}U(U, x, y)$. The spatial distribution of a spectroscopic feature of interest, for example a surface state peak characteristic for a certain coverage of a deposited thin film, can be plotted as a map of the differential conductance at the energetic position of this particular feature. This map can be compared to the simultaneously acquired topography, and structural and electronic properties can thus be correlated.

2.4 Spin Polarized Scanning Tunneling

So far, we did not consider the spin of the tunneling electrons. For ferromagnets, the electronic band structure is split into two subsets of bands, one

with majority spin ($\uparrow$) and the other with minority spin ($\downarrow$).[3] Due to the *magnetic exchange splitting* E_{ex} the minority spin band is filled less than the majority spin band. This imbalance, giving rise to the magnetic moment, shows up as a spin split density of states at the Fermi level. If the STM tip can be made sensitive to the spin of the tunneling electrons it should be an ideal tool for the investigation of magnetism at ultimate spatial resolution. One way to obtain a spin sensitive tip is to coat a regular tip with a thin film of a ferromagnetic material, e.g. Fe or Gd. In this case the tip exhibits a spin split band structure itself, and the interplay of the band structures should affect the tunneling probabilities of electrons as a function of the spin orientation.

2.4.1   Spin Polarized Constant Current Imaging

In his recent theoretical treatment of spin polarized scanning tunneling Heinze [30] generalized the Tersoff-Hamann model to the case of spin polarized tunneling. The DOS for both spin directions of the tip is assumed to be constant but of unequal value: $n_{\mathrm{t}}^{\uparrow} = \mathrm{const.}$, $n_{\mathrm{t}}^{\downarrow} = \mathrm{const.}$, but $n_{\mathrm{t}}^{\uparrow} \neq n_{\mathrm{t}}^{\downarrow}$. This allows to define $n_{\mathrm{t}} = n_{\mathrm{t}}^{\downarrow} + n_{\mathrm{t}}^{\uparrow}$ and $m_{\mathrm{t}} = n_{\mathrm{t}}^{\downarrow} - n_{\mathrm{t}}^{\uparrow}$ for the tip. Similar quantities can be defined for the sample, but again they depend on the tip position and the bias voltage:

$$\tilde{n}_{\mathrm{s}}(\vec{r}_0, U) = \tilde{n}_{\mathrm{s}}^{\uparrow}(\vec{r}_0, U) + \tilde{n}_{\mathrm{s}}^{\downarrow}(\vec{r}_0, U) \tag{2.19}$$

and

$$\tilde{m}_{\mathrm{s}}(\vec{r}_0, U) = \tilde{n}_{\mathrm{s}}^{\uparrow}(\vec{r}_0, U) - \tilde{n}_{\mathrm{s}}^{\downarrow}(\vec{r}_0, U), \tag{2.20}$$

where $\tilde{n}_{\mathrm{s}}(\vec{r}_0, U)$ is called the *integrated local density of states* of the sample, and $\tilde{m}_{\mathrm{s}}(\vec{r}_0, U)$ its *integrated local spin density of states*. In terms of these quantities the tunneling current can be expressed as follows:

$$I\left(\vec{r}_0, U, \theta(\vec{r}_0)\right) \propto \underbrace{n_{\mathrm{t}} \tilde{n}_{\mathrm{s}}(\vec{r}_0, U)}_{non-spinpolarized} + \underbrace{m_{\mathrm{t}} \tilde{m}_{\mathrm{s}}(\vec{r}_0, U) \cos\theta(\vec{r}_0)}_{spinpolarized}. \tag{2.21}$$

The right hand side now contains the sum of two terms, a contribution which is not spin polarized, I_0, and a contribution which depends on the relative spin orientation of tip and sample, I_{P}, and, in order to obtain a magnetic contrast, it is desired to maximize I_{P} over I_0. Since, in general, tip and sample will not share the same magnetization axis, the cosine of the angle θ between the magnetization directions of tip and sample enters. Whereas the magnetization direction of the tip $\vec{M}_{\mathrm{t}}$ can be assumed fix in most cases the sample magnetization $\vec{M}_{\mathrm{s}}(\vec{r}_0, U)$ may change as a function of position, and accordingly the angle between them is a function of the lateral tip position,

---

[3]The argument is not restricted to ferromagnets but holds for any magnetic material exhibiting a long range magnetic order. This order can be that of an antiferromagnet, a ferrimagnet, a spin density wave or a non-collinear spin structure.

$\theta = \theta(x, y)$. This allows to investigate the magnetic domain structure of the sample via the variation of the spin dependent part of the tunneling current. It is obvious that the spin polarized contribution is maximal for a collinear configuration $\vec{M}_{\text{t}} \| \vec{M}_{\text{s}}$, i.e. $\theta = 0$ for the parallel case ($\uparrow\uparrow$) or $\theta = \pi$ for the antiparallel case ($\uparrow\downarrow$), while it vanishes for $\vec{M}_{\text{t}} \perp \vec{M}_{\text{s}}$, i.e. $\theta = \pi/2$. For a collinear or a perpendicular configuration the total tunneling current can be conveniently given in terms of the contributing spin channels:

$$
\begin{array}{rcll}
I(\vec{r}_0, 0) & = & I_{\uparrow\uparrow}(\vec{r}_0) + I_{\downarrow\downarrow}(\vec{r}_0) = I_p(\vec{r}_0) & (2.22) \\
I(\vec{r}_0, \pi) & = & I_{\uparrow\downarrow}(\vec{r}_0) + I_{\downarrow\uparrow}(\vec{r}_0) = I_{ap}(\vec{r}_0) & (2.23) \\
I(\vec{r}_0, \pi/2) & = & 1/2[I_{\uparrow\uparrow}(\vec{r}_0) + I_{\downarrow\downarrow}(\vec{r}_0) + I_{\downarrow\uparrow}(\vec{r}_0) + I_{\uparrow\downarrow}(\vec{r}_0)] & \\
& = & 1/2[I_p(\vec{r}_0) + I_{ap}(\vec{r}_0)]. & (2.24)
\end{array}
$$

The decomposition of the density of states into a spin averaged and a spin polarized part, Eq. (2.21), allows to define the *polarization* of tip and sample in terms of these quantities:

$$
\begin{array}{rcll}
P_{\text{t}} & = & m_{\text{t}}/n_{\text{t}} & (2.25) \\
\tilde{P}_{\text{s}}(\vec{r}_0, U) & = & \tilde{m}_{\text{s}}(\vec{r}_0, U)/\tilde{n}_{\text{s}}(\vec{r}_0, U), & (2.26)
\end{array}
$$

and the polarization of the entire tunneling junction consisting of sample, vacuum gap, and tip, is given by the product of the polarizations of both electrodes:

$$
P_{\text{ts}} = P_{\text{t}} \cdot \tilde{P}_{\text{s}}(z, \vec{r}_{\|}, U). \tag{2.27}
$$

Note that the sample polarization depends also on z since the decay rates for s, p and d electrons may differ.

In constant current imaging, two effects have to be considred that lead to a degradation of magnetic contrasts. First of all, the non-polarized part of the tunneling current I_0 increases monotoneously with increasing bias voltage while the polarized part I_P may stay constant; thus the constant current image will in most cases be dominated by I_0 [42]. Second, the sample polarization $\tilde{P}_{\text{s}}$ is an energy integrated quantity evaluated in the energy interval selected by the chosen bias voltage. As a consequence, the polarization $\tilde{P}_{\text{s}}$ may be degraded by an inclusion of states exhibiting a polarization of opposite sign. This effect is schematically illustrated in Fig. 2.6(a-d) along a fictitious spin split density of states. (b) and (c) represent $\tilde{n}_{\text{s}}$ and $\tilde{m}_{\text{s}}$ as defined in Eqs. (2.19) and (2.20), respectively, and (d) symbolizes the resulting polarization $\tilde{P}_{\text{s}}$ which repeatedly changes sign in the interval $E_{\text{F}} - eU$. This may even lead to a complete cancellation of the spin polarized part of the tunneling current, thus preventing the extraction of any magnetic information from the sample. Due to the described problems the constant current mode is not a powerful method in imaging magnetic domain structures at the nanometer scale; as will be shown in the next section and illustrated
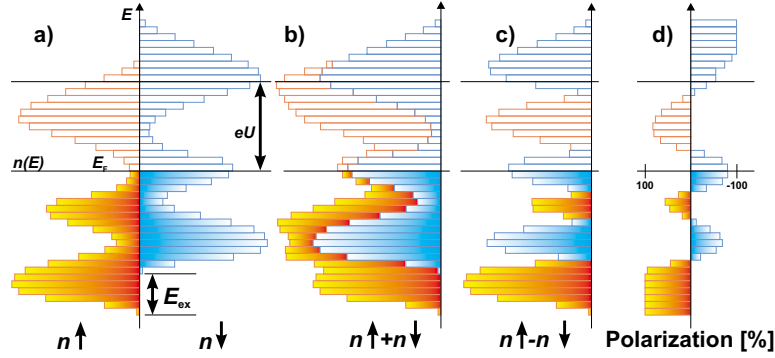
Figure 2.6: **(a)** Schematic illustration of the spin split density of states at the Fermi level. Majority and minority spin states are shifted by an amonut E_{ex}. **(b)** Total DOS $n^\uparrow + n^\downarrow$. **(c)** Difference of majority and minority DOS, $n^\uparrow - n^\downarrow$. **(d)** Polarization $P(U)$ as a function of bias.

by numerous examples throughout the remainder of this work, a method derived from a spectroscopic approach is more appropriate for this task.

However, constant current magnetic imaging has recently been applied with great success to magnetic imaging at the ultimate, atomic length scale by resolving for the first time the 2-dimensional nearest-neighbor antiferro-magnetic order of a single monatomic layer of Mn grown on W(110) [30]. Such a system of chemically identical but magnetically inequivalent atoms is particularly challenging since the total magnetization is zero and the magnetic information can be found exclusively at the atomic length scale. Thus atomic resolution and magnetic sensitivity is required simultaneously. The contrast mechanism in this case relies on the fact that the 2-dimensional translational symmetry of the magnetic superstructure is lower than that of the chemical surface unit cell which leads to a strong enhancement of the spin polarized contribution to the tunneling current [30, 42]. Constant current imaging has a great potential in the study of periodic magnetic structures at the ultimate length scale.

2.4.2   Spin Polarized Scanning Tunneling Spectroscopy

For high contrast studies of magnetic domain structures it is necessary to know the energetic ranges of high polarization within the density of states structure. This knowledge can be obtained by applying the spectroscopic mode of the STM. Differentiating Eq. (2.21) yields the spin polarized differential conductance,

$$\frac{\mathrm{d}I(U)}{\mathrm{d}U} \propto n_{\mathrm{t}} n_{\mathrm{s}}(\vec{r}_0, E_{\mathrm{F}} + eU) + m_{\mathrm{t}} m_{\mathrm{s}}(\vec{r}_0, E_{\mathrm{F}} + eU) \cos \theta(\vec{r}_0). \qquad (2.28)$$

From comparing Eq. (2.28) to Eq. (2.21) we note the essential difference [42]: in the former the tunneling current is governed by the energy integrated
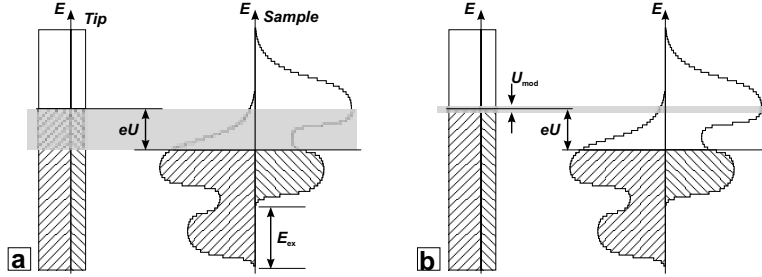
Figure 2.7: Probing the spin split density of states. **(a)** Constant current measurement. All states in the interval $[E_{\mathrm{F}}, E_{\mathrm{F}} + eU]$ contribute to the signal, indicated by the gray-shaded area. Polarization effects may be degraded or even cancelled. **(b)** Spectroscopic measurement. The dI/dU-signal is acquired at $E = eU$ as indicated by the narrow gray-shaded area. The energy resolution is determined by the amplitude of the a.c. modulation voltage ΔU_{mod} of the lock-in amplifier.

quantities $\tilde{n}_{\mathrm{s}}$ and $\tilde{m}_{\mathrm{s}}$ which are central to the constant current mode, while in the latter the differential conductance is directly proportional to n_{s} and m_{s} at an energy $E_{\mathrm{F}} + eU$. In constant current imaging the non-spin polarized contribution I_0 increases with U while the spin polarized contribution I_{P} may stay constant. On the other hand, in a $\mathrm{d}I/\mathrm{d}U$ measurement the voltage can be adjusted as to maximize the spin polarized contribution m_{s} over the spin averaged contribution n_{s}. The energetical positions of such ranges of high polarization can be extracted from spectral curves measured on oppositely magnetized sample locations. Thus, the spectroscopic approach is particularly suited to image the magnetic domain structure of a sample by selectively probing features of the LDOS exhibiting a high spin polarization. A schematic illustration of the two modes of SP-STM application is given in Fig. 2.7.

Making use of Eqs. (2.25) and (2.26) we can rewrite Eq. (2.28) as follows:

$$\frac{\mathrm{d}I(U)}{\mathrm{d}U} \propto n_{\mathrm{t}}(U) n_{\mathrm{s}}(\vec{r}_0, E_{\mathrm{F}} + eU)[1 + \cos\theta(\vec{r}_0) P_{\mathrm{t}}(E_{\mathrm{F}} + eU) P_{\mathrm{s}}(\vec{r}_0, E_{\mathrm{F}} + eU)].$$
(2.29)

The tilde of P_{s} has been dropped since this quantity is no longer energy integrated. We have reintroduced the bias dependence of the tip related quantities $n_{\mathrm{t}}(U)$ and $P_{\mathrm{t}}(U)$ to account for the fact that in a spectroscopic measurement the limit of small bias voltage will, in most cases, not be given. Recalling the discussion of the polarity effect on the transmission coefficient on p. 17 we can expect that any structure of the tip DOS will be particularly noticeable in the negative sample bias range. For a ferromagnetic tip its DOS structure may include highly polarized features that show up at certain bias voltages. Since the contrast required to study the magnetic domain structure of a sample depends on the *total* polarization of the tunneling junction which is given by the product $P_{\mathrm{t}} P_{\mathrm{s}}$ such features can readily be used for imaging.

An extrapolation of a value for the sample polarization is, however, not straight forward without additional information.

Chapter 3

Instrumental Setup

We have endeavored in designing an STM which is extremely stable and which meets three operational conditions: ultra-high vacuum, low temperatures, and high magnetic fields [43]. For the purpose of our special interest in investigations in surface magnetism we have supplied the instrument with some unique features, like sample rotation, easy tip exchange mechanism, and an arrangement for MOKE measurements. In this chapter I will describe the instrument in detail.

3.1 The Cryo STM

3.1.1 Chamber system

The new cryomagnet-STM chamber is added to a four-chamber UHV system [44] consisting of a central distribution chamber, a preparation chamber equipped with resistive and electron beam heating and a sputter gun, an MBE chamber with five evaporators and a home built STM especially designed for time resolved growth studies described elsewhere [49], an analysis chamber containing facilities for standard surface characterization as, e.g. low energy electron diffraction (LEED), Auger electron spectroscopy (AES) and spin-resolved photoelectron spectroscopy (SP-PES), and, within an additional satellite chamber, a commercial variable-temperature STM [45] which can be operated in a temperature range of 30 K $< T <$ 1000 K. A load lock allows for fast introduction of samples and tips without venting the chamber system. To prevent from acoustical and low frequency building vibrations the whole system is installed in an acoustically shielded laboratory with a foundation being completely separated from the rest of the building. The UHV chamber system is supported by a table with additional pneumatic damping.

3.1.2   Magnet Cryostat System

Magnet

The magnet cryostat system (Fig. 3.1) is a modified Spectromag ^{4}He bath cryostat with a LN$_2$ radiation shield [46]. The 2.5 T superconducting magnet is a split coil type with a 62 mm bore. Homogeneity of the field in a 10 mm diameter spherical volume at the sample location is specified to 1 part in 10^2. The maximum sweep rate accounts to 2.5 T per minute. The central region of the magnet (cf. Fig. 3.2) has two cutaways of 80° and 90°, respectively, and a minimum height of 42 mm thus providing two access openings to the microscope. Samples and tips are being exchanged through the 80° window whereas the 90° window is used to carry out magneto-optical Kerr effect (MOKE) measurements, and to allow for metal or molecular beam evaporation onto the sample surface. To obtain proper UHV conditions the magnet is designed to safely endure bakeout at 120° C. In our bakeout procedure we keep the magnet at 115° C for 48 h. The temperature is measured by a platinum resistor sensor on top of the magnet. The signal of this sensor feeds a control unit that supplies a flow of cold nitrogen gas across the magnet if the temperature is about to surpass the set point value. Thus a safe bakeout operation is guaranteed over night.

Cryostat and UHV Chamber

 The helium reservoir of the cryostat has a useful capacity of 20 l giving a hold time in the low temperature regime of approx. 40 h between subsequent fills. The helium reservoir and the magnet are enclosed by a nitrogen radiation shield. Its 20 l volume provides a hold time of 36 h. At the lower end where the magnet has its above mentioned openings the shield has an additional rotating cylinder the purpose of which is to shut the access windows. This cylinder is thermally coupled to the main part of the shield by a number of copper braids. To avoid vibrations due to boiling nitrogen the LN$_2$ reservoir is pumped to a pressure $p < 5$ mbar so that the nitrogen solidifies. To cope with the initially huge amount of gas from the boiling liquid we use a rotary vane pump with a nominal pumping speed of 65 m^3/h. When the nitrogen has solidified at a temperature of 63 K the rate of exhaust gas is greatly reduced so that a much smaller pump can be used to hold the pressure. This pump is located in an adjacent room which is acoustically isolated from the STM laboratory. As the gas flow through the pumping line is very low we have no acoustic coupling of the pump. Having a radiation shield at a temperature as low as 63 K is of considerable advantage for minimizing the helium boil off.

   The outer vacuum chamber of the cryostat unit has a DN 350 CF base flange which fits onto the appropriate top flange of our custom-made UHV chamber. Pumping is done by a turbo pump, an ion getter pump and a
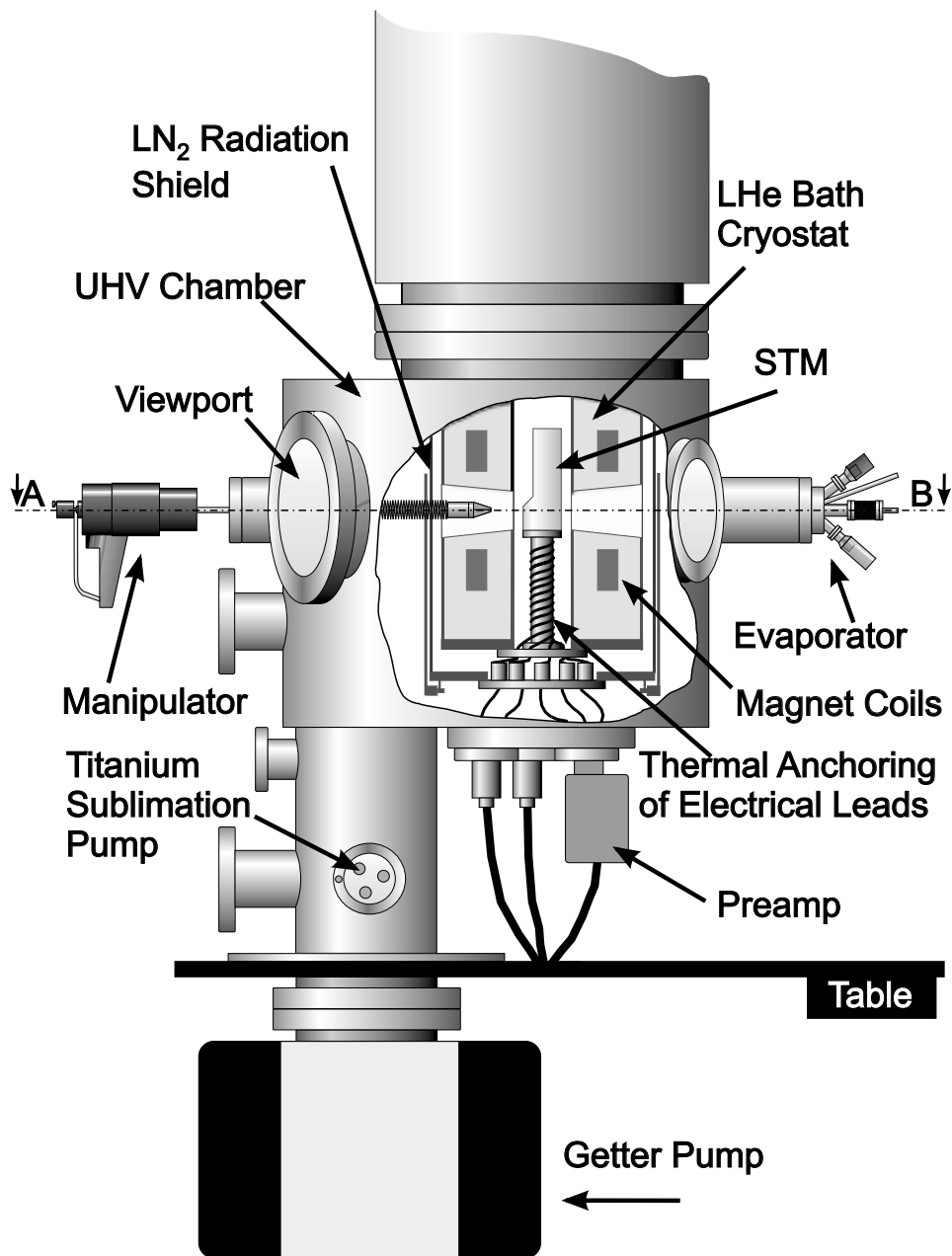
Figure 3.1: (a) Schematic drawing of the cryomagnet STM system (side view). The STM is inserted from the bottom through the base flange which also carries the electrical feedthroughs. For section A—B see Fig. 3.2.
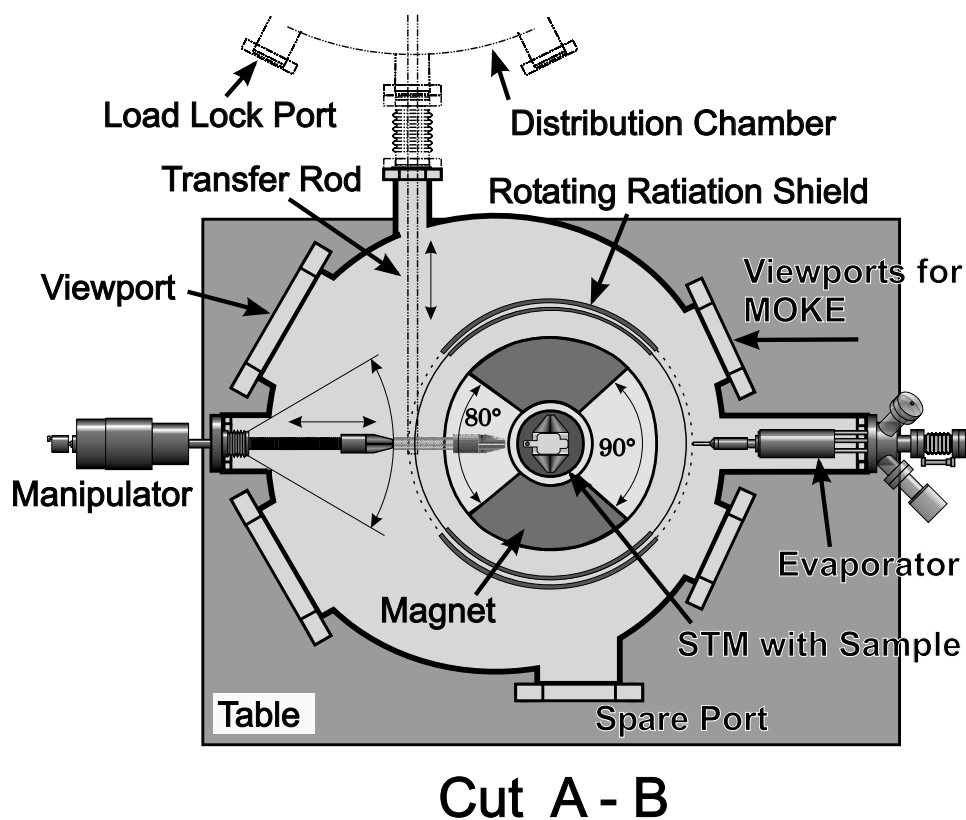
Figure 3.2: Section of the cryomagnet system at the sample plane.

titanium sublimation pump. The base pressure after bakeout and cooldown is $< 5 \times 10^{-11}$ mbar. The turn-around time for venting the system from low temperature, bake-out, and returning to low temperature accounts to several days. Thus it is essential that samples and tips can be introduced through the load-lock of the central distribution chamber without breaking the vacuum.

3.2   STM Design

The design of the STM was geometrically restricted by the 62 mm diameter of the magnet's core tube. The cylindrical body of the STM, machined from one piece of the glass ceramic Macor [47] has a diameter of 40 mm and a height of 110 mm. This body bears all parts of the microscope. It is mounted on top of an OFHC copper pedestal which serves both as the microscope's support and as the thermal anchoring for all electrical wirings. Together with this stand the microscope is installed as a unit into the magnet bore (cf. Fig. 3.3). To avoid any disturbance of the magnetic field the few metallic parts used are made from titanium, molybdenum, copper, or copper
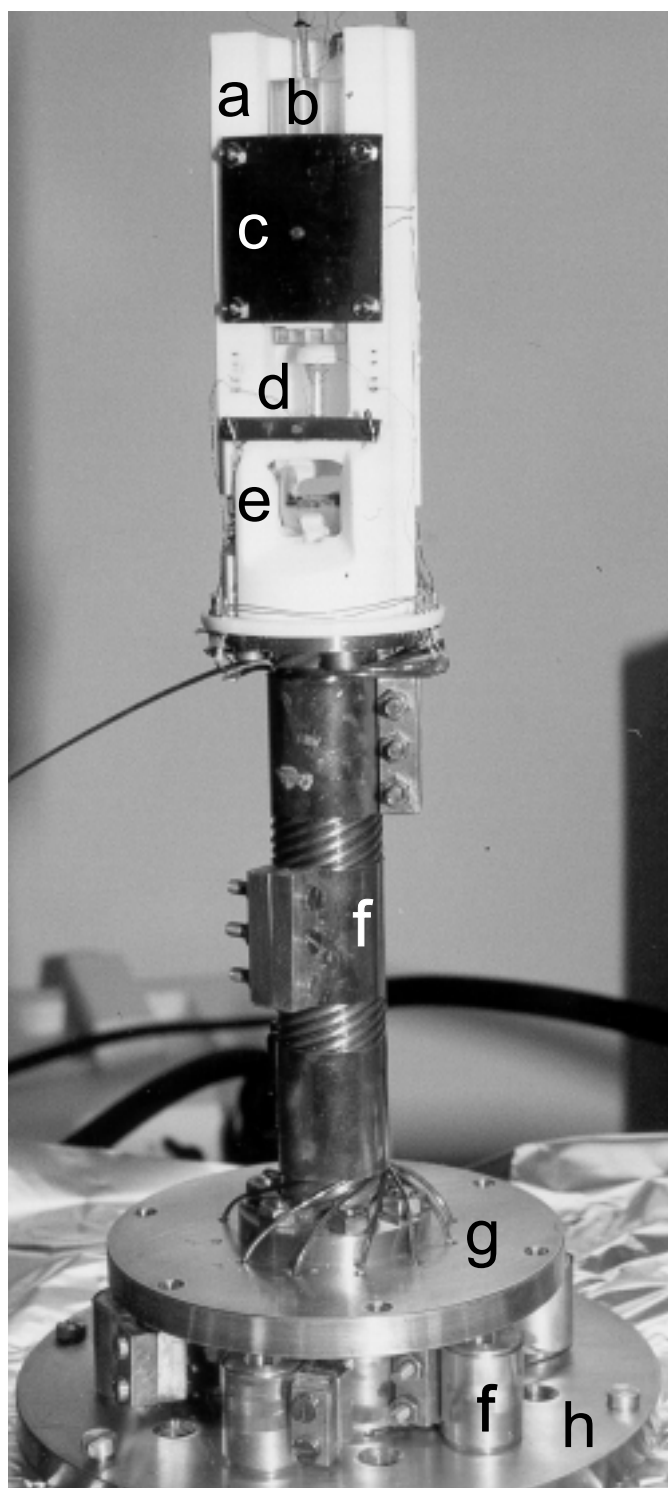
Figure 3.3: Photograph of the microscope on its pedestal. (a) Macor body, (b) sapphire prism, (c) leaf spring, (d) tube scanner with tip, (e) sample, (f) thermal anchoring of electrical leads to helium and nitrogen temperature, respectively. When mounted to the cryostat the helium flange (g) and the nitrogen flange (h) are mechanically disconnected.
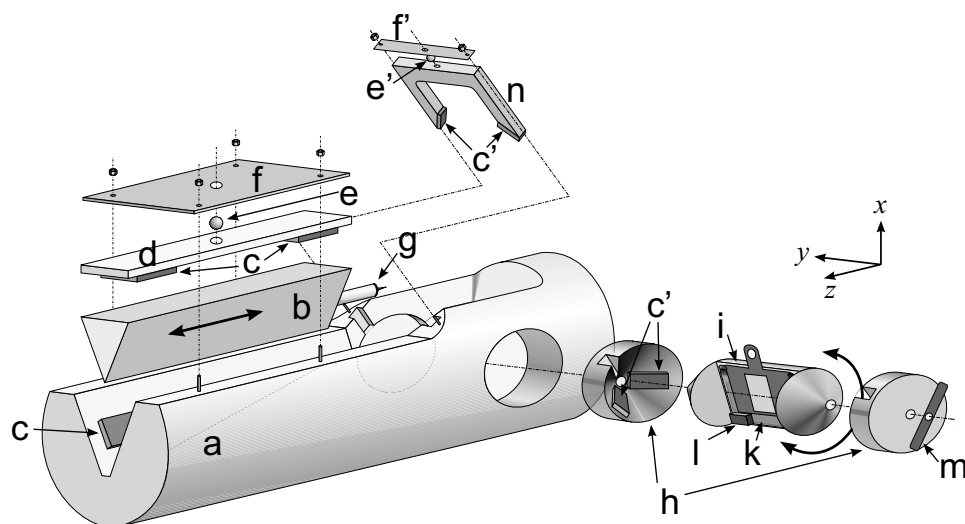
Figure 3.4: Schematic drawing of the STM (not to scale). (a) Macor body, (b) sapphire prism, (c) and (c') shear piezo stacks, (d) Macor beam,(e) and (e') ruby ball, (f) and (f') leaf spring, (g) scanner with tip, (h) stators for sample rotation, (i) rotor with sample, (k) spring, (l) temperature sensor, (m) leaf spring, (n) bridge.

beryllium.

3.2.1   Approach Mechanism

At the center of the microscope one finds two moving parts, the approach sledge bearing the scanner tube at its lower end [(b) in Fig. 3.4], and the sample recectacle (i) which can be rotated about the y-axis. The coarse approach mechanism is based on Pan's design [48] that has proven to be stable enough to regain a microscopic location on the sample with an accuracy of less than 100 nm posterior to a macroscopic movement of 20 mm [49,50]. The approach sledge is a polished sapphire prism placed in a V-shaped groove where it is rigidly clamped by two triplets of shear piezo stacks [51] [(c) in Fig. 3.4]. A 5 mm × 5 mm × 1 mm Al_2O_3 pad is glued on top of each shear piezo stack. These pads provide the actual contact areas between the stacks and the sapphire prism surfaces. Two of the piezo stacks are glued to a Macor beam (d) which is pressed onto the prism by means of a molybdenum leaf spring (f) and a ruby ball (e). The Macor beam functions as a balance and thus warrants an equal distribution of the spring force to all contact areas of the six shear piezo stacks and the prism surface. In contrast to previously presented designs [52–54] we do not employ walker stepping as a working mechanism but use inertial movement by applying an asymmetric saw-tooth voltage curve to all six stacks simultaneously (stick-slip). On the flat slope of the voltage ramp the prism follows the shear movement (stick) while, due to its inertial mass, it is unable to follow the rapid relaxation of

the piezos on the steep slope (slip), the result being one step of the prism per period. The mechanism is driven at 0.5–1 kHz; the step size can be tuned by varying the applied voltage amplitude. The scanner containing the tip is mounted to the lower end of the prism. The tip approach towards the sample to less than 0.2 mm distance is carried out manually using a remote control box; this operation can easily be controlled visually through one of the viewports with an *ex situ* located optical microscope. Only the fine approach is accomplished in automatic mode of the STM control unit. During a measurement the sapphire prism stays firmly clamped to the microscope body. The scanner in use is a 1/4" EBL #4 piezo tube [51] with a length of 31 mm. This length was chosen in order to allow for a scan range of 5 μm at low temperatures (10.5 μm at room temperature) and still having a sufficiently high resonance frequency ($f_{\mathrm{res}} = 2.2$ kHz). A great scan range is desirable for imaging of magnetic domains.

3.2.2 Sample Rotation

The sample is introduced into a receptacle [(i) in Fig. 3.4] which can be rotated by more than $270°$ about the y-axis. This rotor is a sapphire cylinder with the edges ground off to form two $90°$ cones. These cones are polished and again serve as the surfaces for stick-slip movement. In close analogy to the arrangement described above for the linear movement there are six shear piezo stacks (c') two of which are pressed onto the cones by a bridge (n) with a leaf spring (f'). Due to the symmetry of this assembly it is self-centering in both radial and axial direction, and no additional bearings are required. When brought into place and turned for the first time the rotor, shaken by the rapid oscillatory piezo movements, takes on an equilibrium position and keeps it. Between the two cones a recess is ground into the cylinder deep enough to receive the sample tray such that the sample surface lies in the $x - y$-plane. The sample tray is kept in place by a copper beryllium spring (k). The gap voltage to the sample is applied through a contact soldered to the spring. Also, the sample temperature sensor (l), a GaAlAs diode [55], is glued onto the spring, and is thus in immediate proximity and in excellent thermal contact to the sample.

The capability to rotate the sample allows for some unique experimental arrangements, illustrated in Fig. 3.5. While the sample receptacle is in position (a) (i.e. the sample surface normal pointing in $+z$ direction) and the tip retracted, sample and tip exchange can be carried out. With the tip approached, this is also the position for STM measurements. After retraction of the tip a $90°$ rotation can be applied to the sample, thus turning the surface normal into the $-x$ direction [position (b)]. This position allows to direct a molecular beam from the evaporator (cf. Fig. 3.1 and Fig. 3.2) to impinge normal to the sample surface. The sample re-rotated back into position (a), STM imaging can, in principle, be applied for time resolved growth
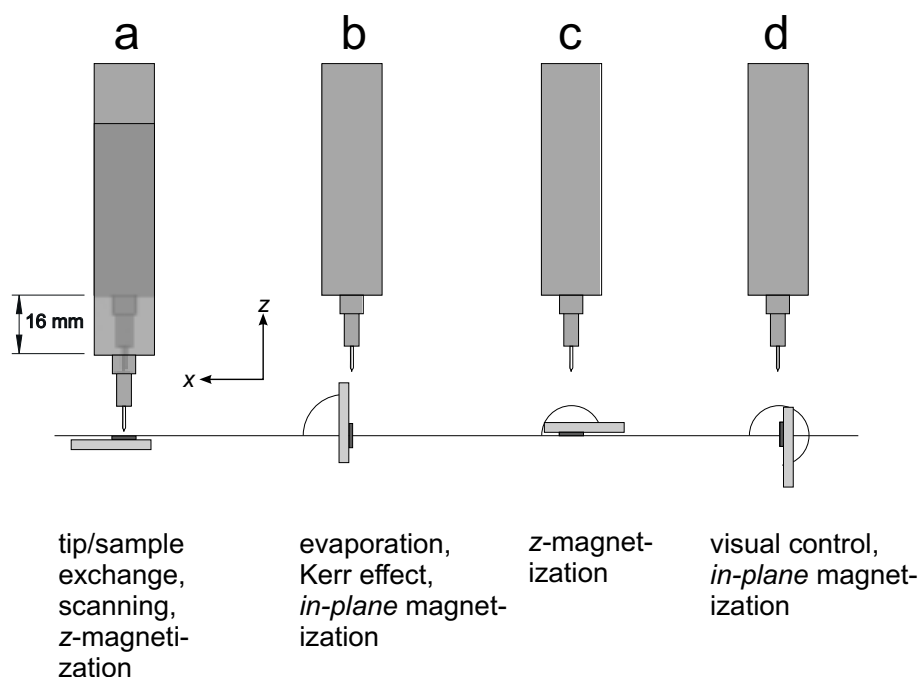
Figure 3.5: Principal geometrical configurations of the sample. For details on the particular use of each position see text.

studies at low temperature and, if desired, in a magnetic field. Position (b) also allows for measurements of the magneto-optical Kerr effect (MOKE). The UHV chamber is supplied with two viewports at the appropriate sites (see Fig. 3.2), one for the incident beam, the other for the reflected beam.

Sample Magnetization

Though the external magnetic field vector at the sample location is restricted to the z direction, the sample can be magnetized in almost any appropriate direction by virtue of the rotor. If in-plane magnetization is desired this can be achieved by turning the sample into position (b) or position (d), respectively. Out-of-plane magnetization is accomplished in position (a) and position (c). This latter configuration provides a very elegant way to study certain surface magnetic phenomena: Suppose a ferromagnetic sample being in position (c), and the external field is applied in, e.g., the $+z$ direction. Having a ferromagnetic tip in use, both tip and sample will be magnetized according to the applied field. Now the field is switched off, and the sample is rotated by 180° into the scanning position, i.e. position (a). Tip and sample will now be in an *antiparallel* magnetic orientation. After taking a measurement *in remanence* the field is switched on again. The magnetization orientation of the tip will stay the same. The sample, however, will experi-
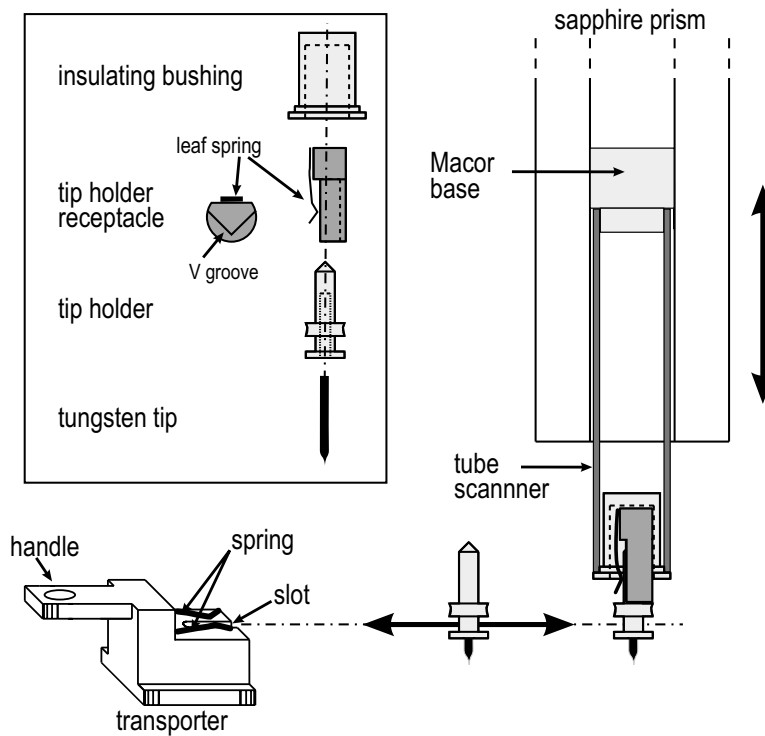
Figure 3.6: Schematic drawing of the tip exchange mechanism. Drawing from Ref. [56].

ence a reorientation of its magnetization, tip and sample magnetization thus ending up in a *parallel* configuration. With the external field switched off, again a measurement *in remanence* can be taken. Since, for the field sweep, the tip does not need to be retracted the second scan will image exactly the same location on the sample surface, thus allowing a one-to-one comparison of the two measurements.

3.2.3 Tip Exchange Mechanism

When working with ferromagnetically coated tips it is mandatory to have the possibility to prepare and exchange tips *in situ* in a short turn-around time. We use etched tungsten tips coated with 5–10 ML of Fe or Gd. A typical tip preparation procedure is as follows. The tungsten tip is cleaned by heating it to $T > 2000$ K by means of electron bombardment in the preparation chamber. Iron coating and subsequent annealing is performed in the MBE chamber. The tip has then to be introduced into the microscope. While a normal W or PtIr tip can repeatedly be sharpened by field emission and thus can be kept in the microscope for periods of months this is not possible for a tip carrying an ultrathin magnetic film. Thus a tip exchange

mechanism is indispensable. Figure 3.6 shows the assembly schematically. The tip is fixed in a molybdenum tip holder. For inserting a tip into the scanner the tip holder is carried by means of the transporter which can be placed into the sample receptacle where it is positioned such that the tip holder ends up precisely below the retracted scanner. Driving down the linear motor lets the tip holder slip into a V–shaped groove of the tip receptacle which is mounted inside an insulating bushing within the lower end of the scanner tube. A small leaf spring clamps the tip holder. Now the transporter can be retracted, leaving holder and tip firmly attached to the scanner tube. Tip and sample exchange is carried out using a "Mechanical Hand" [57] which allows simple and safe operation. Tip exchange comes down to a matter of minutes, sample exchange being even faster. A whole tip preparation procedure, including fresh coating, accounts to less than one hour.

3.2.4   Electrical Connections

Since electrical leads introduce heat to the microscope special attention has to be paid to an optimum of thermal anchoring of all wirings. The leads for the magnet current supply, level meters, and temperature sensors are fed through the top side of the cryostat. They are effectively cooled by the flow of cold helium gas. The microscope wiring, however, is fed directly into UHV via several multipin feedthroughs at the bottom flange of the outer vacuum chamber (see Fig. 3.1). We use custom made Capton insulated shielded twisted pair VA steel cables with an overall diameter of 1 mm. They are thermally anchored to both the nitrogen and the helium stage (cf. Fig. 3.1 and 3.3). At the nitrogen stage every single lead is wound around a copper pole ten of which are mounted on top of a flange and thereby fixed to the base flange of the nitrogen shield. Anchoring to helium temperature is achieved in a similar way: a ten gear thread is cut into the microscope's pedestal such that all ten leads can be firmly wound around it, being held in place by appropriate clamps. When installed, the nitrogen and the helium flange are mechanically disconnected. For maintenance works they get coupled so that they form a unit with the microscope on top. Mounting and dismounting requires approx. 1/2 h.

3.3   Performance

3.3.1   Micro Positioning

Due to the very high stability of both the linear and the rotational drive one can regain a microscopic location on the sample after a macroscopic movement. This feature is illustrated in Fig. 3.7. The series of images was taken *ex situ* on Au(111)/mica in alphabetical order as indicated. Some islands of

characteristic shape are shown which can easily be distinguished. After each scan the tip was retracted by 16 mm, followed by a rotation of the sample by 90°, re-rotation of the sample, and re-approach of the tip. The images have been taken without any correction of the scan position. The maximum lateral offset during subsequent scans was found to be $\Delta(x, y) < 280$ nm, and $\Delta(x, y) < 425$ nm during 7 cycles.

3.3.2 Atomic Resolution

Figure 3.8 shows atomic resolution obtained in UHV on a terbium film grown *in-situ* on W(110). The dark sites are caused by adsorbates from the residual gas, probably CO. A profile along the line indicated is shown below the image. The resolution achieved in spite of the great scanner length highlights the stability of the whole microscope setup.
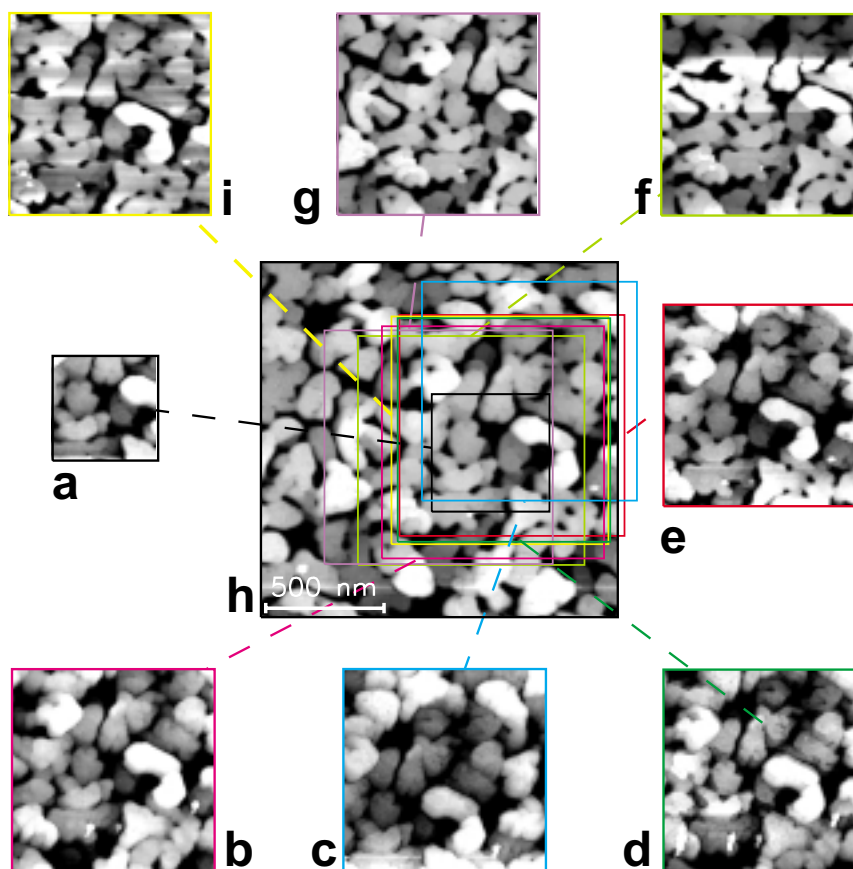
Figure 3.7: Sequence of images in alphabetical order demonstrating the microscope's ability to regain a microscopic location after a macroscopic movement. Au(111)/Mica, ambient condition. Each scan was followed by a retraction of the tip by 16 mm, rotation of the sample by 90°, re-rotation of the sample, re-approach of the tip. Maximum lateral offset during subsequent scans $\Delta(x, y) < 280$ nm, maximum lateral offset during 7 cycles $\Delta(x, y) < 425$ nm.
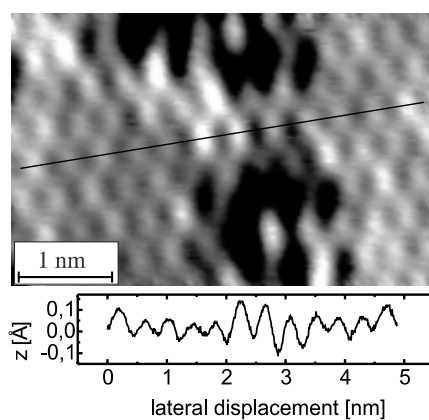
Figure 3.8: Atomic resolution on Tb(0001)/W(110) at $T = 16.8$ K. The profile below the image is taken along the line indicated.

Chapter 4

Preparatory Studies on Gd(0001)/W(110)

In the development of an STM-based magnetic imaging technique the Gd(0001) surface played an important role. This rare earth element is ferromagnetic below its bulk Curie temperature of 293 K. It exhibits a well known surface state which is spin-split, with both spin parts close enough to the Fermi level to be accessed by scanning tunneling spectroscopy. This surface state has been investigated by photoemission spectroscopy [59–62] and inverse photoemission spectroscopy [59,63,64] as well as STS [58,65,66] with consistent results. In a pioneering experiment Bode *et al.* [22] imaged the magnetic domain structure of a 50 ML Gd(0001) film on a W(110) substrate. By this experiment the feasibility of their specific approach was clearly demonstrated. Two ingredients were essential: the use of tips carrying a ferromagnetic thin film, and an application of scanning tunneling spectroscopy. It was thus an obvious thing to start the experiments in the new instrument by picking up the baton with gadolinium.

4.1 Thick Films

To begin with, it was necessary to show that the tunneling current *does not change* under the impact of an applied external magnetic field when a non-magnetic tip is in use, and that it *does change* when the tip is ferromagnetically coated. For this purpose a smooth 45 ML Gd(0001) film was prepared on a W(110) substrate. The preparation procedure is as follows: The W(110) single crystal is cleaned from carbon contaminants by repeated cycles of prolonged heating in an oxygen atmosphere ($T = 1200$ K, $p = 5 \times 10^{-6}$ mbar) and frequent short flashes to a temperature $T = 2300$ K by means of electron bombardment to remove oxide layers. Gd is then evaporated at room temperature at a rate of approx. 1.1 ML min^{-1} from a tungsten crucible heated by electron bombardment. Subsequent annealing of the sample at
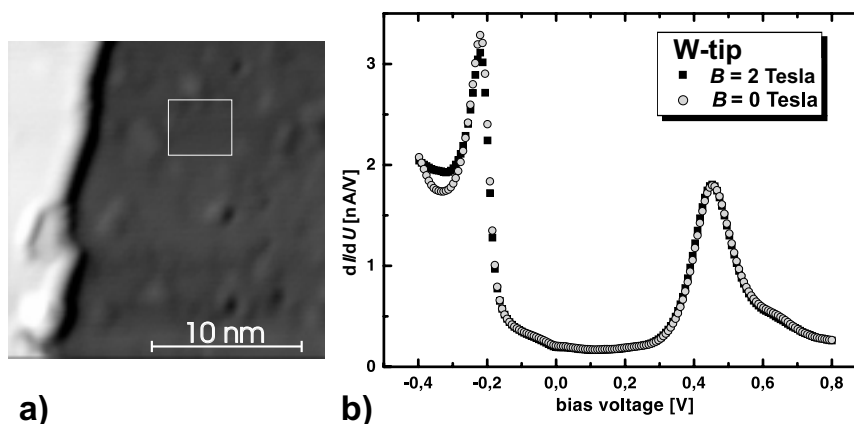
Figure 4.1: **a)** Topography and **b)** spectroscopy of 45 ML Gd(0001)/W(110) as measured with a bare tungsten tip in order to control the impact of an external magnetic field. The box in **a)** indicates the 4 × 5 pixels included in the averaged spectra. The exchange split Gd surface state shows up as two peaks (majority and minority spins). Black squares: 2 Tesla applied; grey circles: 0 Tesla (i.e. in remanence). No significant change of the spectra due to the magnetic field is observed.

a temperature $T = 710$ K for 10 min results in a smooth film exhibiting monatomic steps.

In a first step a bare tungsten tip was used for data acquisition. In a simultaneous measurement at a temperature of $T = 16.9$ K topographic, $I(U)$ and $dI(U)/dU$ data were obtained, see Fig. 4.1. The measurements were carried out with no magnetic field, i.e. in remanence (grey circles in Fig. 4.1(b)), and then with a field of 2 Tesla applied perpendicular to the sample surface (black squares in Fig. 4.1(b)). Since, for the field sweep, the tip is not required to be displaced, in both measurements exactly the same location on the sample is imaged. This facilitates a direct comparison of the two measurements. Both parts of the well known spin-split surface state appear as pronounced peaks in the spectra at -220 mV (majority spin part) and $+450$ mV (minority spin part), respectively. The spectra show neither a deviation nor a significant change in intensity due to the external field. This can be taken as a first clue that a non-magnetic tip gives a spin-averaged spectrum and is thus insensitive to the magnetic conditions.

In a second step the experiment was repeated with a clean tungsten tip coated with approx. 100 ML Fe.[1] The sample was prepared in a similar

---

[1]Bode *et al.* had shown in Ref. [22] that a tip coverage of this thickness is likely to cause stray field induced interactions with the domain structure of the Gd film, which is, in general, not desired. At the early stage of experiments with the new instrument described here, however, it was not the main goal to investigate any details of the sample, but to make absolutely sure that the tip had a ferromagnetic coating and to gain some first experience of the microscope's behavior in a strong external magnetic field.
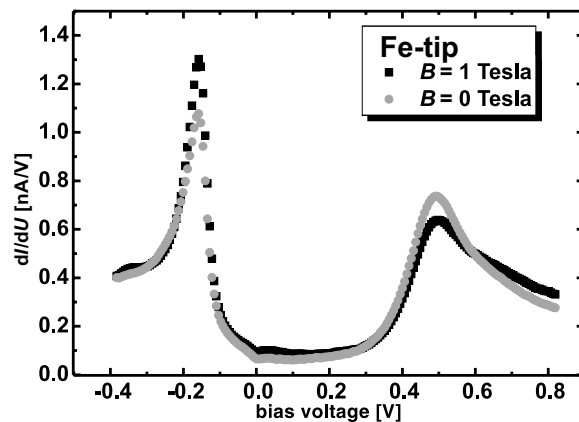
Figure 4.2: 50 ML Gd(0001)/W(110) as measured with a Fe covered tungsten tip. Black squares: 1 Tesla applied; grey circles: 0 Tesla (i.e. in remanence). The intensity of the majority peak is enhanced at the expense of the minority peak.

way, with a slightly higher coverage of $\theta = 50$ ML Gd. Fig. 4.2 shows two curves of the differential conductivity dI/dU. Again grey circles show the spectrum with no field applied, i.e. in remanence, and black squares indicate the spectrum taken with a magnetic field applied (this time $B = 1$ Tesla). With the Fe-tip in use, a clearly visible effect of the magnetic field can be observed in the spectra. The magnetization of tip and sample is forced into a parallel configuration. In the spectra, the signature of this arrangement is an increased intensity of the occupied part of the surface state which is enhanced by 22 percent at the expense of the unoccupied part which is attenuated by 12.5 percent. There is no energy shift of the peaks due to the magnetic field.

A similarly prepared sample was investigated by Kerr effect measurements. For this purpose the sample was rotated by 90° (position b in Fig 3.5) so that the magnetic field could be applied parallel to the sample plane. The Kerr signal was measured in the transverse geometry, i.e. the field is applied perpendicular to the plane of incidence of the light beam. Fig. 4.3 shows
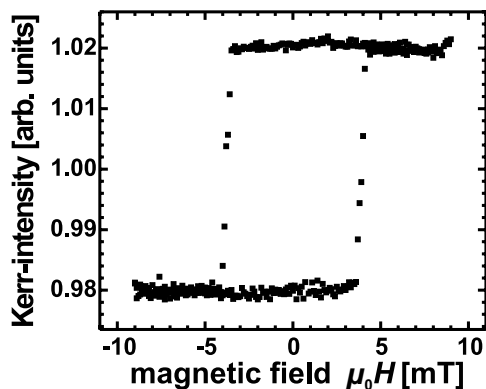
Figure 4.3: Kerr effect measurement of a 50 ML Gd(0001) film on W(110). The external field is applied parallel to the plane of the sample, perpendicular to the plane of light incidence (transverse geometry). The curve shows a typical easy-axis loop.

an easy-axis Kerr loop measured on 50 ML Gd(0001)/W(110) confirming its
in-plane anisotropy.

4.2   Ultrathin Films

Encouraged by the thick film results the next aim was to investigate a system
which better allowed to exploit some of the special features of our instrument,
in particular the combination of the external magnetic field and the ability
to rotate the sample. A sytem exhibiting out-of-plane anisotropy appeared
particularly suited. In the literature a few hints were available [67,68] that
Gd films on W(110) exhibit reorientation transition to a perpendicular easy
axis at a thickness below $\theta \approx 9$ ML at low temperatures (cf. Fig. 4.4).

The idea was to study spectroscopically a parallel as compared to an
antiparallel tip-sample magnetic configuration. The measurements brought
about some surprising results that will be reported on in the remainder of
this chapter. At a later stage, the conclusions drawn from these results
turned out to play an important role for a further development of the mag-
netic imaging technique based on spin polarized tunneling. Unfortunately,
although the chosen system proved very promising, the investigations had
to be interrupted at an early stage due to growing experimental difficulties,
and a number of interesting questions remain open. For some reason we
had to face an increasing contamination of the Gd films that progressively
prevented a growth of clean, well ordered Gd films. Though hardly visible
in the topographic images, the spatially resolved spectroscopic data revealed
local inhomogenities in the electronic structure, supposedly due to atoms of
an unknown species, possibly buried below the Gd surface. There is reason
to believe that the contaminants were Fe atoms. The spectra shown in the
following figures are acquired at locations where the Gd surface state was
fully developed, and since it is one of the characteristics of surface states
to be extremely sensitive to contaminations, this seems to indicate that the
data are reliable. However, though the conclusions drawn with regard to the
anisotropy of ultrathin Gd films proved very successful, it remains highly
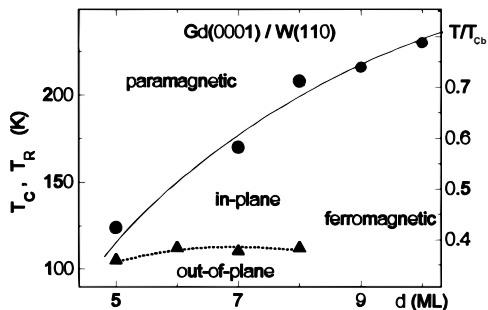
Figure 4.4: Magnetic phase diagram of
Gd/W(110) ultrathin films, indicating a
reorientation transition from in-plane to
out-of-plane magnetization at low tem-
peratures. (Diagram from Ref. [67]).

desirable to revisit the Gd ultrathin film system in order to clarify if the
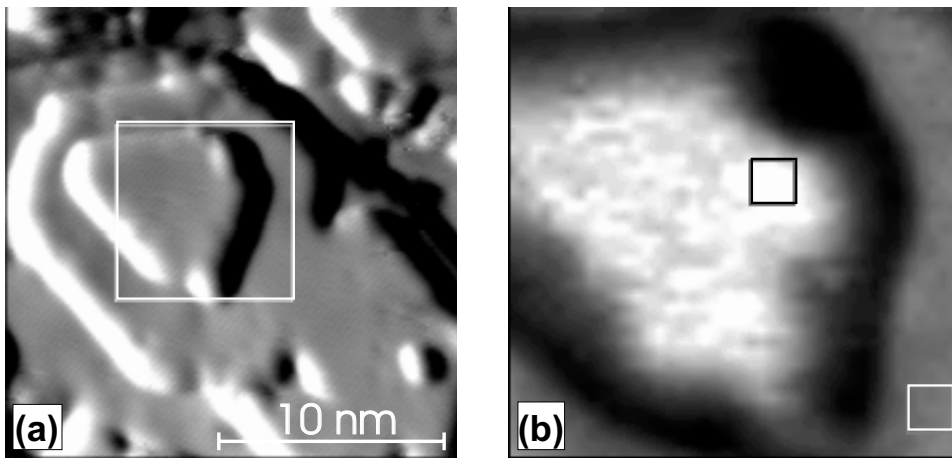
Figure 4.5: **(a)** Topographic image of the Gd(0001)/W(110) film (differentiated for clarity) at a nominal thickness of 7 ML. The local thickness of the two topmost terraces is 9±1 and 10±1 ML. **(b)** dI/dU map ($U = -200$ mV) of the area indicated by a box in **(a)**. The small boxes on the upper and lower terrace, respectively, highlight the exact locations where the spectra shown in the following figures have been averaged.

observed anisotropy may be influenced by contamination or alloying.

For the measurements, a clean tungsten tip was coated with approx. 10 ML Fe. A 7 ± 1 ML thick Gd(0001) film was prepared on the W(110) substrate. After inserting the sample into the microscope it was turned upside down by means of the rotational motor. In this geometry tip and sample were magnetized in an external field of $B = 1$ Tesla, and then the sample was turned face up. The plan was to perform a first measurement of the now supposed *antiparallel* configuration, then to apply the field again without turning the sample in order to achieve a *parallel* configuration, and then perform a second measurement. The Fe film at the tip is known to exhibit an easy magnetization axis parallel to the sample plane which is, of course, disadvantageous for this type of experiment. However, the expectation was to find at least a non-vanishing remanent out-of-plane *component* at the tip after exposing it to the strong external field.

Figure 4.5(a) shows a 20 nm × 20 nm constant current image of the topography (slightly differentiated for clarity). It displays a landscape of terraces each of monatomic height. Note that the vertical scale is much smaller than the lateral scale, greatly exaggerating the apparent corrugation. The box indicates the exact area investigated by high resolution spetroscopic measurements. A dI/dU map of this 7 nm × 7 nm area at a voltage of -200 mV is shown in Fig. 4.5(b). On both the upper and the lower terrace small boxes of a 20 × 20 pixels size have been marked to indicate the area of averaging of the spectroscopic curves shown in Figs. 4.6 and 4.7.
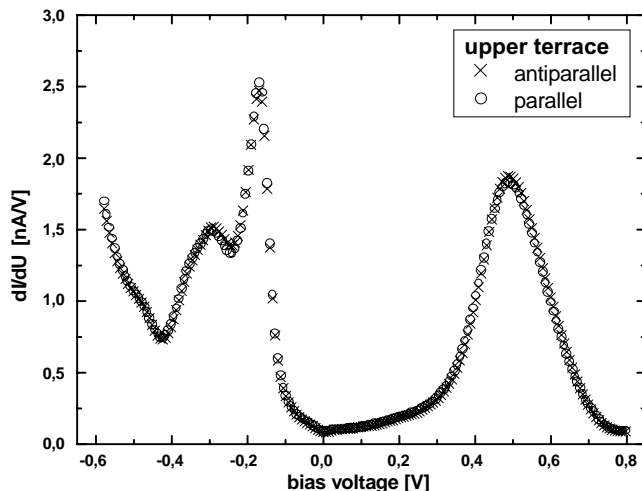
Figure 4.6: dI/dU vs. U curves taken *in remanence* on the upper terrace. Before each measurement tip and sample have been exposed to a magnetic field of $B = +1$ T perpendicular to the sample plane, the first time with the sample held upside down (antiparallel measurement), the second time in the normal position (parallel measurement). The curves show no significant differences.

In Fig. 4.6 two curves of the differential conductance dI/dU vs. U are shown, as measured on the upper terrace, one curve representing the antiparallel remanent case, the other the parallel remanent case. Surprisingly, the curves are virtually identical. The same is true for the respective curves measured on the lower terrace (not shown here). Such a result could have been expected for a measurement with a non-magnetic tip. As long as the main assumption, namely the out-of-plane orientation of the sample magnetization was upheld, two possible explanations had to be checked: (i) no Fe at the tip, (ii) Fe at the tip, but no remanent out-of-plane component despite a tip exposure to 1 T field.

Five additional measurements were carried out using the same tip at persistent fields of 1 T and 2 T as well as at 0 T. Fig. 4.7(a) shows the results obtained on the upper terrace, and 4.7(b) those obtained on the lower terrace. Already a first glimpse at the data allows to rule out the first option: a strong effect of the applied field can be seen in both figures proving the tip to be magnetically active. A closer inspection of the curves on the upper terrace show the peak in the negative bias range to grow with increasing field strength while the peak intensity in the positive bias range is reduced at the same time. A parallel alignment is what intuitively can be expected if both electrodes are subjected to the same field. The more surprising is an inspection of the lower terrace data: here the increasing field *dampens* the peak at negative bias, and the peak at positive bias is *enhanced*, a behavior which is completely in contrast to the one observed on the upper
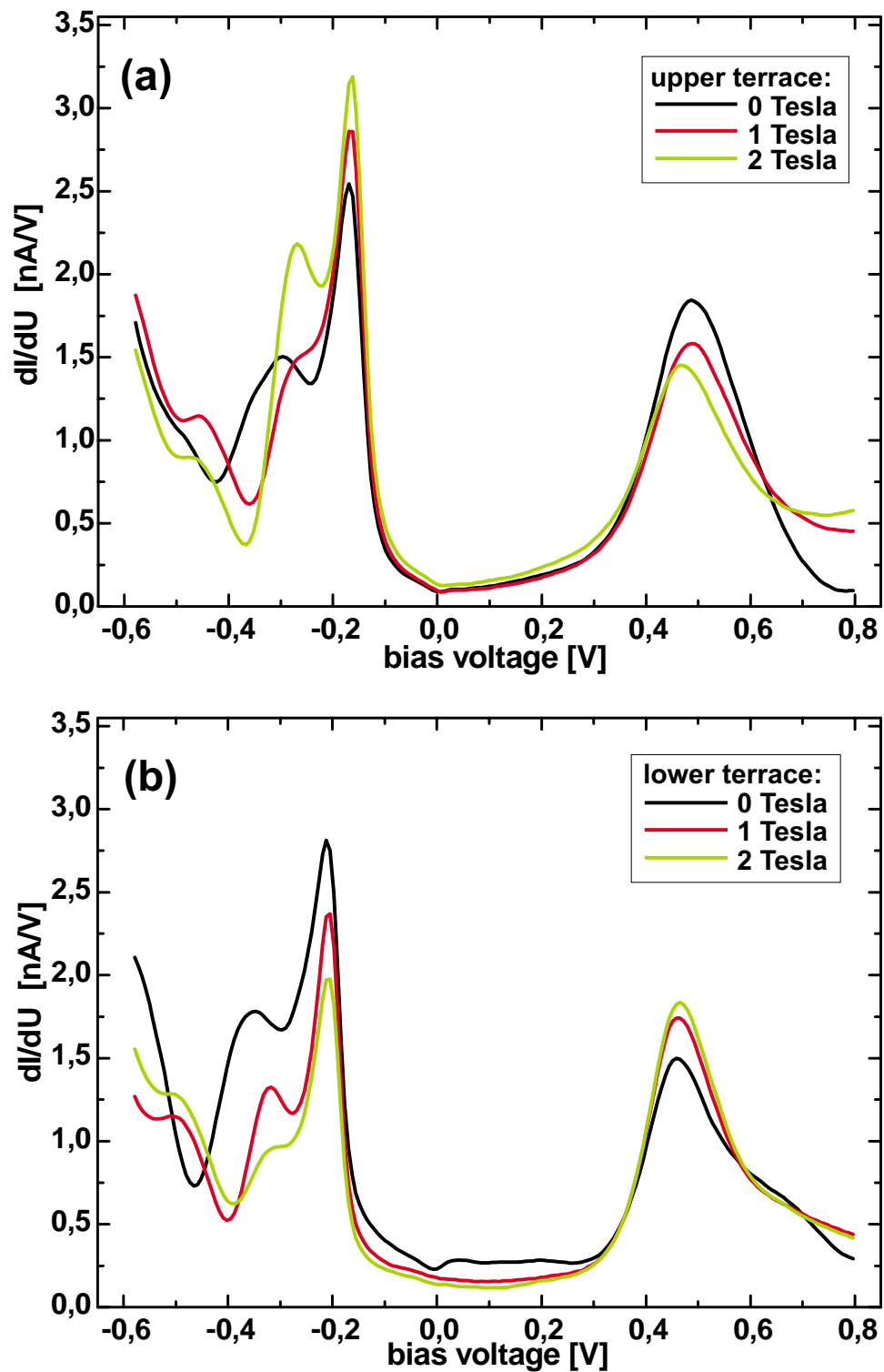
Figure 4.7: Curves of the dI/dU vs. U signal at three different field strengths taken on **(a)** the upper and **(b)** on the lower terrace. In **(a)** the increasing field amplifies the intensity of the peak at negative bias and dampens the peak at positive bias. In **(b)** the effect of the field is opposite.

terrace. In other words, the system reacts to the applied field *oppositely* on the two terraces, and if the upper terrace may be characterized by an increasing parallel alignment of tip and sample magnetization due to the increasing field, the lower terrace data must be interpreted as an increasing *antiparallel* alignment.

Such a behavior cannot be explained if an in-plane anisotropy of the Gd film is assumed. The field applied in $+z$ direction would turn both tip and sample magnetization into the same direction, and, regardless of the degree of initial alignment, a parallel configuration would be favoured by higher field strengths. It can be excluded that the external perpendicular field may turn an in-plane magnetization into one direction on one terrace and into the opposite direction on the next terrace. The observations can, however, well be explained if we return to our initial premises, namely an out-of-plane anisotropy of the sample and an in-plane anisotropy of the tip. In this case, the tip is insensitive to the magnetic orientation of the sample at $B = 0$ Tesla, since no out-of-plane component is available at the tip. This picture is supported by the results shown in Fig. 4.6 which, on the other hand, indicate that our early expectation of a *remanent perpendicular component*, once the tip had been exposed to 1 T, must be dropped. Now, in a persistent perpendicular field the tip magnetization is forced into a hard direction so that a perpendicular component evolves, introducing sensitivity to the sample's out-of-plane magnetization. Obviously, 1 T is not sufficient to obtain hard axis saturation of the tip, and the step towards 2 T still enhances the tip's out-of-plane component. This observation is consistent with previously reported results [69]. Now this tip is able to reveal information that was previously not accessible: one terrace is magnetized upwards, and the other downwards. It is this combination of two contrasting facts that proves the out-of-plane anisotropy of the Gd film. The argument given above does not require a knowledge which of the terraces really be oriented parallel or antiparallel to the tip but relies on the *opposite* effect the applied field produces on the two terraces.

The data shown in Fig. 4.7 allow to determine the asymmetries of the peak intensities for parallel versus antiparallel tip-sample magnetization alignment, represented by the two terraces, and thus the spin polarization of the Gd film which is given by

$$P_{\mathrm{Gd}} = \frac{1}{P_{\mathrm{Fe}}} \frac{I_{\uparrow\uparrow} - I_{\uparrow\downarrow}}{I_{\uparrow\uparrow} + I_{\uparrow\downarrow}}. \tag{4.1}$$

Here P_{Fe} is the polarization of the Fe coated tip which is assumed as 0.44 [70, 71], and $I_{\uparrow\uparrow}$ and $I_{\uparrow\downarrow}$ are the peak intensities for parallel and antiparallel alignment. P can be determined separately for the majority and the minority peak at negative and positive sample bias, respectively. We have to account for the fact that the zero-field curves found on the two terraces are not identical in intensity – which is not a magnetic but an electronic

effect probably related to the limited size of the upper terrace.[2] Therefore I have first calculated separately for each terrace the asymmetries $A_{\mathrm{maj,min}}$ introduced by the field at each peak position,

$$A = \frac{I_{B=2\,\mathrm{T}} - I_{B=0\,\mathrm{T}}}{I_{B=2\,\mathrm{T}} + I_{B=0\,\mathrm{T}}},$$

and then added the respective values. In this way a polarization at the majority (minority) peak position of 0.65 (0.52) is obtained. Since it cannot be decided which of the terraces is magnetized parallel to the tip the sign of the polarization remains undetermined.

4.2.1 Conclusions and Open Questions

The most important result in the context of the present work is the *out-of-plane anisotropy of the 7 ML Gd film*. In Chapter 6 I will describe how this property came back into play when a material for tip coating was needed that would allow to study another system with out-of-plane anisotropy, 1.5 ML Fe/W(110).

Many questions remain open regarding the ultrathin Gd films. They should be addressed in the future on clean, well ordered films to exclude any modifications due to contaminants. I list some of them:

- What is the cause of the high coercivity that must be concluded from the observation that still at $B = 2$ T the two terraces give an opposite response to the applied field?

- Is there an antiferromagnetic coupling from one atomic layer to the next? If so, what may the coupling to next-deeper layers be?

- Is the peculiar magnetic behavior the result of a stacking fault? Bode *et al.* [72] have shown by spatially resolved STS measurements – albeit not spin-polarized – that stacking faults in ultrathin Gd(0001)/W(110) films lead to a significant modification of the intensities and energetic positions of the surface state peaks.

- If the observed phenomenon turns out to be only a local feature resulting, e.g., from a stacking fault, a ferromagnetic perpendicular order in the film in general is expected. In this case an interesting domain structure should be present in the film in order to minimize the stray field.

- What is the critical film thickness for the transition to in-plane anisotropy?

---

[2]Note that there is also a slight shift in the energetic position of the peaks.

Chapter 5

Ultrathin Fe/W(110) Films: Previous Results

The system investigated in the remaining chapters is 1.5 ML Fe grown on W(110). In the low coverage regime, epitaxially grown iron films show a rich variety of structural and, just as rich, of magnetic appearences. The changes with coverage have been studied by various methods, as, e. g., Auger electron spectroscopy (AES), low energy electron diffraction (LEED) [73–75], thermal desorption spectroscopy (TDS) [74, 75], by scanning tunneling microscopy [40, 76–78], stress measurements have been performed by a beam deflection method [79], and the local electronic structure was studied by scanning tunneling spectroscopy [40,80]. The magnetic properties have been investigated by conversion electron Mössbauer spectroscopy (CEMS), torsion oscillation magnetometry (TOM) [81] and magneto-optical Kerr effect (MOKE) measurements [82–85]. The most decisive parameter is the mismatch of the lattice constants: $a_{\mathrm{W}} = 3.165$ Å, $a_{\mathrm{Fe}} = 2.866$ Å [86] resulting in a huge lattice strain: $(a_{\mathrm{W}} - a_{\mathrm{Fe}})/a_{\mathrm{W}} = 9.4\%$. This mismatch enforces rapid changes of the morphology (and hence the electronic and also magnetic properties) with each ML added, until at 4 ML the film has attained the Fe bulk lattice constant. These rapid transitions at ultralow coverages make the system Fe/W(110) extremely complicated but also extremely interesting.

5.1 Morphology

Due to the high surface energy of the W substrate as compared to Fe ($\gamma_{\mathrm{W}} = 3.5$ Jm^{-2}, $\gamma_{\mathrm{Fe}} = 2.9$ Jm^{-2} [87]), the first Fe monolayer wants to coat the surface completely thereby reducing the system's free energy. This first wetting layer grows pseudomorphically on W(110) and is still stable at anneal temperatures as high as 1000 K [74]. For subsequent layers, the situation is different, since they can grow already on the preexisting overlayer at reduced surface energy. At room temperature, the second layer nucleates

46
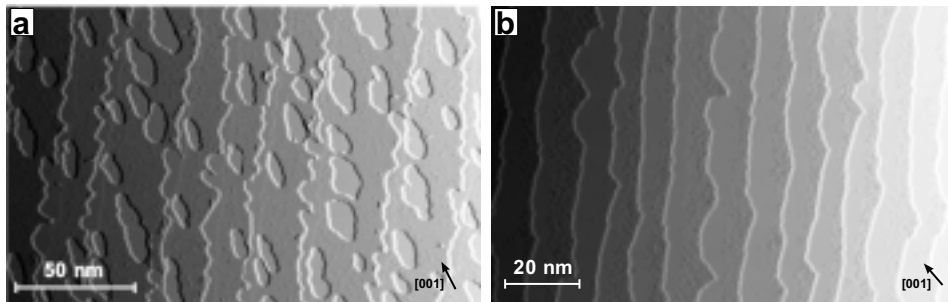
Figure 5.1: Topography of ultrathin Fe films on stepped W(110). A closed first atomic layer covers the substrate. **(a)** $\Theta = 1.3$ ML. When grown at room temperature, the second atomic layer partly decorates the step edges, partly forms patches which start to coalesce at a coverage of $\Theta = 1.6$ ML. **(b)** $\Theta = 1.5$ ML. Annealing at $T = 550$ K for 4 min. leads to step flow growth resulting in a periodic system of continuous stripes of alternating one and two atomic layers thickness extending along the substrate step edges.

in islands which are surrounded by the monolayer sea. These islands show a preferred growth direction along [001] leading to an aspect ratio of 1:2 - 1:4 [77]. An example for island growth mode is displayed in the topographic STM image in Fig. 5.1(a). The morphology can be modified by moderate annealing at $T \approx 550$ K or by growth at elevated temperatures. The result is step flow growth: the Fe atoms use their enhanced mobility to move to the step edges, from there progressively covering the substrate terraces. This leads to stripes, or *nanowires* extending along the substrate step edges. This growth mode can be observed for coverages Θ in the sub-monolayer regime as well as after completion of the first layer, $\Theta - 1$ in this case indicating the fraction of the terrace widths covered by an additional atomic layer. At this stage, before completion of the second atomic layer, each terrace of the substrate carries a Fe film of alternating one and two layers thickness. Fig. 5.1(b) shows an STM image of a Fe film in stripe morphology at $\Theta \approx 1.5$ ML. This system of stripes will be mainly focused on in this and the following chapters since it exhibits very unusual magnetic properties.

Both in island and in stripe morphology, the second layer initially also grows pseudomorphically with the substrate, until, at a coverage of about 1.7 pseudomorphic ML, dislocation lines extending along [001] appear indicating a local onset of relaxation by an introduction of additional rows of atoms.[1] The third layer starts to nucleate on top of dislocation lines before completion of the second. Fully developed, the third layer exhibits a strictly periodic 1-dimensional network of dislocation lines that is extended to a 2-dimensional network in the fourth layer. This is a consequence of a full

---

[1]The critical coverage for the dislocation lines to appear depends on the preparation conditions. Bethge [77] observed them already at $\Theta > 1.2$ ML in films grown at $T = 570$ K.

lateral relaxation of the Fe film that eventually attains its proprietary lattice constant; a Moiré pattern emerges due to Fe atoms periodically pushed off the substrate lattice sites. In STM images, the 2D network has been observed to decrease in corrugation with increasing film thickness up to a thickness of 12 ML [77]. By scanning tunneling spectroscopy Bode [40] was able to observe the characteristics of the coverage dependent electronic properties. As shown in Fig. 2.4, p. 18, he found an enhanced LDOS at positive sample bias (unoccupied states) for the first and the second layer with slightly higher energy values and intensities for the latter, whereas for local coverages $\Theta > 3$ ML an LDOS maximum appears at a bias of $U = -0.5$ V (occupied states), indicating that the process of relaxation has a strong influence on the electronic structure.

Another parameter influencing the morphology is the orientation of the substrate step edges. Elmers has shown that Fe DL stripes grow smoothest if the step edges extend along [001] [85,88]), while for the case of step orientation along [1$\bar{1}$0] the continuous stripes are replaced by chains of discontinuous, triangular shaped islands [89].

The two W(110) single crystals used throughout the present work have a step edge orientation which is between the two extrema, roughly along [1$\bar{1}$1]. Substrate #1 has a miscut with respect to the (110) plane of $\alpha_1 = 1.42°$ resulting in an average terrace width of $\overline{w_0} = 9$ nm, and substrate #2 is miscut by $\alpha_2 = 0.5°$ with $\overline{w_0} = 25$ nm.

5.2 Magnetic Properties

It is the merit of U. Gradmann and H.J. Elmers that, due to the long term work of their groups, the magnetic properties of the system Fe/W(110) are comparatively well understood. The relaxed Fe film ($\Theta \geq 4$ ML) is magnetized in the plane and attains the bulk magnetization value at a thickness of 60 Å [90], and also films of a thickness of $\Theta > 2$ ML are reported to be magnetized in the plane [84,91].

For the closed Fe monolayer, it has been shown that it is ferromagnetic [81] with an in-plane uniaxial anisotropy oriented along [1$\bar{1}$0] [76]. By torsion oscillation magnetometry (TOM) Elmers *et al.* [92] determined an enhanced magnetic moment per atom for the ML ($\mu = 2.53$ μ_B) and the DL ($\mu = 2.46$ μ_B) as compared to the bulk value of 2.2 μ_B for Fe films coated by Ag. The ML Curie temperature was found to be $T_C^{ML} = 225$ K decreasing to 180 K with a decrease of coverage to $\Theta = 0.6$ ML where ferromagnetism vanishes [76]. STM studies revealed that for the island morphology coalescence starts at exactly this coverage and thus magnetic percolation of the Fe patches; for lower coverages, the patches are superparamagnetic. In stripe morphology the ML films remained ferromagnetic down to $\Theta = 0.05$ ML corresponding to average Fe stripe widths of 0.8 nm or about 4 atomic chains,

with an easy magnetization axis along [1$\bar{1}$0].

Despite the progress in understanding of the ML, the DL regime remained puzzling for a long time. Controversial results were reported in the literature for films at $\Theta = 1.3$ ML, prepared in island morphology. Sander *et al.* [79] and Back *et al.* [93] found high in-plane coercivity while Elmers *et al.* [91] reported a complete absence of long range magnetic order for the coverage range of 1.2–1.48 ML. A new approach was proposed by Weber *et al.* [94] who showed by TOM and, for the first time, by *polar* Kerr measurements, that there is a *perpendicular* magnetization of the DL islands within the in-plane magnetized ML sea, concluding a "nanoscale spatial switching of magnetic anisotropy". To make things even more complicated, this perpendicular magnetization was shown to be highly sensitive to contamination from the residual gas [80,88,95] which causes the easy axis to rotate into the plane or, alternatively, to degrade the perpendicular magnetization. Also in the DL stripe morphology a similar perpendicular anisotropy was observed for $1.1 < \Theta < 2$ [84]. Adjacent DL stripes were suggested to couple antiferromagnetically from dipolar interaction, the result being a macroscopically demagnetized state of the DL.

Chapter 6

Spin Polarized Imaging of 1.5 ML Fe/W(110)

Before I present recent results obtained on the system of magnetic nanowires Fe/W(110)[1] I will focus in this chapter on a detailed discussion of the imaging process in spin polarized tunneling spectroscopy [98]. To start with, spin-averaged data will be shown recorded with a bare tungsten tip. Then spin polarized spectra will be presented. I will explain how the spectra can be used to visualize magnetic domains. A simplified procedure for faster data acquisition will be derived, leading to a convenient method of high spatial resolution magnetic domain imaging. Further, some aspects of the tip magnetic anisotropy will be discussed.

6.1   Spectra Taken with Uncoated Tips

In Fig. 6.1(a)-(c) spectroscopic curves, the topography and a map of the differential conductance of a 1.3 ML Fe/W(110) film is shown, recorded by a bare tungsten tip at a temperature $T = 16$ K. In confirmation of earlier results [40,80] we find two distinct types of spectra which reflect the different electronic properties of ML and DL.[2] The ML curve (gray) shows a main peak at about +400 mV, and the DL curve (black) has an even more pronounced peak at +680 mV; at this bias, the ML signal is particularly low. These two types of spectra have been found consistently on *all* ML and DL stripes, respectively. If we plot a map of the dI/dU signal at the bias of the DL peak, Fig. 6.1(c), DL areas appear bright, as opposed to ML areas appearing dark accordingly. Thus, in the dI/dU map the respective stripes

---

[1] A study of the coverage dependent magnetic properties of films in *island* morphology by Kubetzka *et al.* [97] has recently been published. This topic will not be discussed in the present work.

[2] In the remainder of the present work images will be shown using a color scale that is better adopted to facilitate a comprehension of the delicate contrasts than a grey scale.
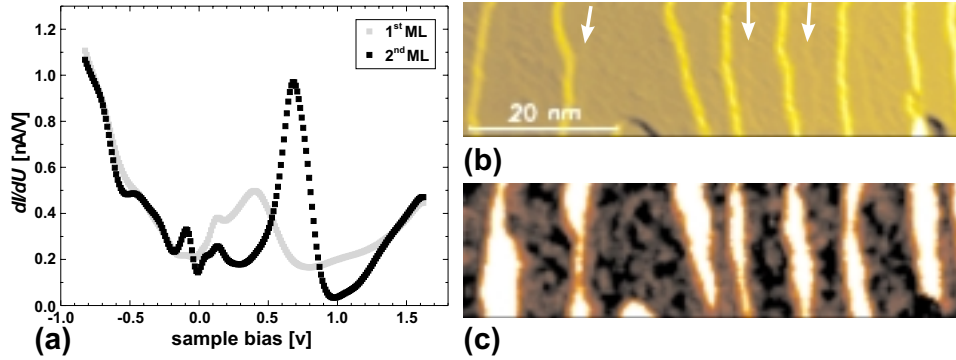
Figure 6.1: **(a)** Spectra taken with an uncoated W tip, recorded on the 1.3 ML Fe/W(110) film shown to the right as **(b)** a topographic image and **(c)** as a map of the differential conductance. While the homoplanar ML-DL transitions in **(b)** are visible merely as faint lines (see arrows), the dI/dU map, taken at the bias voltage of the DL peak position, displays clearly the bright DL areas (high conductance) and the dark ML areas (low conductance).

can easily be discriminated even where they are not separated by a step of monatomic height. In the constant current topography shown in Fig. 6.1(b) this is hardly possible. I have marked by arrows a few of the faint lines that indicate the ML–DL border.

6.2 Spectra Taken with Magnetically Coated Tips

Before the corresponding spin-resolved experiment with a ferromagnetic tip could be performed one more obstacle had to be overcome. So far, experience was available only for Fe as a coating material for tunneling tips, and as was clear from Ref. [22] and the Gd experiments described in Chapter 4 these tips exhibit a magnetization parallel to the sample plane. This is inappropriate for imaging the DL stripes since their easy axis is perpendicular. According to Eq. 2.24 no spin polarized contribution to the tunneling current is expected if the magnetization of tip and sample is at right angle. A measurement with an applied external field was not feasible in this experiment since, according to Ref. [84], the DL stripes are saturated at $\mu_0 H_s = 17$ mT, a value much too low for gaining a considerable perpendicular component in the tip. In higher fields, however, the effect to be observed, namely a contrast alternating between adjacent DL stripes, would be quenched. Hence, a tip with a perpendicular magnetization was indispensable.

This is where our results achieved with 7 ML gadolinium came back into play. The idea was as follows: if 10 ML Fe at the tip give an anisotropy like it was known for an extended 10 ML Fe film on a flat W(110) substrate, namely *in the plane*, should not 7 ML Gd at the tip again show an anisotropy like

that identified previously on the flat substrate — *perpendicular*?[3] Already
the first experiment with a tip coated by 7 ML Gd proved to be successful.

6.2.1   Spin Resolved Spectra of 1.5 ML Fe/W(110)

Fig. 6.2(a) shows schematically the structure of the stripe system below the
height profile which is taken along the line indicated on the topograph (see
inset). Arrows indicate the magnetization directions, being in the sample
plane for the ML and alternatingly pointing up and down in the DL stripes,
according to Ref. [84]. Fig. 6.2(b) shows dI/dU-spectra which were measured
using a Gd coated probe tip. Again, ML and DL spectra can easily be
distinguished, with the ML peak at +400 mV and a strong DL peak at
+680 mV. However, this time we find two different types of spectra above
the DL stripes which will hereafter be referred to as ↑↑ and ↑↓. Both spectra
exhibit the same general shape but differ in intensity. While the differential
conductivity at the peak position amounts to only $dI/dU = 1.3$ nA/V for
the spectra of type ↑↓ it is enhanced by about 40% to $dI/dU = 1.8$ nA/V
for type ↑↑. The relative intensities between both types of spectra invert
for $U < 500$ mV. These differences in the tunneling spectra of the Fe DL
stripes are caused by spin- polarized tunneling between the magnetic tip and
Fe DL stripes being magnetized either parallel or antiparallel to the tip. In
Fig. 6.2(c) a map of the differential conductivity dI/dU at the peak position
($U = +680$ mV) is plotted. Different intensities of the dI/dU-signal show up
as different color levels. Since the dI/dU-signal at $U = +680$ mV is much
lower for the monolayer than for double-layer stripes the former appears
black. Furthermore, the data reveal that most double-layer stripes exhibit
only one type of spectrum, either ↑↑ or ↑↓, and that the type alternates
between adjacent stripes. This observation is consistent with the proposed
AFM out-of-plane coupling of adjacent stripes [84, 85, 96]. In Fig. 6.2(c)
some exceptions from this rule have been marked by arrows demonstrating
the impact of the high spatial resolution of SP-STS. Approximately in the
middle of the image one can recognize two adjacent stripes which exhibit
the same dI/dU-signal (black arrows). Obviously, these stripes are so close
together ($d < 1.5$ nm) that the exchange coupling overcomes the energy gain
due to the dipolar antiparallel coupling. Furthermore, at the very right edge
of the image we can find two stripes which change the type of spectrum from
the bottom to the top part of the image, i.e. both stripes exhibit a domain
wall (white arrows). These are details found on a lateral scale which is not
accessible by spatially averaging methods.

---

[3]Implicitly, this idea rests on the assumption that, contrary to intuition, the tip is rather
blunt allowing to carry a more or less extended film that exhibits, at least with regard to
magnetic anisotropy, the properties of a flat film. The soundness of this assumption will
be discussed in more detail later.
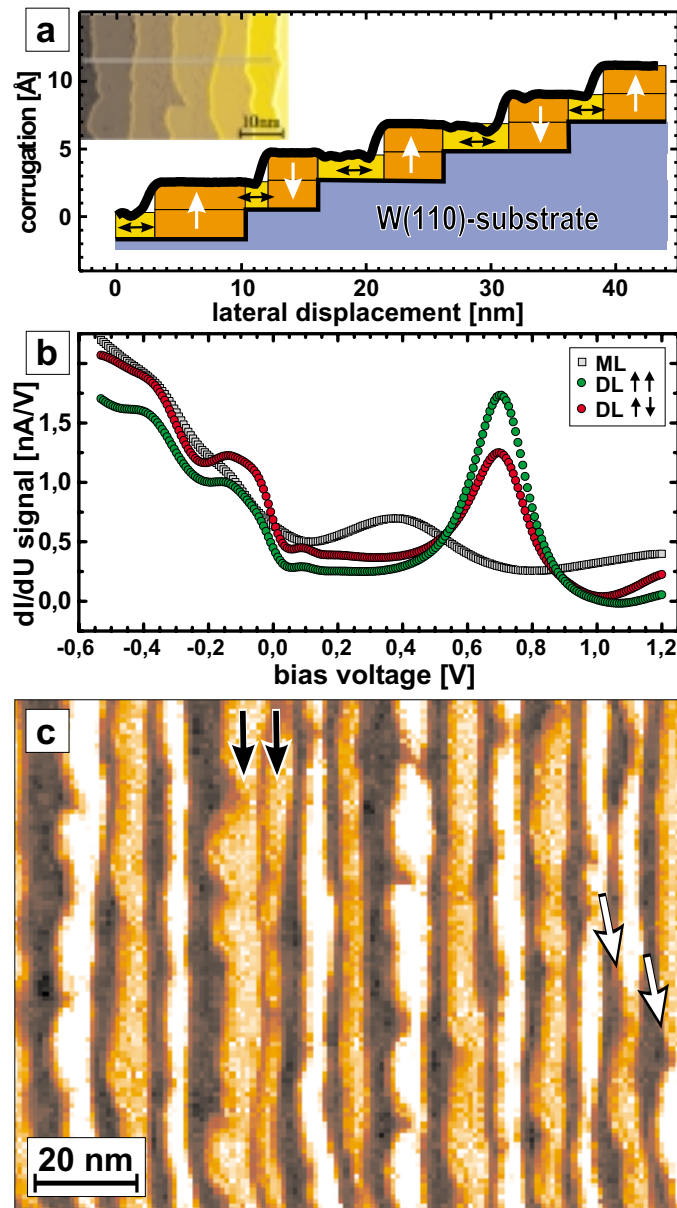
Figure 6.2: **(a)** Height profile taken along the line indicated in the topograph shown in the inset and schematic structure of 1.5 ML Fe on a stepped W(110) single crystal. Arrows indicate the magnetization direction of the ML (in-plane) and the DL stripes (perpendicular), the latter alternating from one DL stripe to the next. **(b)** Spectra measured by a W tip coated by 7±1 ML Gd exhibiting a magnetization perpendicular to the sample plane. The ML again exhibits a peak around +400 mV (gray curve). On the DL stripes we find two distinct spectra differing in intensity (red and yellow curves). This effect is due to the difference in conductance for parallel and antiparallel tip-sample configuration. **(c)** dI/dU map taken at the DL peak voltage $U = +680$ mV. The ML appears black according to its intensity being lowest. The antiparallel order of the DL stripes becomes visible by the two-stage contrast which is observed to alternate from one stripe to the next. Black arrows mark two stripes being exchange coupled due to a vanishing ML width between them. White arrows mark two domain walls.

6.2.2   The Impact of Bias Voltage on the Contrasts

In the following, some implications of the spectroscopic method used shall be discussed. We have seen so far that the DL peak position ($U = +680$ mV) is particularly suited for an imaging of magnetic domains since the contrast between the spectra $\uparrow\uparrow$ and $\uparrow\downarrow$ is maximum. Choosing another bias voltage will change the contrast distribution. In Fig. 6.3 this effect is demonstrated for selected voltages from the same data set. We follow the curves from right to left, i.e. we progress from positive towards negative sample bias. At $U = +880$ mV the DL curves have a crossing point, and consequently no contrast between DL stripes can be observed at this bias. For $U = +635$ mV we observe the distribution already seen in Fig. 6.2. Going to lower bias voltages, the DL curves again cross each other at $U = +550$ mV, again with a loss of DL contrast. Below this voltage the ML curve becomes most prominent. The effect can be seen in the map at $U = +275$ mV: the ML appears brightest now, and the contrast order of the DL stripes is reversed. At $U = 0$ mV, corresponding to the Fermi level, we find contrast between the DL stripes, but now the ML exhibits a differential conductance almost equal to that of the bright DL stripe, and they can hardly be separated.[4] This holds also in the map given for $U = -170$ mV. From the observation of a DL contrast reversal as a function of the applied bias the conclusion must be drawn that it is *not clear* from the very start which of the DL stripes have a magnetization parallel to the tip magnetization and which of them have it antiparallel, because the parallel case can appear bright, or dark, depending on the bias voltage, and the same holds for the antiparallel case. Thus, for a given bias voltage, the correct assignment can only be decided in an applied external field *enforcing* a parallel configuration so that *either* dark *or* bright is switched and only one color, corresponding to the domain type aligned parallel to the external field and hence to the tip remains for the DL stripes at saturation. Such results will be presented in chapter 8, and it will be shown that a bright coloring at the bias voltage of the DL peak position corresponds to a parallel alignment. Up to now, in all our measurements with a field applied, we did not observe an exception from this behavior at this particular voltage, justifying the notation $\uparrow\uparrow$ and $\uparrow\downarrow$ already used above.

It must be emphasized that the last statement applies to the DL peak voltage only; other details of the spectra are found to depend strongly on the particular tip in use. This is illustrated by another set of spectra shown in Fig. 6.4; only the DL curves are shown for clarity. While the shape of the curves in general agree with those shown in Fig. 6.2 there are also some remarkable differences. We again observe the curves to cross each other to the right and to the left of the DL peak, at $U = 870$ mV and $U = 530$ mV, respectively, and we already discussed that this means a contrast reversal

---

[4]This ML signal must not be interpreted in terms of a perpendicular magnetization. It is of pure electronic origin.
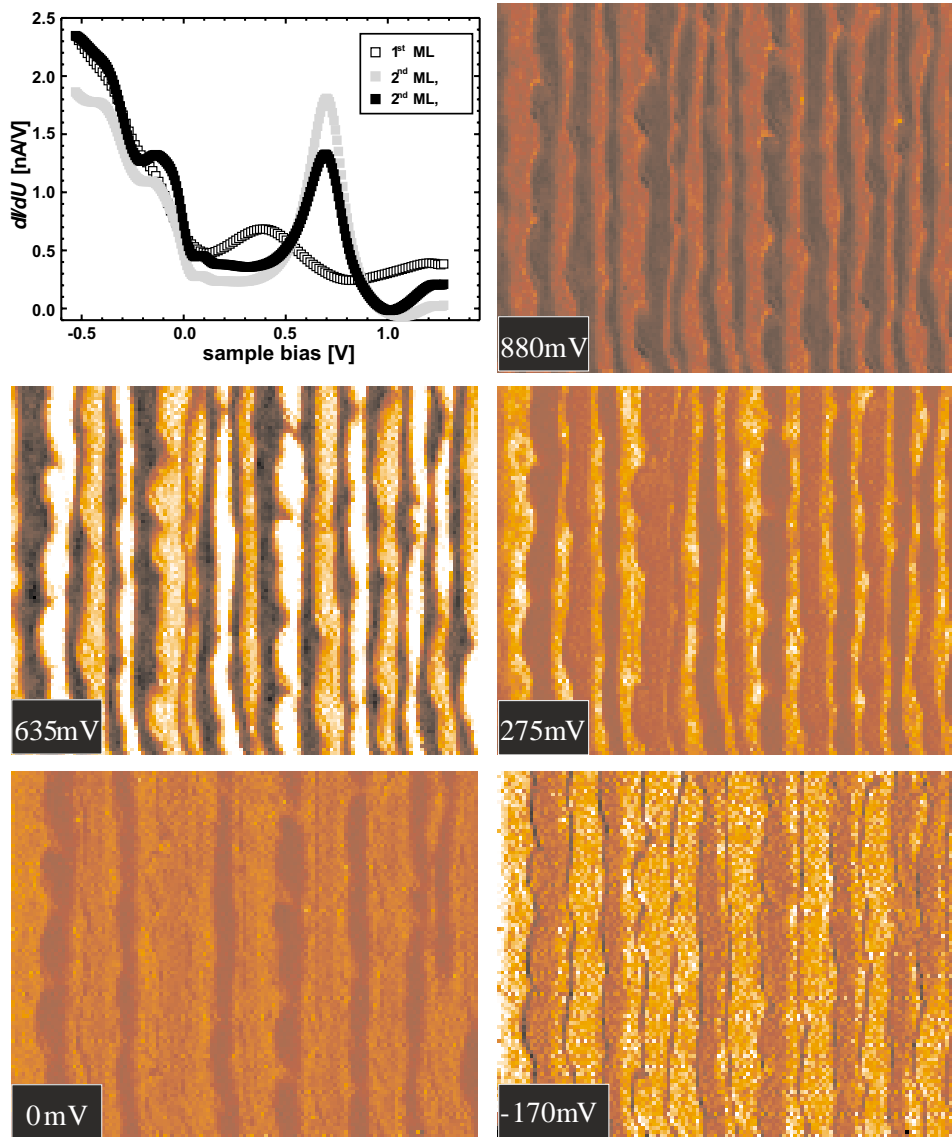
Figure 6.3: Contrast distributions as a function of the applied bias voltage, according to the relative spectral weights of the three curves. Note the inversion of the DL contrast by comparing, e.g., the maps for $U = +635$ mV and for $U = +275$ mV. Also, the relative ML intensity has changed place.
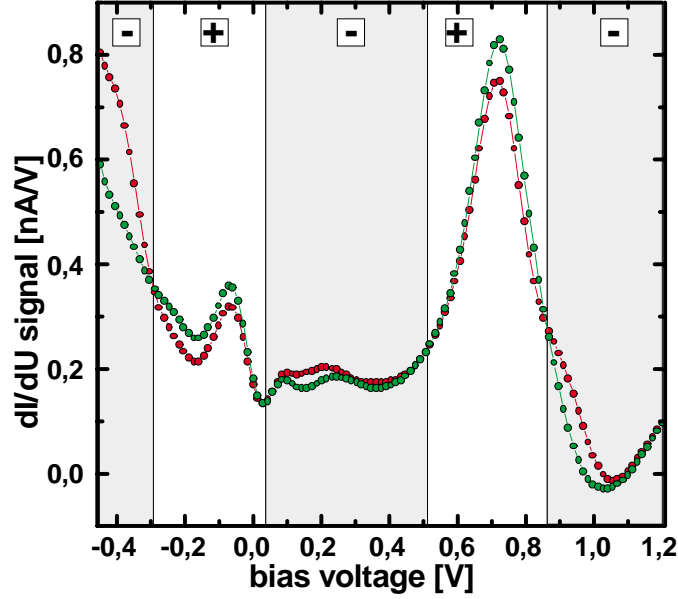
Figure 6.4: DL Spectra taken with a different tip showing two additional crossing points which are absent in the previous example. They result in additional contrast reversals at the respective bias voltages, which is equal to a repeated change in sign of the spin polarization of the tunneling junction. This is how each particular tip introduces its own signature.

if we plot a dI/dU map for a voltage beyond the crossing point. Fig. 6.4 shows two more crossing points at $U = 30$ mV and $U = -290$ mV which are absent in the spectra shown in Fig. 6.2. Accordingly, the contrasts undergo additional reversals at the appropriate voltages. Or, to put it another way, the sign of the spin polarization P_{ts} of the tunneling junction is switched four times in the spectra shown in Fig. 6.4 while it is switched only twice in those of Fig. 6.2 within the same energy interval. In Fig. 6.4 the voltage regimes of opposite spin polarization are indicated by different background colors. We recall Eq. 2.27, $P_{ts} = P_t \cdot \tilde{P}_s$. The sign of P_{ts} is positive if $I_{\uparrow\uparrow} > I_{\uparrow\downarrow}$ and it is negative if $I_{\uparrow\uparrow} < I_{\uparrow\downarrow}$. Note that here the arrows indicate the magnetization alignment, not the spin polarization. If the parallel case shows a higher conductance than the antiparallel case (this is what we observe in high fields for the voltage range around the DL peak) this can be accomplished in either of two ways: (i) the tunneling current is dominated by majority electrons tunneling into majority states, $P_t > 0$ and $P_s > 0$, i.e. both electrodes exhibit a positive spin polarization, or (ii) the current is dominated by minority electrons tunneling into minority states, $P_t < 0$ and $P_s < 0$, i.e. both electrodes exhibit a negative spin polarization. If, however, one of the electrodes changes the sign of its polarization due to the particular selection of states contributing to tunneling as a function of the

bias voltage also the sign of P_{ts} will be changed. I have labeled the energetic regions in Fig. 6.4 accordingly. This is what can be observed in the spectra of Fig. 6.4 off the DL peak range. It has to be emphasized that the number and energetic positions of such inversions in spin polarization depend on the particular tip.

While the energetic position of, e.g., the main ML and DL peaks are very stable in all spectra, their intensities can change considerably when the tip is exchanged. Especially in the negative voltage regime we occasionally observe large spectroscopic features that may vanish completely upon tip exchange. As has been discussed earlier (cf. p. 18), it is very likely that this sort of spectral features reflect properties of the Gd tip rather than those of the sample. Such structures can be highly spin polarized resulting in an accordingly high contrast at the appropriate bias voltages. Hence, they may very well be used to image the domain structure of the sample. The assumption of a constant spin polarized tip density of states as discussed in Chapter 2 is a good approximation only in the limit of a few mV around the Fermi level. At higher bias voltages this assumption is no longer valid. Instead one may clue, with due caution, that certain characteristics of the density of states observed in thin films on a flat surface may be preserved on a "flat", i.e. blunt tip, albeit subjected to distortion by the reduced symmetry of the effective tip apex. Details will depend on the exact atomic arrangement which cannot be controlled. However, it may be the better guess to take, of instance, the 7 ML Gd spectra discussed in Chapter 4 as a guideline of a Gd coated tip's density of states than an assumed constant value. Summarizing, a *high spin polarization of the tunneling junction* and not so much a particular sample spectral feature is required to gain a good magnetic contrast; so for the purpose of domain observation the bias voltage can be chosen in a quite pragmatic way.

6.2.3 Accelerated Data Acquisition: Reduced Spectroscopic Layers

In a measurement like the one shown in Figs. 6.2 and 6.3 225 spectroscopic data points have been measured at each of the 130×130 pixels requiring a total measurement time of about 12 hours. However, once it has been made clear how the observed contrasts are related to the magnetic domain structure of the sample it is no longer necessary to take full spectra. Instead, one can choose an appropriate fixed bias voltage providing a good spin contrast and measure *just one* $\mathrm{d}I/\mathrm{d}U$ map using lock-in technique. Giving up *energy resolution* saves an enormous amount of time (and data storage space), and we can reinvest some of the savings into a much higher *spatial resolution*. Now a standard 500×500 pixels image takes only about 30 minutes. Furthermore, since the tip is scanned back and forth, we can, with no additional time required, measure at one voltage in the forward direction and
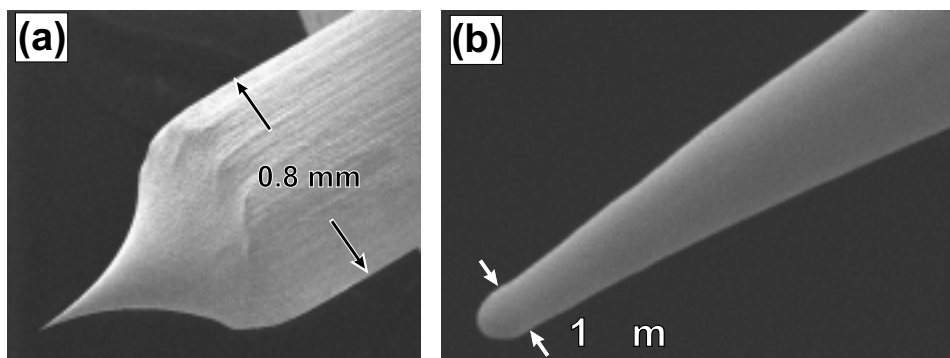
Figure 6.5: Scanning electron microscopy (SEM) image of a freshly prepared tungsten tip.

at another voltage in the backward direction. In our standard procedure we record a constant-current image and simultaneously a $\mathrm{d}I/\mathrm{d}U$ map in each scan direction totaling in four images per data set. In addition to the bias voltage of the DL peak, we found the value of $U = -300$ mV particularly suited for imaging the magnetic domain structure at high contrast. In the following figures, this bias can easily be recognized at first sight since it lets the ML appear bright.

6.3   Tip Issues

6.3.1   Tip Magnetic Anisotropy

As has been mentioned earlier, the experiments showed that the use of Gd as a tip coating material leads to a magnetization orientation perpendicular to the sample plane, that is along the tip axis, and in the case of Fe the orientation is in the sample plane, that is perpendicular to the tip axis. Especially the latter observation is in contradiction to the intuitive picture of a sharp tip suggesting an anisotropy being governed by its shape. By definition, a tip is an elongated piece of material, and in the case of a bulk ferromagnetic tip certainly a magnetization directed along the tip axis can be expected due to shape anisotropy. In Chapter 4 it has been shown, however, that a Fe coated tip gave no magnetic signal on a perpendicularly magnetized Gd film in zero magnetic field while a strong field applied parallel to the tip axis gave rise to a clear sensitivity of the tip to the sample magnetic orientation. Recalling the linear $\cos \varphi$ dependence of the magnetic signal, φ being the angle between tip and sample magnetization directions, this effect was explained by a vanishing out-of-plane tip magnetization component with the field removed, $\cos \varphi = 0$, and a finite value of $\cos \varphi$ when the tip magnetization is forced into its hard direction by the external field. This observation indicates a negligible influence of the tip *shape* on the anisotropy of the thin

film coating. This conclusion is supported by the following considerations. During preparation the tungsten tip is heated by electron bombardment to temperatures $T > 2000$ K, the temperature presumably being much higher at the tip apex. On melting of the tip apex this procedure results in a blunt tip exposing most likely a densely packed (110) surface. Fig. 6.5 shows a scanning electron microscopy (SEM) image of a tip after a flash, revealing a radius of curvature of about 0.5 μm which is large compared to the 1–2 nm thickness of the coating film. In the actual tunneling process, the current will certainly flow through some cluster of a few atoms being closest to the sample surface; the magnetic anisotropy of the coating film, however, is most likely determined on a mesoscopic scale by surface and interface terms due to the blunt tip. Using this picture, also the anisotropy of 7 ML Gd at the tip is not primarily the result of shape anisotropy. Instead, the anisotropy of the tip coating film can be deduced from the anisotropy the same material exhibits when deposited on a flat substrate.

6.3.2   Tip-Sample Interaction

In their study of the 50 ML Gd film domain structure Bode *et al.* [22] had shown examples for domain switching while the sample was scanned by a tip coated with 100 ML Fe. Since they never observed a domain switching if the tip coating was only 10 ML thick they concluded that the switching was induced by the stray field the tip exerts on the sample.

In our present case the situation is reversed in the sense that now the sample is a Fe film and the tip carries a Gd coating, and the question arises how tip–sample interactions will show up now. Occasionally one particular tip produced a quite strange dI/dU signal while the simultaneously recorded constant current image showed no irregularity at all. An example is presented in Fig. 6.6. We observe the DL contrasts to be reversed every few scan lines, and the reversal always affects the full image width. This is different from the observation made by Bode *et al.* on the Gd films where only a single domain switched while nerighboring domains stayed unaffected. We thus conclude that in our case not the sample but the tip is switched by the sample's stray field. I have intentionally selected an image of only moderate resolution since it allows to identify some of the switching events at pixel resolution; a few examples have been marked in Fig. 6.6 by circles. The image was recorded with the tip scanned from right to left (fast scan direction), bottom to top. This explains why not more switching events can be localized: they might occur at equal probability while the tip moves in the opposite direction. Also, a switching occuring above a ML stripe is not easily identified since ML contrasts remain unchanged. At the location marked by an arrow in Fig. 6.6 seemingly an inconsistency shows up: while all other DL stripes reverse their contrasts upon tip switching the marked stripe keeps its color. An explanation can be found in a domain wall causing an additional contrast
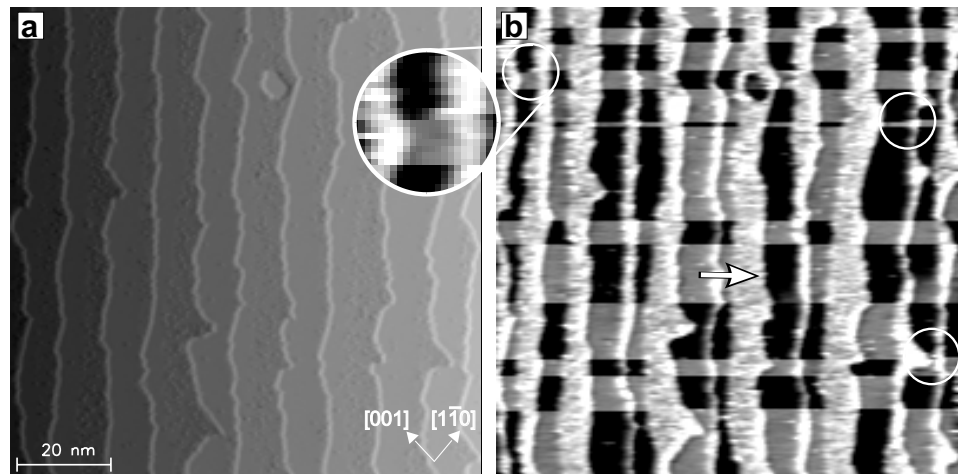
Figure 6.6: **(a)** Constant current image and **(b)** dI/dU map measured simulta-
neously. While the topography shows no irregularities the dI/dU signal is reversed
frequently. This is the result of a magnetization reversal of the tip due to the sam-
ple's stray field. Circles mark locations where switching events could be identified
at pixel resolution, see the inset. The DL stripe marked by an arrow seems not to
follow the reversal; the cause is a domain wall in this stripe, reversing the dI/dU
signal once again.

reversal in this particular stripe.

It is obvious that the Gd tip coating is magnetically softer than the
Fe film. Two possible mechanisms for tip switching may be responsible.
Either the tip Gd film switches as a whole, or a domain wall close to the
tip apex moves back and forth under the influence of the sample stray field.
In Chapter 8 we will be able to give an estimate of the tip's coercivity from
observations made in an applied magnetic field.

Chapter 7

The Magnetic Domain Structure of Fe Nanowires

It has already been mentioned that the details of the DL nanowire magnetic domain structure were inaccessible prior to the application of SP-STM. Using the simplified imaging method derived in Chapter 6 we now have access to a wealth of previously unseen details at high spatial resolution. In this chapter I will discuss results obtained for both DL and ML stripes.

7.1   Overview

In Fig. 7.1 a simultaneously recorded topography and $\mathrm{d}I/\mathrm{d}U$ map is shown, taken at tunneling parameters $I_{\mathrm{tun}} = 0.3$ nA , $U = -300$ mV on substrate #1. From the topograph (a) we notice that ML areas appear rougher than DL areas; obviously, any adsorbate from the residual gas is pushed onto the ML. This effect was also observed by Hauschild *et al.* [84] and will be visible in all images. Note that the size of adsorbates is exaggerated by STM imaging. Within the scan range of 200×200 nm 21 DL stripes are found, and from the total visible DL stripe length of $l = 4200$ nm about 47% appear bright in (b), and 53% dark confirming the overall demagnetized state. The DL stripe width is rather inhomogeneous and displays numerous constrictions. This morphology is typically found in stripes grown at room temperature with subsequent annealing. The number of 7 domain walls allows a very rough estimate for the average domain length which is several 100 nm. However, at the lower right corner a dark domain of only 31 nm length, marked by arrow (A), is present which is obviously exchange coupled to the next stripe to its left, indicating that a quite wide distribution of lengths may be found. At the site marked (B) a pair of domain walls can be found which is correlated by dipolar interaction. This type of correlation can frequently be observed.

   Two types of domain walls can be distinguished. These are shown in more detail in the insets of Fig. 7.2. The left panel shows a relatively broad
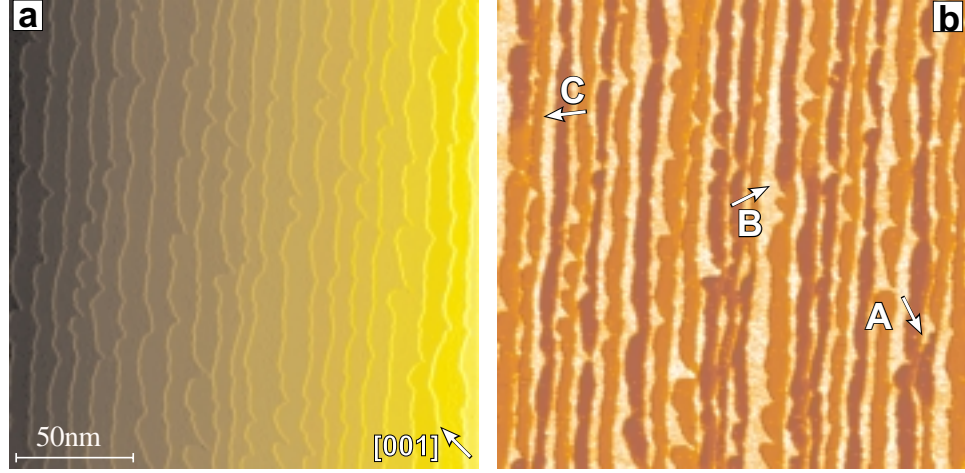
Figure 7.1: **(a)** Topography and **(b)** dI/dU map of a 200×200 nm^2 scan, providing an overview. At the chosen bias voltage $U = -300$ mV the ML appears brightest, as explained along Fig. 6.3. In the 21 DL stripes 7 domain walls can be found.

domain wall (marked (C) in Fig. 7.1) which extends along the $[1\bar{1}0]$ direction (wall normal pointing in [001] direction, i.e. roughly at an angle of 45° to the stripe orientation) exhibiting a width $w_0 = 6 \pm 1$ nm. This type of wall can be found in wider parts of the DL stripes. The minimum distance required to change the magnetization direction is determined by the exchange length $L = \sqrt{A/K}$ [99], where A is the so-called exchange stiffness and K the (effective) anisotropy constant. The result for the wall width is in strong disagreement with a recent publication by Elmers *et al.* [85], in which the DL exchange length was estimated to $L_{\mathrm{DL}} = 0.5$ nm based on Kerr-effect measurements, but it is in accordance to another publication of the same author [96] where a value $L_{\mathrm{DL}} = 3.2$ nm was derived from a micromagnetic calculation. Using the definition $w_0 = 2L = 2\sqrt{A/K}$ our results suggest that $L_{\mathrm{DL}} = 3$ nm. With the DL anisotropy constant $K_{\mathrm{DL}} = 1 \times 10^6$ J/m^3 [76] this leads to an exchange stiffness $A_{\mathrm{DL}} = 9 \times 10^{-12}$ J/m which almost perfectly agrees with the bulk value $A = 1 \times 10^{-11}$ J/m.

At structural constrictions which often serve as pinning centers for domain walls one can find much narrower domain walls as can be seen in the line section shown in the right panel of Fig. 7.2. Typically, the width of domain walls being pinned at structural constrictions amounts to $w^\star = 2 \pm 1$ nm. This behavior has recently been proposed theoretically by Bruno [99]. We have applied Bruno's approach by modelling the width of the DL stripe $S(x)$ by the quadratic approximation $S(x) = S_0(1 + \frac{x^2}{d^2})$ (model II in Ref. [99]). Here, S_0 is the minimum width of the constriction positioned at $x = 0$, x is the distance from minimum, and d is a fit parameter. Indeed, in our case the constriction could well be fitted by using $S_0 \approx 0.8$ nm and $d = 1$ nm
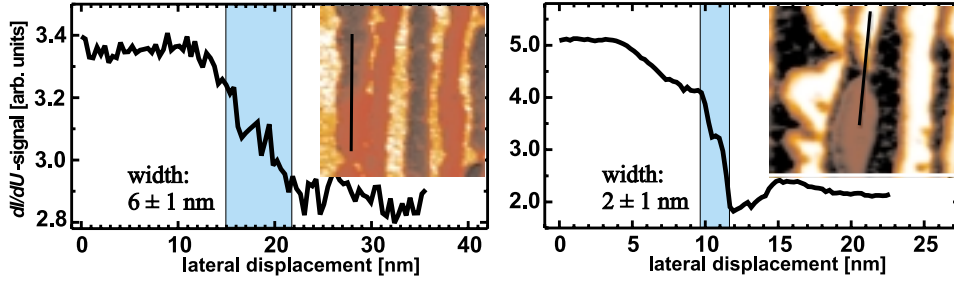
Figure 7.2: Line-sections showing the change of the dI/dU-signal when crossing a domain wall being located in a smooth (left panel) or constricted (right panel) Fe DL stripe. Maps of the dI/dU-signal are shown in the inset.

which results in a reduced domain width $w^\star = 8d/\pi \approx 2.5$ nm being in fair agreement with the experimental observation.

7.2 Simultaneous Imaging of ML and DL Magnetization

The image shown in Fig. 7.3 was measured on substrate #2 exhibiting an average terrace width of 22 nm. It shows an overview of 400×400 nm of 1.5 ML Fe/W(110) recorded at $U = -300$ mV. In this image not only the DL stripes exhibit a strong contrast but also the ML stripes. This latter contrast is absent in the simultaneously recorded map for $U = 700$ mV (not shown here). Obviously, this particular Gd tip has an extraordinary high spin polarization, and it also exhibits an *in-plane component* allowing to image both ML and DL magnetizations simultaneously. This surprising result can be understood if we assume a *canted tip magnetization*.[1] Due to the annealing process after the room temperature deposition of the film the image is governed by the stripe morphology with a few islands still present. A dislocation line found on the large island in the upper left part of the image allows a determination of the [001] direction.

The general magnetic domain structure is characterized by a series of domain walls in both ML and DL stripes along a line roughly in [1$\bar{1}$0] direction which are clearly interconnected. This series of domain walls separates the upper right part of the image from the lower right part by a phase shift so that two *superdomains* emerge, each of them displaying a strictly periodic order of contrasts within both ML and DL; at the boundary of the superdomains a checkerboard pattern emerges. The series of domain walls ends

---

[1] An alternative explanation was recently proposed by Bode *et al.* [100] who interpreted a similar finding for a Fe coated tip in terms of a bias voltage dependent *intra-atomic non-collinear magnetism* of the tip atom. This issue is beyond the scope of the present work and will not be discussed here.
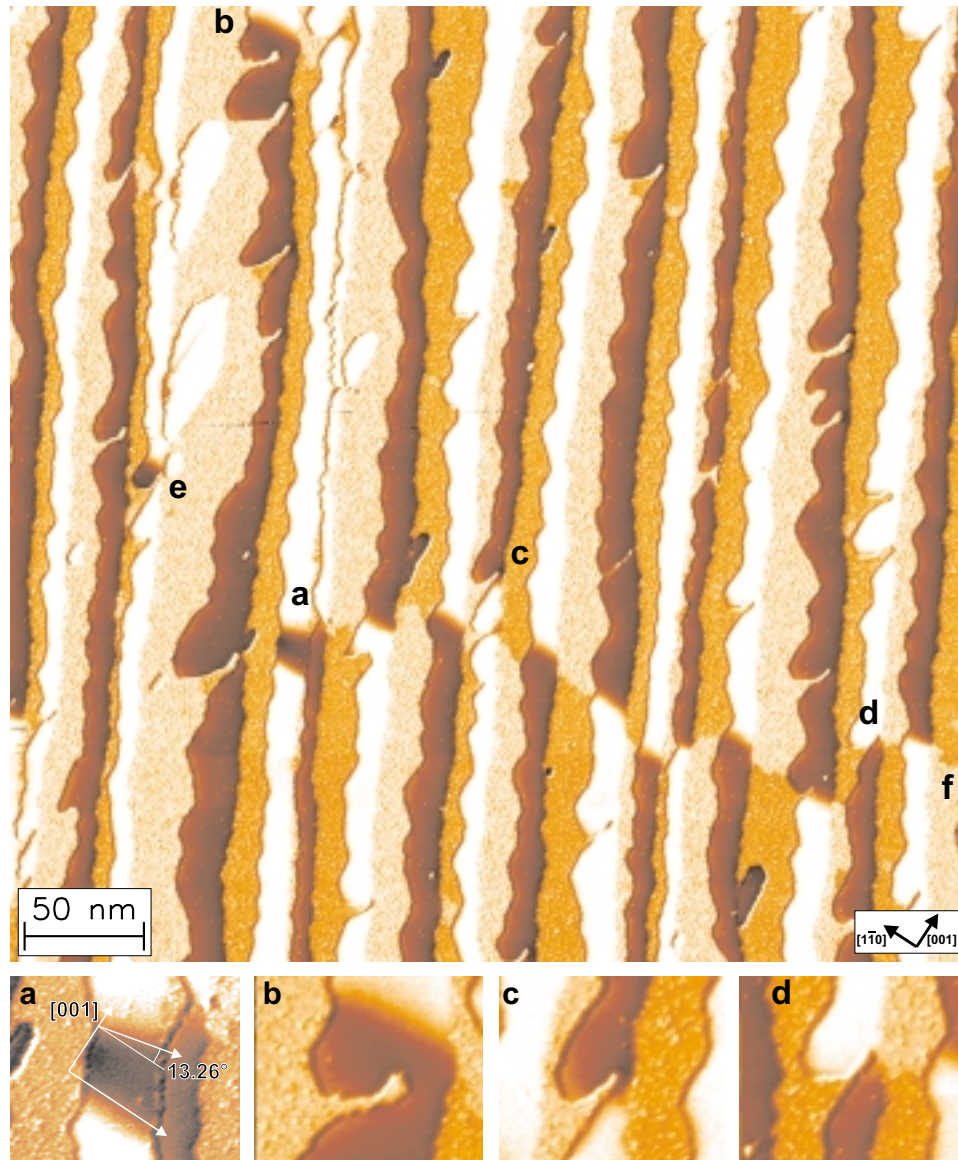
Figure 7.3: Map of the dI/dU signal at $U = -300$ mV. The terraces are wider than in the previously shown examples. A magnetic contrast is found for both, ML and DL stripes. Zoomed views of details marked (a — d) are given at the bottom. Tunneling parameters: $I = 0.3$ nA, $U = -300$ mV.

to the left at a short dark DL domain marked (a), and the contrast periodicity of the upper superdomain is disturbed by two bright DL stripes being exchange coupled to each other due to the vanishing width of the ML stripe between them. As a rule, each dark DL stripe has a dark ML stripe to its right, and each bright DL stripe is neighbored to the right by a bright ML stripe. Consequently, since the next DL stripe to the left of the disturbance is dark and has a domain wall only close to the top edge of the image (marked (b) in Fig. 7.3), the ML contrast follows its DL neighbor up to the top, too, and changes to bright only in close vicinity to the DL domain wall. From this observation we can conclude that it is the DL magnetization which governs the ML magnetization, inducing an *antiparallel* order in adjacent ML stripes as well. This is in contrast to the *parallel* ML stripe order observed in the sub-ML regime by Hauschild *et al.* [82]. Further evidence for the leading role of the DL magnetization comes from considering the fact that the Curie temperatures are different for DL and ML stripes. As has been mentioned earlier, for the extended (i.e. closed) ML a value of $T_{\mathrm{C}}^{\mathrm{ML}} = 220$ K was found [76]. For DL stripes of a width of 5 nm $T_{\mathrm{C}}^{\mathrm{DL}}$ was estimated to 300 K [101], being presumably considerably higher for the wider DL stripes here, hence $T_{\mathrm{C}}^{\mathrm{DL}} > T_{\mathrm{C}}^{\mathrm{ML}}$. After the sample is annealed at $T \approx 550$ K it is introduced into the cold microscope where it undergoes a rapid cooling process (thermal equilibrium at $T = 14$ K is reached in ≈ 1 h). Thus, when $T_{\mathrm{C}}^{\mathrm{ML}}$ is reached the DL stripes are already ferromagnetic and have attained their particular interstripe antiferromagnetic domain order. It is thus very likely that the ML is magnetically driven by the DL, and not *vice versa*. When the ML becomes ferromagnetic the stray field of the DL stripes is already present, and the stray field lines are, except in the vicinity of a DL domain wall, predominantly directed from one DL stripe to the next, i.e. along [1$\bar{1}$0]. This is also the easy axis direction of the ML magnetization. For an unsupported film no directional preference would be expected to result in the ML from the stray field since field lines would equally be present above and below the ML area, and the action of both stray field contributions cancels for a stripe of monatomic height. In our case, however, the film has a vacuum interface on the top side and the nonmagnetic W substrate interface at the bottom side.

A possible explanation of the ML–DL correlation would be an induced polarization of the topmost W layer giving rise to an asymmetry by providing a field line guide in the W interface layer which is absent at the top side vacuum interface. Such a polarization effect has indeed been predicted in a theoretical study of 1 ML Fe/W(110) by Soon C. Hong and A.J. Freeman [102] using the full-potential linearized augmented plane wave (FLAPW) method within the local-spin-density (LSD) approximation. According to this paper the huge lattice strain of the Fe layer leads to a downward relaxation of 9.5 % as compared to the averaged Fe–Fe and W–W bonding lengths resulting in a reduction of the Fe magnetic moment to $2.18\mu_{\mathrm{B}}$ (as compared to $2.65\mu_{\mathrm{B}}$
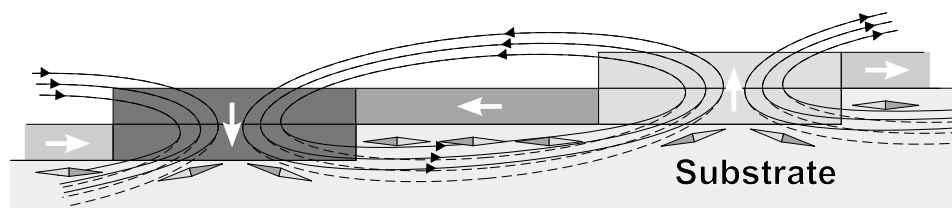
Figure 7.4: Schematics of a possible mechanism inducing a directional preference of the ML arising from a symmetry breaking of the DL stray field lines, acting on the ML, due to a magnetically polarized W interface layer. Dashed lines indicate symmetric field line paths, and full lines represent field line deviations arising from the polarized layer.

for the Fe surface terminating a bulk Fe crystal). This effect is attributed to strong hybridization of the Fe $3d$ and W $5d$ bands, which, on the other hand, gives rise to a small but significant negative magnetic moment of $-0.1\mu_{\mathrm{B}}$ of the topmost W interface layer. If such a polarization, albeit small, is given, the stray field lines are no longer symmetric on either side of the ML so that a net stray field effect is given inducing an alternating directional preference in accordance to the conditions determined by the DL stray field. A schematic presentation of the supposed model is shown in Fig. 7.4.

In any case, the effect on the ML orientation cannot be strong. This can be concluded from the following experimental facts. On close inspection of Fig. 7.3 one can find in the ML stripes, which in general appear magnetized quite homogeneously, a number of small patches showing a contrast in opposition to their local ML environment. In Fig. 7.5 a few examples are presented in an enlarged view, marked by arrows. Most of of these patches show a quite irregular shape without a noticeable preferred orientation of their bounding domain walls. An occurrence of opposite magnetization is obviously favoured in the funnel-shaped bay formed by the DL stripe in the center of Fig. 7.5. A few more examples of this type can be found in Fig. 7.3. In order to rule out a possible misinterpretation of the observed contrasts due to surface roughening by the visible adsorbates I have measured the averaged signal intensities in one patch in comparison to the surrounding extended ML domain in boxes containing 14×12 pixels^2 (1 pixel $\approx 4\text{Å}^2$) as presented in Fig. 7.6. Each of the 14 data points correspond to an average over a column of 12 pixels in vertical direction, the error bars indicate the dispersion within the respective column, and the red lines are linear fits to the data points. The data clearly show a two-stage contrast, and the averaged intensity found in a patch matches that of an extended domain of the same color.

A qualitative explanation for the existence of these patches can be derived from assuming internally exchange coupled ML *spin blocks* of full ML stripe width W_{ML} and length L which increases with decreasing temperature, as proposed by Hauschild *et al.* [82]. In this picture, the magnetization of a ML
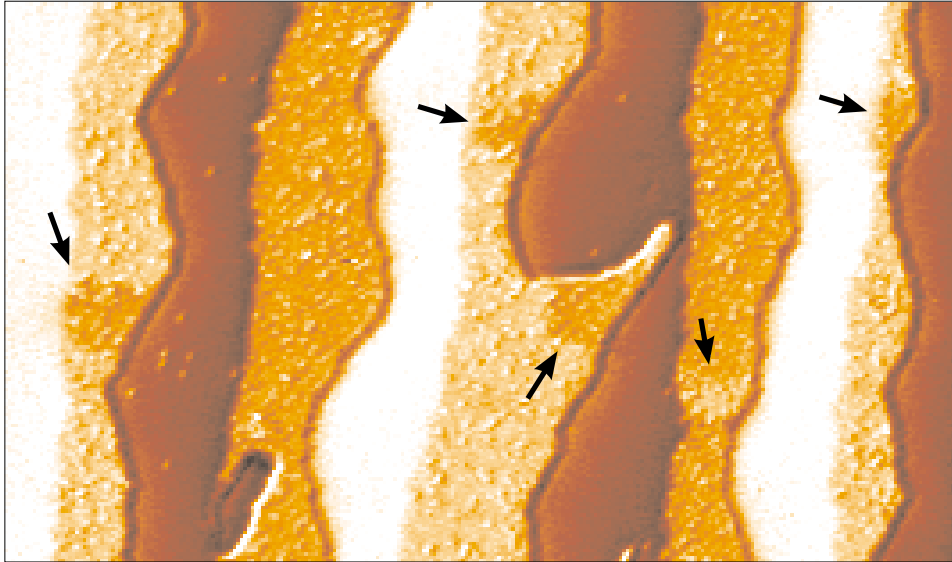
Figure 7.5: ML patches of opposite magnetization within homogenously magnetized ML stripes. They presumably result from magnetic freezing during the rapid cooling process.
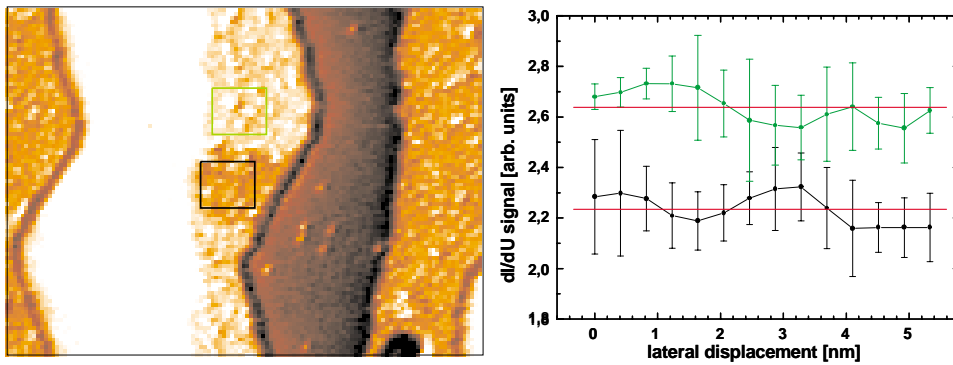
Figure 7.6: Comparison of the dI/dU signal intensities in an extended ML stripe and in a patch of opposite magnetization as measured in the green and black boxes. Data points represent an average over a vertical column of 12 pixels, error bars indicate the dispersion within the respective column.

stripe decays exponentially due to thermally activated fluctuations of the blocks, with a relaxation time τ increasing with decreasing T resulting in a freezing-like transition to a permanently magnetized state below an effective freezing temperature $T_\tau(W_{\mathrm{ML}})$ as a function of the ML stripe width W_{ML}, and τ is governed by the activation energy for spin block generation. For the sub-ML regime it has been shown [82] that $T_{\mathrm{C}}(W_{\mathrm{ML}}) > T_\tau(W_{\mathrm{ML}})$ so that at decreasing temperature the system can order ferromagnetically by dipolar interaction of neighboring ML stripes before it freezes. In our case, replacing the ML–ML dipolar interaction by a ML–DL dipolar interaction explains the observed antiferromagnetic ordering of adjacent ML stripes driven by the DL stray field. Further, considering the rapid cooling process it appears reasonable that the ordering process may locally remain incomplete, depending on the time available for ordering which can occur only in the temperature window $\Delta T = T_{\mathrm{C}}(W_{\mathrm{ML}}) - T_\tau(W_{\mathrm{ML}})$. Below T_τ the system lacks the activation energy required to overcome the energy barrier $\Delta E > k_{\mathrm{B}} T_\tau$ separating the two magnetic states and attain the energetically more favourable state of complete order so that patches of opposite magnetization are left over.

7.2.1   Domain Walls

In the following I will first present a number of details found in Fig. 7.3 at DL domain walls, and after that I will focus on domain boundaries observed in ML stripes. Locations marked by letters (a)–(f) in Fig. 7.3 are shown in zoomed views in the bottom panels and in the following figures, respectively.

DL Domain Walls

Most of the DL domain walls clearly show an extension in $[1\bar{1}0]$ direction, but also some examples are found deviating by $\approx 13°$, thus preferring the $[3\bar{3}1]$ direction. This is most clearly seen by comparing the upper and lower wall directions of the short dark domain marked (a) in Fig. 7.3. More examples for such behavior can be seen in Fig. 8.11.

At the location marked (b) a broad DL domain wall is visible spurning the nearby constriction. A contrasting case is found in example (c) at an — albeit much narrower — constriction. In this case, the wall orientation deviates from the $[1\bar{1}0]$ direction and follows the direction enforced by the local morphology. This case resembles the one shown in Fig. 7.2 although the geometry of the constriction is quite different. A completely different situation can be observed at locations (d) and (e). Here, obviously a few atomic rows are missing so that the DL stripe is discontinuous. Since the impact of the short ranged exchange interaction is absent no domain wall is formed at all. The effect can be studied more quantitatively by inspection of Fig. 7.7, recorded at location (e), where a standard wall can be compared to a transition across missing atomic rows. The latter takes place over a
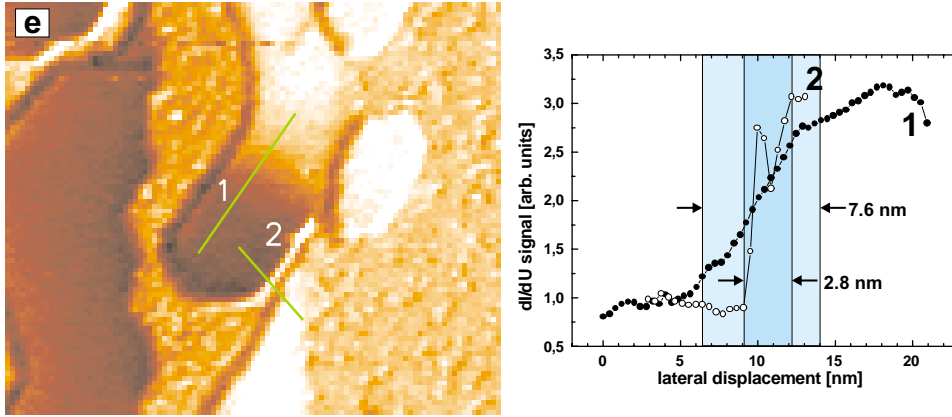
Figure 7.7: Comparison of the dI/dU signal transition lengths across a standard DL domain wall to that across some missing atomic rows. In the absence of exchange interaction oppositely magnetized DL areas can get extremely close.

length of 2.8 nm i.e. less than half the width of a standard domain wall. Using the W row distance $a_W/\sqrt{2} = 2.24$ Å in [1$\bar{1}$0] direction and correcting for artifacts due to scanning at step edges I estimate the number of missing rows to $n < 10$. Given the condition of a few missing rows, areas of opposite magnetization can approach each other extremely close.

ML Domain Boundaries

From Fig. 7.3 it is already clear that the domain boundaries found on ML stripes are much sharper than those of the DL stripes. This can be seen in more detail in Fig. 7.8(a) which was recorded at an even higher resolution of 1 Å pixel^{-1}. Sections (b) and (c) have been taken to the same lateral scale along the lines shown in the image. They reveal the ML walls to be an order of magnitude narrower than those of the DL layer, $w_{ML} = 0.8$ nm. The measured value may even be broadened by the adsorbates in close proximity. Since the line sections were taken in [001] direction and considering the W lattice constant of $a_W = 3.165$ Å the surprising result is a 180° spin rotation over a distance of 2-3 atomic rows. This observation suggests to raise the question if the transition between the oppositely magnetized ML areas can properly be called a domain *wall* in the sense of a continuous spin rotation. Instead, an Ising-like *discontinuous switching* has to be considered. In Ising's thermodynamical model [103], the spins can only have the values ↑ or ↓. Regarding the uniaxial in-plane anisotropy with a strong anisotropy field of the order of 5 T [82], this means a magnetization in either [001] direction or opposite. Additional evidence for such a behavior can be found from the paths of the boundaries shown in Fig. 7.8(d) and (e); (d) is taken from location (f) in Fig. 7.3, and (e) is an enlargement of the boundary in
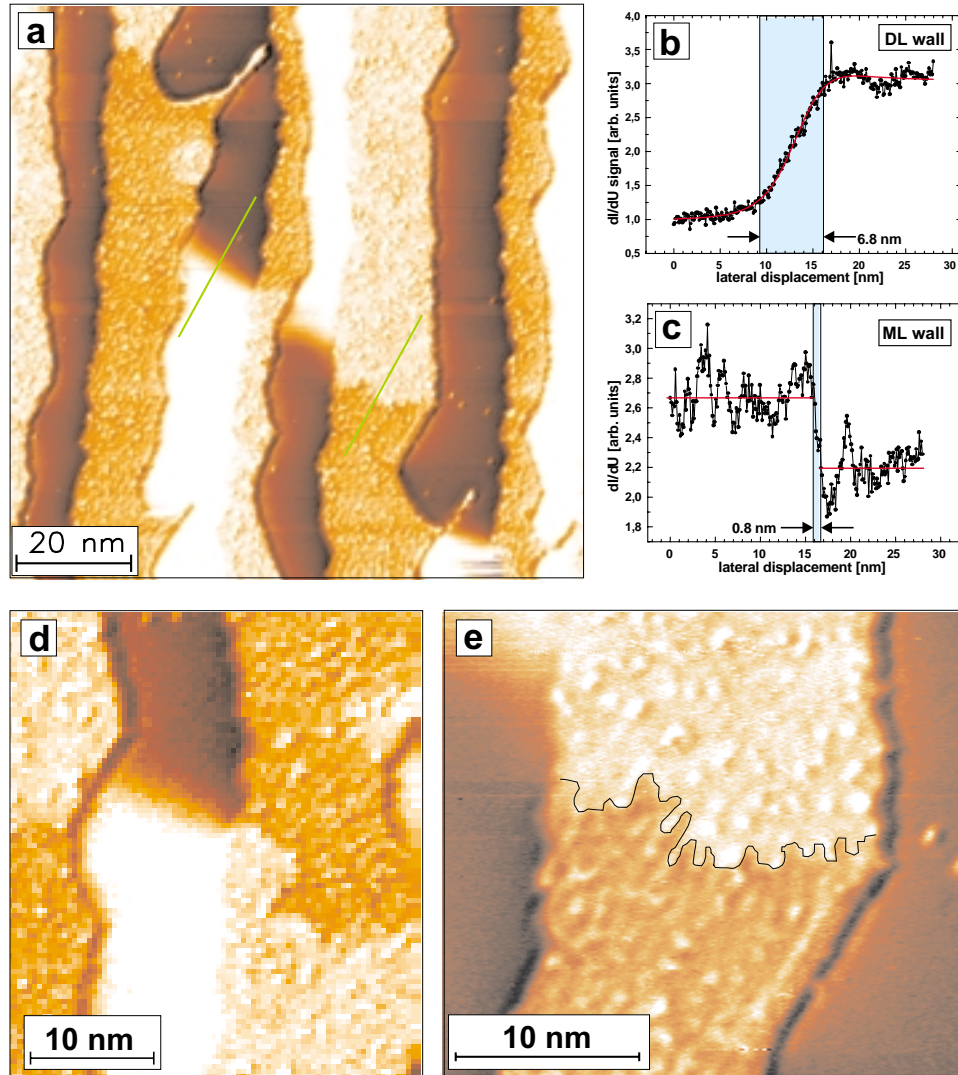
Figure 7.8: **(a)** High resolution image of 1.5 ML Fe/W(110). Scan range is 100×100 nm². 1 pixel corresponds to 1 Å². **(b–c)** Comparison of the DL domain wall width to the domain boundary separating ML domains, taken along the lines in **(a)**. For the latter the measured value suggests a 180° spin rotation over a distance of 2-3 atomic rows. **(d)** ML domain boundary from Fig. 7.3, location marked (f). **(e)** Zoom of the boundary in panel (a). Pinning at adsorbates strongly influences the detailed path at a sub-nanometer length scale. Tunneling parameters: $I = 0.3$ nA, $U = -300$ mV.

Fig. 7.8(a). We note the bizarre path of the boundary in (d) reminiscent of a random walk. In (e) the domains appear clasped into each other with the aid of adsorbate pinning centers. As a guide to the eyes, I have drawn a contour line separating the two domains. The details of the paths on a sub-nanometer scale are strongly determined by pinning. This observation can hardly be reconciled with the concept of an ordinary domain wall with a continuous transition from one magnetic state to the other at any reasonable length scale. On the other hand, the assumption of a discontinuous switching at the atomic scale implies a spin frustration all along the domain boundary. The problem remains to be resolved by further investigations.

Chapter 8

Field Dependent Measurements

The ultimate proof that the contrasts observed are really of magnetic origin is given if an external field is applied to the sample and the domain structure can be watched changing accordingly. SP-STM not only simultaneously provides images of the magnetization and the topography at the ultimate length sale and also spectroscopic data of the electronic structure at the Fermi energy by which the magnetic properties of the sample are determined. It is also a unique technique in that it allows measurements with a magnetic field applied. In this chapter I will describe experiments studying the magnetization reversal of the Fe/W(110) system of nanowires.

8.1   The Development of the Domains

As an introduction, the sample we will be concerned with on the next few pages is presented in Fig. 8.1 both in a topographic image (a) and in a dI/dU map (b). The scan range is 200 nm × 200 nm. The Fe film with a nominal thickness of 1.65 pseudomorphic atomic layers was deposited onto substrate #1 exhibiting a terrace width of 9 nm on average. At the chosen coverage the DL stripes have an average width of 5.8 nm and a variation of local widths in a range between 10 nm and less than 2 nm. During growth the single crystal was held at a temperature $T = 450 \pm 50$ K, with no additional anneal. In all measurements tip and sample had a temperature of $T = 14.5 \pm 1$ K. The W tip in use had a coating of 8 ± 1 ML Gd providing sensitivity to the perpendicular component of the sample domain structure.

Fig. 8.1 presents the magnetic virgin state before exposition to an external field. ML stripes appear as black lines. In the DL stripes we again find an alternating order of bright and dark domains confirming the antiparallel coupling of adjacent stripes. The contrast distribution is nearly balanced. The 23 visible stripes exhibit 15 domain walls, and a certain tendency to form spatial correlations of domain walls among neighboring stripes in a checkerboard manner can be recognized. The widths of the walls confirm
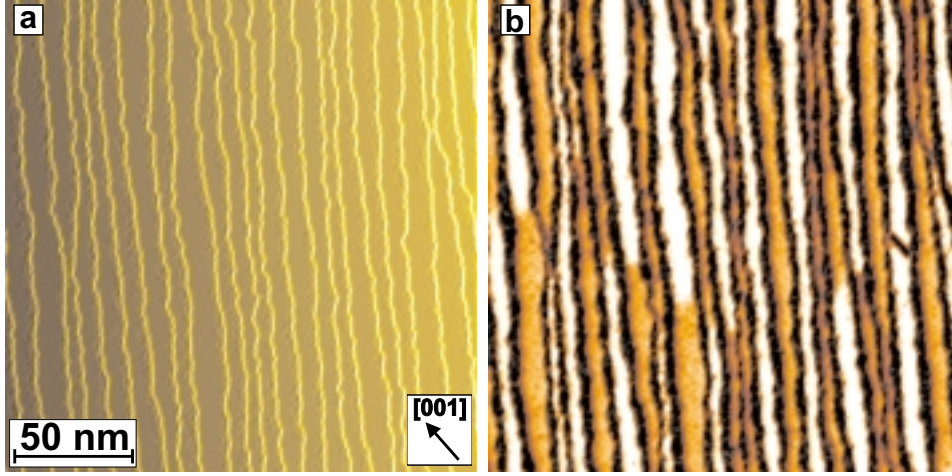
Figure 8.1: Topography and dI/dU map of the virgin state. The 23 DL stripes exhibit 15 domain walls, the average domain length estimated from the visible area is thus roughly 300 nm. Tunneling parameters: $I = 0.5$ nA, $U = +700$ mV.

the previously reported result of 6 ± 1 nm.

Fig. 8.2 shows the full series of 24 images taken at magnetic field strengths in the range of ± 400 mT, applied perpendicular to the sample plane. Panels (a) to (x) show the development of the domains as a function of the external magnetic field. With increasing positive field bright areas grow at the expense of dark areas until, at $+400$ mT, almost all dark DL areas have vanished indicating saturation [Fig. 8.2(f)]. So far, we can identify bright areas as being magnetized parallel to the external field, i.e. *up* ($\uparrow$), while the dark domains are magnetized *down* ($\downarrow$). High remanence is observed [Fig. 8.2(h)].

Taking the step from remanence to -50 mT [Fig. 8.2(h)–(i)] a dramatic change takes place in the distribution of bright and dark. The contrast of all DL stripes is reversed. This can be explained by a switching of the tip's magnetization by the action of the external field from ($\uparrow$) to ($\downarrow$) while the sample remains almost unaffected. As a consequence, at ($\uparrow$) domains the tip-sample configuration is changed from ($\uparrow\uparrow$) to ($\downarrow\uparrow$), and the opposite happens for ($\downarrow$) domains where ($\uparrow\downarrow$) is changed to ($\downarrow\downarrow$). This is the cause of the contrast reversal.

A further field increase in $-z$ direction leads again to a growth of bright DL domains until, at -400 mT, saturation in the negative direction is reached, again with no dark domains left [Fig. 8.2(o)]. At $+50$ mT the tip has switched again [Fig. 8.2(p)], symmetrical to the previous switching event, and the effect on the images is analogous. This observation allows an estimate of the coercive field for the Gd tip, $\mu_0 H_C^{\mathrm{tip}} \leq 50$ mT.
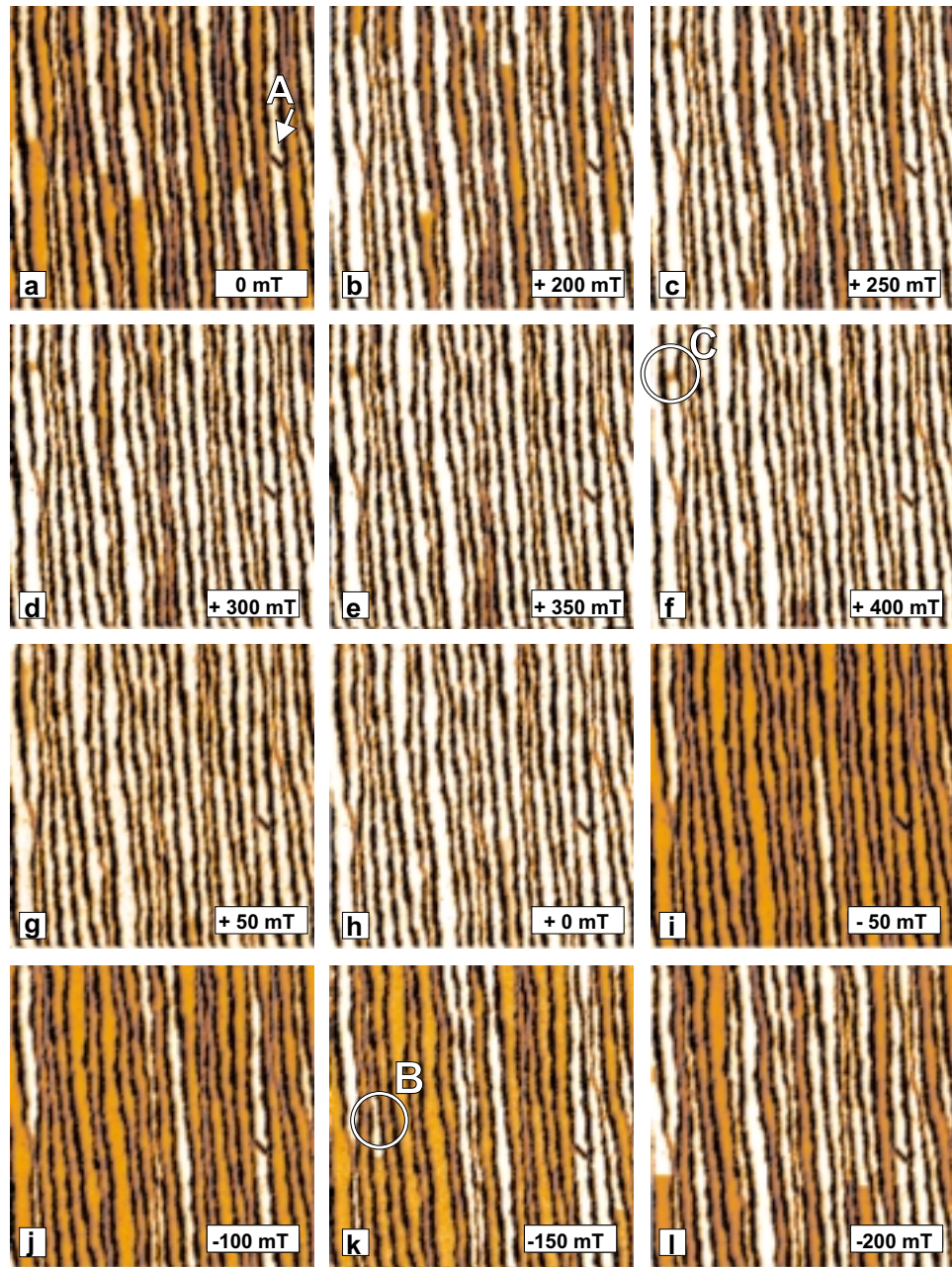
Figure 8.2: Series of 24 dI/dU images taken at field values as indicated. As a guide to the eyes, a dislocation line (A) is marked. Circles (B) and (C) refer to the enlarged views given in Figs. 8.4 and 8.5.
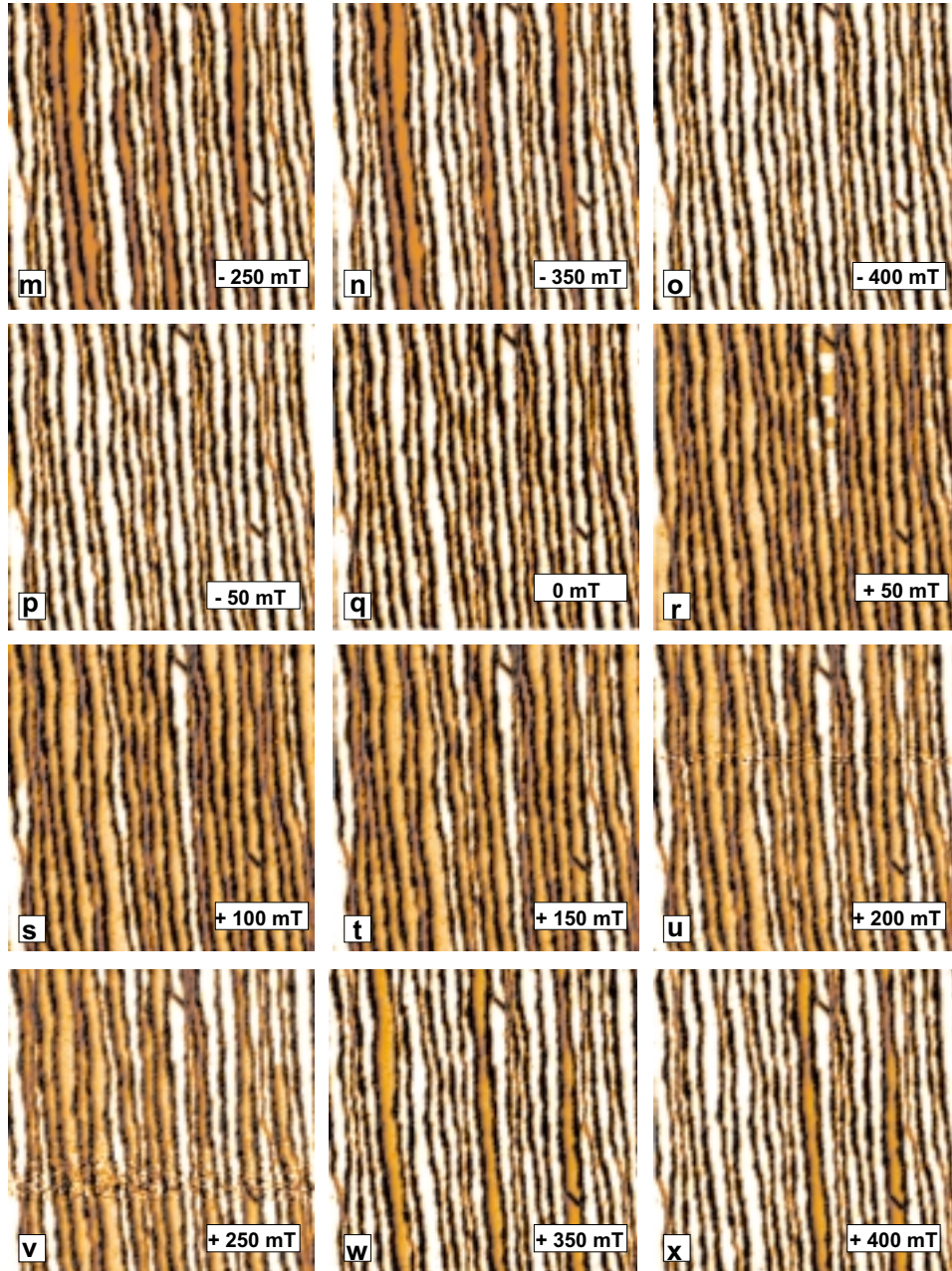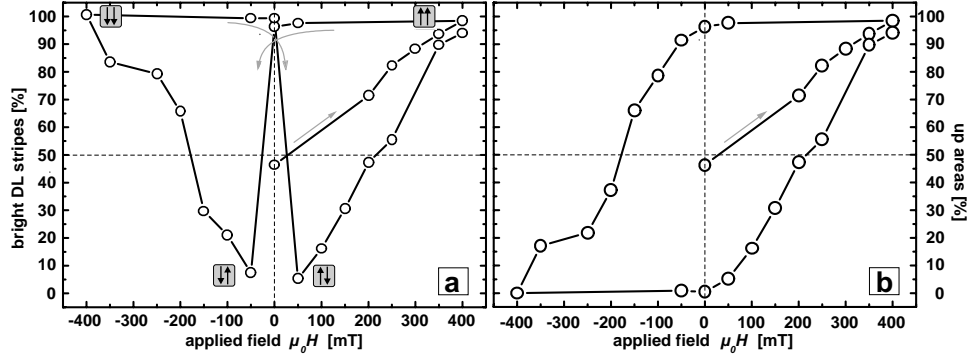
Figure 8.3: Hysteresis curves obtained from the distribution of (**a**) bright domains and (**b**) stripes with $+z$ magnetization ($\uparrow$). The butterfly curve (**a**) shows properties of the complete tunneling junction consisting of two ferromagnetic electrodes, while the curve (**b**) displays only sample properties. Arrow panels indicate the relative alignment of tip and sample magnetization.

8.1.1   Hysteresis at the Nano-Scale

From evaluating the *bright* DL stripe length percentage we obtain the butterfly hysteresis curve displayed in Fig. 8.3(a). The shape of this curve results from the fact that *two* ferromagnetic electrodes are involved, namely tip and sample. Taking the effect of tip switching into account *pure sample properties* can easily be separated. They are represented by the second hysteresis curve, Fig. 8.3(b), which displays the percentage of ($\uparrow$) domains as a function of the applied field. A remanence-to-saturation ratio $M_{\mathrm{R}}/M_{\mathrm{S}} \approx 0.98$ is observed. Sample coercivity is found at $\mu_0 H_{\mathrm{C}}^{\mathrm{sample}} \approx 225 \pm 25$ mT and is best matched in Fig. 8.2(u-v). Comparing these frames to the initial demagnetized state, Fig. 8.1, we observe that the detailed magnetic order of the stripes has changed significantly. No domain wall can be found at its initial location. This is not surprising, since the existence of a hysteresis is already a consequence of the irreversibility of the remagnetization process. The initial contrast pattern alternating from one stripe to the next is replaced by an occurrence of bunches of two, three or even four stripes of the same magnetization next to bundles of stripes of opposite magnetization. The dipolar order has coarsened significantly. This behavior can be attributed to the different history of these demagnetized states. The initial order was formed when the sample was cooled down from its growth temperature to 14.5 K. At the DL Curie temperature $T_{\mathrm{C}}^{\mathrm{DL}} = 300$ K [101] the thermal energy is of a magnitude comparable to that of the magnetization-related energy contributions. This supports the formation of a fine-sized equilibrium order such that the stray field energy is minimized. This effect of thermal energy on domain wall mobility is greatly reduced at low temperatures. The virgin state emerged from a transition from the *paramagnetic phase* with no magnetic
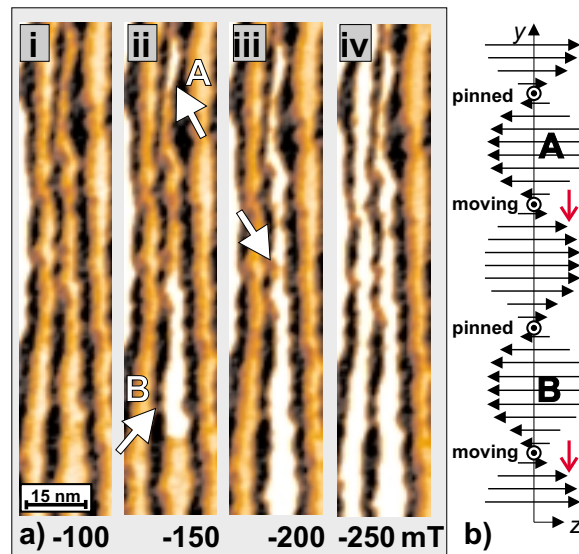
Figure 8.4: **(a)** Creation and annihilation of domains. Two new bright domains (A) and (B) are being created, bounded by Bloch walls. The lower wall of (A) moves towards (B), the trapped dark area shrinks. The last dark portion is marked in (iii), immediately before it gets annihilated. **(b)** Sketch of the magnetization reorientation process. Black arrows indicate the perpendicular component of the magnetization. Note the vector orientation in the wall centers, all pointing into the same direction. The new domains will again be annihilated on field reversal.

order while coercivity was preceded by *saturation* with all domains perfectly aligned, i.e. maximum magnetic order.

8.1.2 Mechanisms of Magnetization Reversal

The general shape of the hysteresis loop of Fig. 8.3(b) is not a simple square loop but shows a slope. It is thus clear that the magnetic reorientation does not take place in a single jump from one saturated state to the opposite one but progresses successively. Except for the weak spatial correlations of domain walls mentioned earlier caused by dipolar interaction, the DL stripes are found to be effectively decoupled even by ML stripes as narrow as ≈ 1.5 nm. Every single stripe is remagnetized individually. Two mechanisms of remagnetization are observed, *domain creation* and *domain wall motion*. Wall motion is restricted to the direction along the stripe. Both mechanisms are illustrated in Fig. 8.4(a), taken at the location marked (B) in Fig. 8.2. Two new domains (A) and (B) are created. Since the spins have to rotate continuously at both domain ends the magnetization vectors at the wall centers point into the same direction in both walls. In other words, the sense of rotation within the two Bloch walls bounding a new domain must be opposite, namely clockwise and counterclockwise. This situation is depicted

schematically in Fig. 8.4(b).

With increasing field, the lower wall of domain (A) moves towards domain (B). Finally, (A) and (B) merge, which is equvalent to an annihilation of the dark domain trapped between them. In panel (iii) the last dark portion, marked by an arrow, is visible just before it vanishes. From the viewpoint of the dark domain, its bounding walls get unwound. On field reversal, the new bright domain will also be annihilated because the same arguments apply.

8.1.3   Residual Domains

In Fig. 8.2(c)–(f) a dark spot marked (C) is present which is a relict of the dark domain visible in Fig. 8.2(b). This spot retains its size and position regardless of the increasing field and serves as a nucleation center for an extended dark domain in this particular wire at decreasing field [Fig. 8.2(g)]. An enlarged view of this small domain is presented in Fig. 8.5(a). Its surprising stability can be understood in the following way: Due to the increasing field a dark domain has shrunken. Its two domain walls approach each other and end up in direct contact. However, the domain can only be annihilated if the sense of rotation within its bounding walls is opposite. This was the case in the previously discussed example. If, on the other hand, both walls exhibit the same sense of rotation the result is a total spin rotation of $360°$ which is inherently stable in an external field. To overcome such a configuration a breakdown process is required, with external fields equal to the exchange field B_{ex} the order magnitude of which can be estimated by considering that the exchange energy is about equal to the thermal energy at
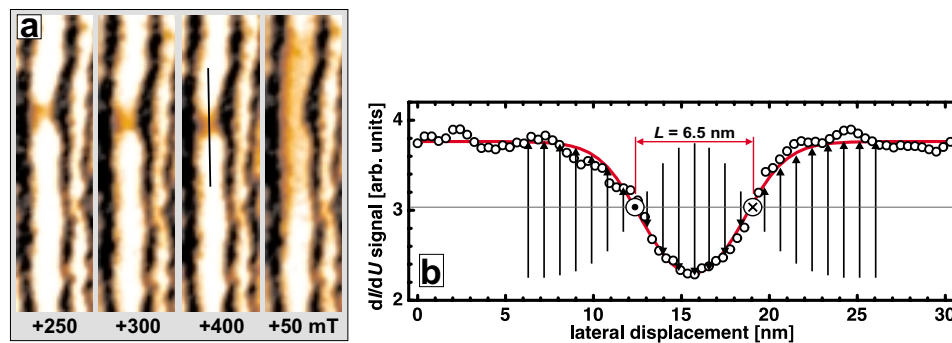
Figure 8.5: **(a)** A residual domain resulting from two winding $180°$ Bloch walls. The walls have been forced together by the external field. As soon as the field strength is released an extended dark domain grows. **(b)** Section taken along the line in **(a)**, arrows indicating the perpendicular magnetization component. In the wall centers, the magnetization vectors point in opposite directions such that, in total, a $360°$ spin rotation is given. This configuration is inherently stable in an applied external field and thus provides the smallest possible domain with a magnetization opposite to the field.

the Curie temperature,

$$E_{\mathrm{ex}} \approx \mu_{\mathrm{B}} B_{\mathrm{ex}} \approx \mathrm{k}_{\mathrm{B}} T_{\mathrm{C}},$$

with $\mu_{\mathrm{B}} = 0.579 \times 10^{-4}$ eV/T the Bohr magneton and $\mathrm{k}_{\mathrm{B}} = 0.862 \times 10^{-4}$ eV/K the Boltzmann constant [104]. Taking $2.2\mu_{\mathrm{B}}$ for Fe instead of μ_{B} and $T_{\mathrm{C}}^{\mathrm{DL}} = 300$ K for 5 nm stripe width [101], we obtain $B_{\mathrm{ex}} \approx 200$ T, a value not accessible by laboratory magnets. The actual value remains to be investigated and may be considerably smaller due to the reduced number of nearest neighbor atoms in a film as thin as two ML (6 instead of 8 in the bulk), this number being even more reduced to 3 at the step edges, but B_{ex} may still be large. In this picture the smallest possible stable domain exhibiting a magnetization direction opposed to the external field is the result of two 180° walls forced together in a winding process by the external field. We have fitted two tanh standard wall profiles [105] to the dI/dU signal assuming a 360° rotation, see the red line in Fig. 8.5(b), thereby determining the length of the residual domain as $L_{\mathrm{rd}} = 6.5 \pm 0.5$ nm. The observation of residual domains suggests a rather simple but natural view on the saturated state and the initial nucleation process that starts the magnetization reversal. Saturation is obtained when only residual domains are left in the sample.[1] Such domains serve as seeds for a magnetization reversal.

A schematic side view of pairs of unwinding and winding walls, respectively, is depicted in Fig. 8.6. When seen from the right hand side, the spins in the unwinding case first rotate counterclockwise and then clockwise in the next wall. In the winding case, the rotation is counterclockwise in both walls. A representation of the contrast distribution as observable by a tip with perpendicular magnetization is given in Fig. 8.6 by the small boxes (shown in top view). Both types of walls look the same. If the field B is applied in the upward direction all four walls shown will move towards the center, i.e. the dark domain shrinks. If the walls are of the unwinding type the domain will be annihilated, in contrast to the winding case.

As has been mentioned, using a tip sensitive only to the perpendicular component of the sample magnetization we will not be able to distinguish beween winding and unwinding walls. This should be, however, possible with a tip sensitive to the in-plane component since in a pair of unwinding walls the magnetization vectors at the wall centers point into the *same* direction whereas they point into *opposite* directions in pairs of winding walls. This issue will be scrutinized in the following section, and we will examine if the residual domains are as stable as is suggested by the reasoning above.

---

[1]This statement will be modified in Section 8.3.1.
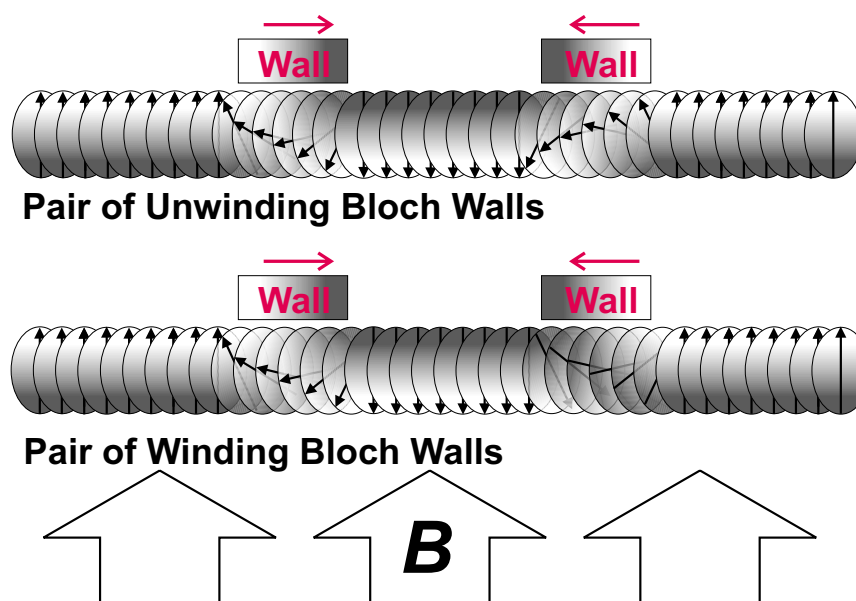
Figure 8.6: Side view of unwinding and winding Bloch walls under the action of an external field. Unwinding walls lead to domain annihilation. Domains bounded by winding walls are stable to a high degree. Small boxes represent a top view of the walls' color gradient as obtained when imaged with a tip of perpendicular magnetization; they cannot be distiguished.

8.2   Tips with In-Plane Anisotropy

In residual domains the requirement of a 360° spin rotation implies that, at the wall centers, the magnetization vectors lie in the sample plane pointing in *opposite* directions. This can be made visible by using a ferromagnetic tip with easy-plane anisotropy being sensitive to the domain *walls* rather than to the domains. Such tips have been used by Bode *et al.* to image the easy-plane domains of thick Gd films [22]. In order to study the properties of domain walls more closely I will describe experiments in which tips with in-plane anisotropy were used.

For a better understanding of the occurring contrasts it is convenient to first examine the spectra obtained with such tips. This is shown in Fig. 8.7. In this experiment the tip had a coating of 5±1 ML Fe. The colors of the spectral curves in panel (a) correspond to the boxes in panel (b) which indicate the areas of averaging. First of all we note that the *domains* show no contrasts. The yellow and green curves have been measured on domains of opposite out-of-plane magnetization and are virtually identical at all bias voltages. This is indicative for a vanishing perpendicular tip magnetization component. On the other hand, comparing the curves acquired on *domain walls* (blue and red) we find them highly polarized almost over the whole voltage range. Consequently, nearly all maps of the differential conductivity
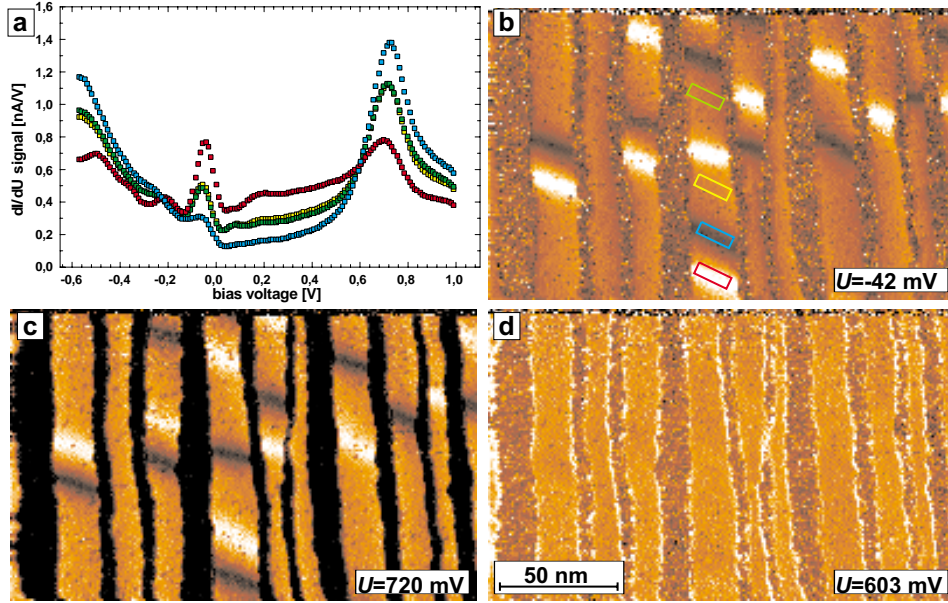
Figure 8.7: **(a)** Spectra recorded using a tip coated by 5±1 ML Fe exibiting a magnetization parallel to the sample plane. The color code corresponds to the colors used in **(b)** to indicate the locations where the spectra have been averaged. While the spectra sampled on *domains* of opposite magnetization are virtually identical (green and yellow) those taken at *domain walls* (blue and red) show a strong spin contrast at the well known DL peak at $U = +720$ mV and a smaller but equally highly polarized peak at $U = -42$ mV. **(b–d)** dI/dU maps taken at the peak positions and at one of the nodes of the curves where all magnetic contrasts vanish. Note the wall contrast reversal in **(b)** and **(c)**.

for any specific bias voltage show a bright–and–dark wall contrast. The two maps shown in (b) and (c) correspond to the energetic positions of the peaks at $U = +720$ mV and $U = -42$ mV, respectively, i.e. above and below the Fermi level located at $U = 0$ mV. All spectral curves intersect at two points, namely -225 mV and $+603$ mV, and at these voltages all DL wall contrasts vanish, as is demonstrated in map (d) for the latter voltage. No contrasts attribuable to a magnetization are found at any voltage on the ML stripes in these spectra. This result is in agreement to MOKE measurements by Elmers *et al.* [85] who found only a paramagnetic in-plane signal in a coverage range of $1.5 < \Theta < 2$ ML.

Inspecting maps (b) and (c), we note that the wall contrasts are reversed. This is a result of the already mentioned crossover of the corresponding curves. This behavior indicates an inversion of the tunnel magneto-resistance (TMR). Since we have two intersections in the curves, the energetic range can be subdivided into three regions: (I) $eU < -225$ meV, (II) $-225 < eU < +603$ meV, and (III) $eU > +603$ meV. As a consequence, either in region (II) we have *normal* TMR (which is given if the resistance is lower for a
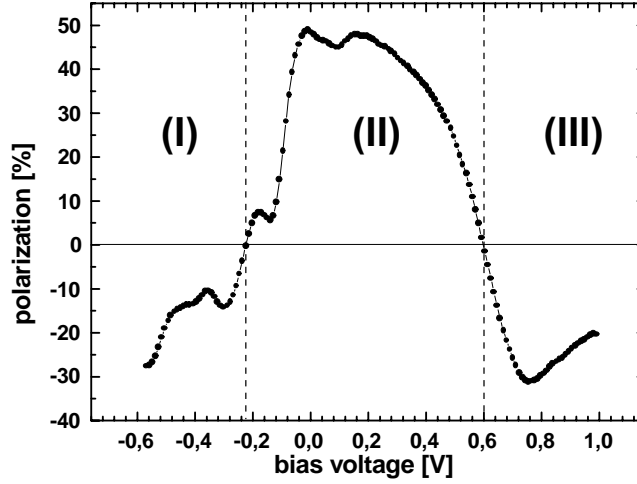
Figure 8.8: Polarization of the tunnel junction of tip and sample at domain wall locations. Note that the experiment does not allow to determine the sign of the polarization.

parallel magnetization of the two electrodes as compared to the *antiparallel* alignment) and *inverse* TMR (given if the *antiparrallel* configuration exhibits the lower resistance) in regions (I) and (III), or *vice versa*. In Jullière's model [106] the TMR ratio is given by $\Delta R/R = (R_{\uparrow\downarrow} - R_{\uparrow\uparrow})/R_{\uparrow\downarrow}$. As the resistance R is inverse to the conductance, $G = 1/R$, we can use this quantity in an equivalent expression which is more appropriate here since our signal is the differential conductance. According to Slonczewski's formulation [107] the TMR ratio is then given by

$$\text{TMR} = \frac{\Delta G}{G} = \frac{G_{\uparrow\uparrow} - G_{\uparrow\downarrow}}{G_{\uparrow\uparrow}}, \tag{8.1}$$

where G denotes the conductance of the tunnel junction, which is related to the spin polarization P of the tunneling junction, shown in Fig. 8.8 as a function of bias voltage, by the equation

$$\frac{\Delta G}{G} = \frac{2P_1 P_2}{1 + P_1 P_2}, \tag{8.2}$$

where P_1 and P_2 denote the polarizations of the two electrodes, respectively, and $P = P_1 P_2 \cos\varphi$ according to Eq. (2.27). Taking the values shown in Fig. 8.8 and assuming perfect alignment, $\cos\varphi = \pm 1$ we yield a TMR ratio of 65 percent in the range of -20 mV$< U < +200$ mV. In analogy to the considerations made in Chapter 2, p. 21, concerning the superiority of a spectroscopic approach to spin polarized tunneling against constant current imaging the measurement of the *differential conductance* allows a much more

detailed view onto the relevant properties.[2] The questions related to the systematic study of TMR are, however, beyond the scope of the present work.

While for the earlier discussed case of the *domains* we can decide whether tip and sample are in a parallel or antiparallel alignment by applying an external field, this is not possible for the domain *walls*, since, on applying the field, they will only move back or forth without revealing their *absolute* magnetization direction. Even if we knew the azimuthal magnetic orientation of the tip (in the present experimental setup this is not possible for the in-plane case) we cannot easily decide if a bright domain wall is indicative for a parallel alignment since the same wall shows up dark at a different bias voltage. However, in all our experiments we found a strict alternating order of contrasts for the walls inside a particular stripe, i.e. the magnetic ground state is characterized by walls of only the *winding* type. In other words, within any individual stripe, the *sense of spin rotation does not change*. This is conceivable if we consider a higher mobility of walls with the aid of thermal energy during earlier stages of the cool-down process leading to an easy annihilation of domains bounded by walls of the *unwinding* type thus leaving only winding walls.

In Fig. 8.9 again two simultaneously measured dI/dU maps are presented, recorded using a Fe coated tip. Panel (a), taken at $U = -100$ mV in the backward scan direction (right to left), shows the domain wall contrast we are by now familiar with. In panel (b), taken at $U = +150$ mV in the forward scan direction, the wall contrasts again show up inverted. The most surprising observation is, however, to find (b) clearly dominated by a *domain contrast* indicating that the tip exhibits a perpendicular magnetization component at +150 mV which cannot be observed at -100 mV. This finding was explained in a recent publication by Bode *et al.* [100] in terms of a *voltage dependent intra-atomic non-collinear magnetization of the tip*, a novel effect that will not be discussed here. However, now that we are having information at hand acquired simultaneously for the walls and for the domains, we observe that the contrasts of domains and walls follow — without any exception — a particular order. We can model this finding by

---

[2]In TMR experiments *planar* tunnel junctions are studied consisting of (at least) two magnetic thin film layers separated by an insulating barrier. Devices based on the TMR effect are of high technological relevance for magneto-electronics, e.g. in the development of non-volatile MRAMs. As has been pointed out by Wiesendanger *et al.* [108], SP-STS has a high potential in the study of TMR related problems since it is able to provide information on two main issues: surface roughness, and domain reorientation. Especially the possibility to replace (i) the insulating barrier film by a vacuum gap and (ii) the counterelectrode by a tip of constant polarization mimicking a 2-dimensional interface by the process of scanning allows to separate effects inherent to the ferromagnetic electrodes from those due to barrier imperfections.
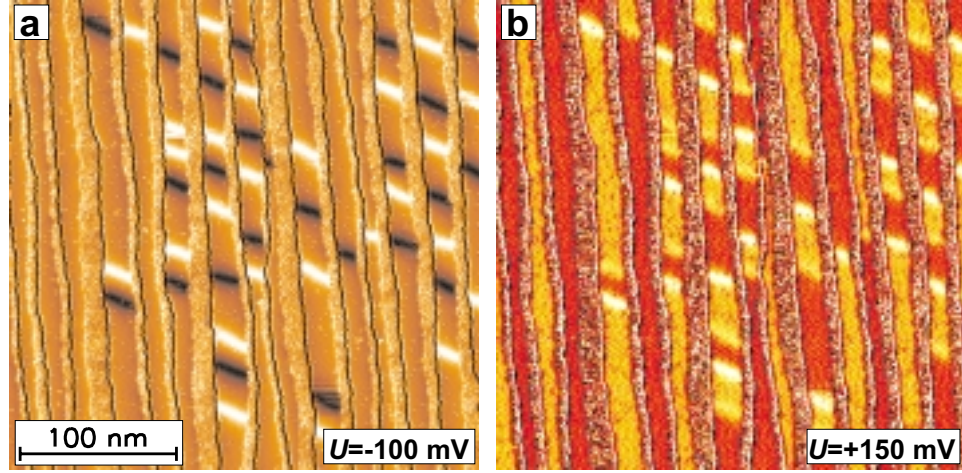
Figure 8.9: Simultaneously recorded dI/dU maps measured using a Fe coated tip at the bias voltages indicated. In (a) contrasts are found in domain *walls*. (b) also shows some (inverted) wall contrast, but is clearly dominated by *domain contrast*.

a sequence of domains and walls ordered in the following manner:

$$D - d - L - l - D - d - L - l - D - \ldots \qquad (i),$$

where capital letters D (L) symbolize the domains (**D**ark and **L**ight) and small letters d (l) stand for domain walls (**d**ark and **l**ight). An alternative sequence would be

$$D - l - L - d - D - l - L - d - D - \ldots \qquad (ii),$$

which is the same sequence as (i) if we read it from right to left. But let us look at both of them from the same viewpoint. If we assign a clockwise (cw) rotation in the domain walls to sequence (i) (this choice is arbitrary) then sequence (ii) is the result of a counterclockwise (cc) rotation, and we can write the sequences as

$$D - cw - L - cw - D - cw - L - cw - D - \ldots \qquad (i),$$
$$D - cc - L - cc - D - cc - L - cc - D - \ldots \qquad (ii).$$

Since *all* domains appearing dark in panel (b) are bounded at their lower ends by *bright* walls, and at their upper ends by *dark* walls we know that only one of the two sequences is observed. As a consequence, we also observe only one sense of rotation, and it is equal for *all stripes*. This is a quite unexpected result, since left hand or right hand spin rotation should be energetically degenerate, and hence an occurence of both cases should be observed at random. Instead, we find a new type of long range order the cause of which presumably lies in some asymmetry of the system favouring one sense of rotation over the other the exact cause of which remains to be investigated.

8.3 Imaging Magnetic Properties Using Non-Magnetic Tips

Having studied some of the more general phenomena observable with in-plane magnetized tips on the 1.5 ML Fe/W(110) stripe system we will now return to the question of residual domains. The aim is to observe the behavior of their bounding walls in addition to that of the domains themselves. In particular, the following issues will be scrutinized: (i) Will residual domains be further reduced in size in applied fields higher than 400 mT? (ii) Will they be eventually switched, and if so, which field strengths will they be able to sustain? Experimenting with in-plane magnetized tips in applied perpendicular magnetic fields brought about two major results: Firstly, at increasing fields an increasing loss of in-plane sensitivity is observed which can be attributed to the action of the external field forcing the tip magnetization to rotate into its hard direction. Secondly, evidence was found that interactions due to the presence of the tip affected the stability of the residual domains at field values around $B = 800$ mT. Or, to put it another way, the measurement process proved to be influential on the result. This is, in general, a situation one wants to avoid.

So, searching for a non-intrusive way to observe residual domains in higher fields, we found *bare tungsten tips* without any ferromagnetic coating to be sensitive not to DL domains, but to domain walls. Again, before presenting the results obtained in the study of residual domains, I want to elucidate the contrast mechanism along the spectra obtained with these tips on the DL stripe system. Two spectral curves are plotted in Fig. 8.10(a). Again, the color code matches the boxes drawn in the dI/dU map (c) to indicate areas where the spectra have been averaged. Comparing the two curves, we find them nearly identical over almost the whole energetic range, which is not surprising since the W tip probes the *spin-averaged* electronic structure of the sample. However, in a small range close to the Fermi energy $E_{\mathrm{F}} = 0$ meV there are small but significant deviations between the two curves. This range, marked by a dashed box in (a), is presented in an enlarged view in (b). In the red curve we find (i) a small peak with a maximum at a bias of $U = +84$ mV which is absent in the green curve, and (ii) the more pronounced peak at $U = -67$ mV for the red curve is shifted by 10 mV towards higher bias for the green curve. Plotting the normalized difference of the two curves, (red − green)/(red + green) as a function of bias we obtain the white-dotted curve that shows at which biases the relative intensities exhibit extrema. The dI/dU maps shown in panel (c) and (d) correspond exactly to these values. They reveal the cause for the observed discrepancies: the red curve was measured above a domain, whereas the green curve belongs to a domain wall. The observed contrasts must not be attributed to spin polarized tunneling. Instead, it is the spin averaged electronic structure of
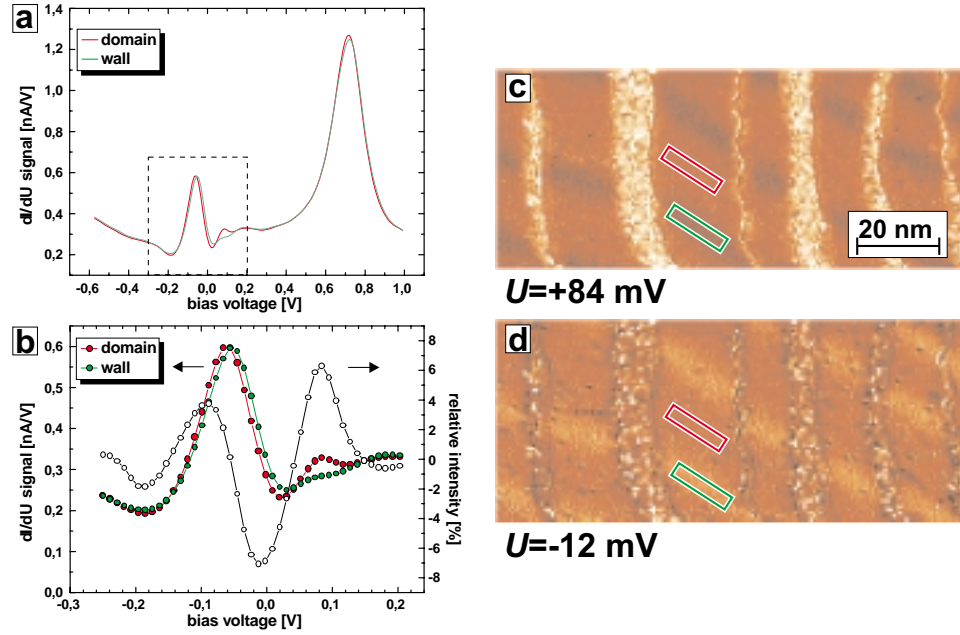
Figure 8.10: **(a)** Spectra measured using a bare tungsten tip. Color codes correspond to the boxes in **(c)** and **(d)**, respectively. Only in the limited voltage range marked by the dashed box the curves deviate significantly. A zoom into this range is plotted in **(b)**. The white-dotted curve indicates the signal asymmetry.

the DL stripes being locally modified by the presence of a domain wall that is giving rise to the signal. A possible explanation for such a behavior may be the well known effect of magnetostriction. We do not observe a contrast from one wall to the next as was the case in the spin polarized experiments with in-plane magnetized tips. All walls show up either dark (c) or bright (d), depending on the chosen bias. Nevertheless, we can exploit the observed effect in our study of residual domains, now with a tip which is free of any stray fields.

Fig. 8.11 presents maps of the dI/dU signal taken with a bare tungsten tip at a bias of $+50$ mV in applied fields as indicated. A few dislocation lines are visible in the left stripe indicating the [001] direction. At zero field (a) numerous domain walls can be recognized as dark lines oriented along [1$\bar{1}$0]. Note that a significant number of the walls deviate from this direction by an angle $\alpha = 13.2° \pm 0.5$; this effect was already discussed in Chapter 7. It is also noteworth that the presence of dislocation lines shows no significant influence on the initial domain wall formation. We find a density of walls much higher than observed in Fig. 8.1. The higher density and hence much shorter domains presumably result from the larger terrace widths on substrate #2 as compared to substrate #1, allowing for wider DL stripes, albeit the nominal coverage is only slightly higher here. The walls are
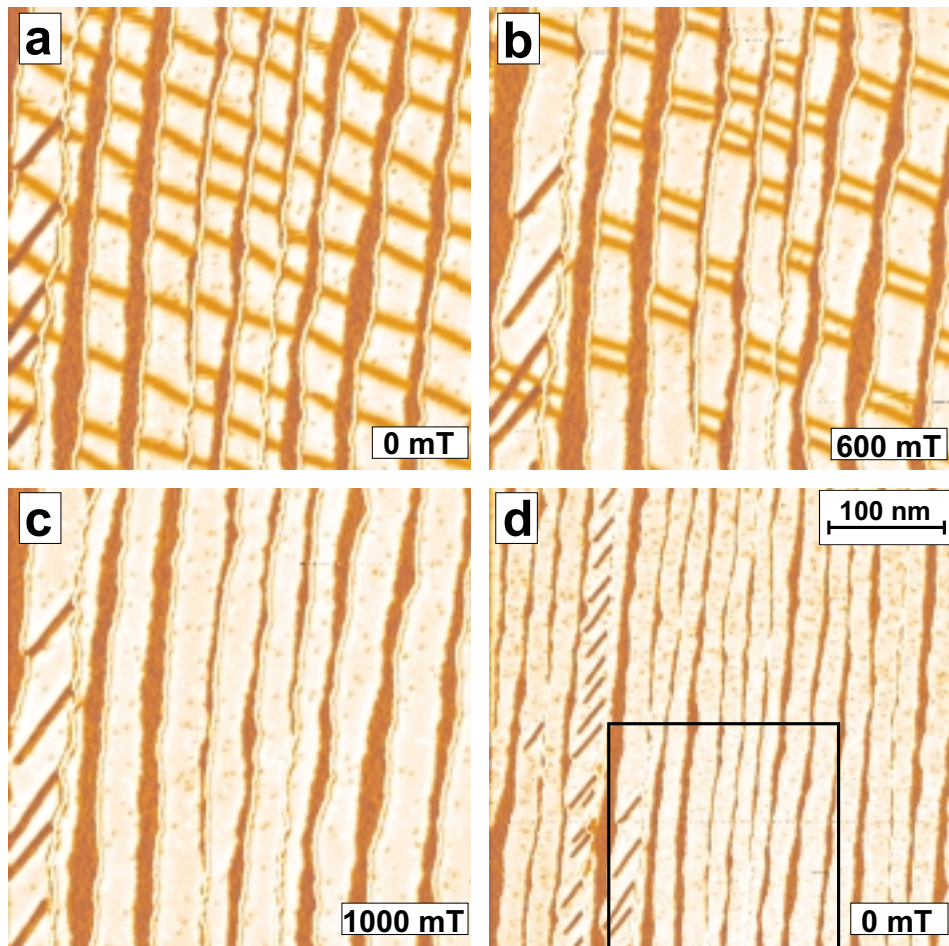
Figure 8.11: Maps of the dI/dU signal taken with a bare tungsten tip without ferromagnetic coating. A few dislocation lines can be seen in the left stripe, indicating the [001] direction. At the chosen bias voltage numerous domain walls appear as dark lines in **(a)**. With increasing field **(b)** they form pairs bounding the invisible residual domains. **(c)** At 1000 mT no wall is left. In the zoom-out view **(d)** the scan area of **a–c** is marked by a box. With the field removed no wall is found left, indicating an annihilation of the residual domains due to the sole action of the applied field. Tunneling paramenters: $I = 0.5$ nA, $U = +50$ mV.
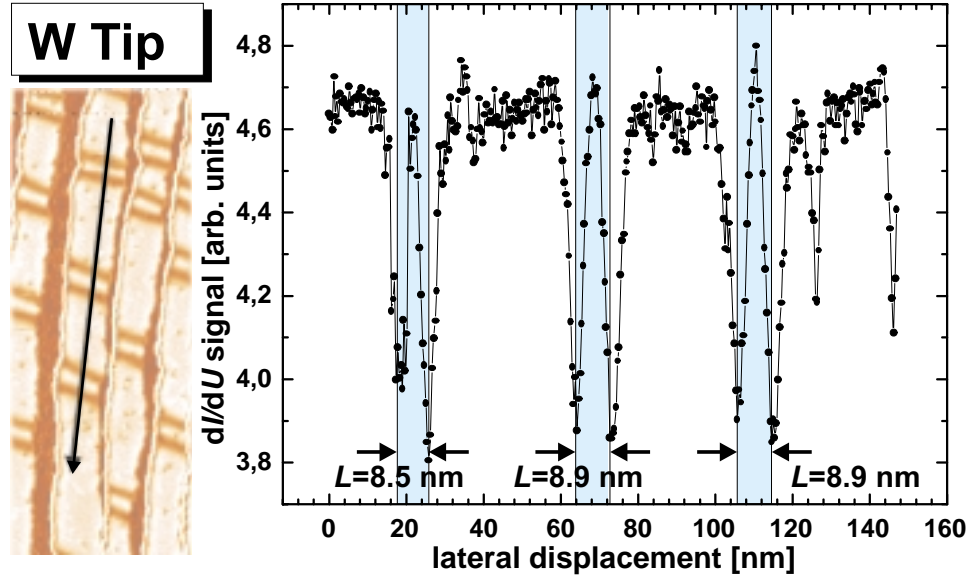
Figure 8.12: Lengths of residual domains as measured by a bare W tip.

roughly spaced equidistantly. At 600 mT all walls have formed pairs. In the broad stripe containing the dislocation lines and in the narrow stripe next to it the number of walls is reduced; obviously, the dislocation lines destabilize the residual domains now being stressed. In all other stripes the number of walls is constant except for single walls that may have moved out of the scan range. Panel (c) shows no wall left in an applied field of 1000 mT. In the zoom-out view (d), taken after removal of the external field, a box is drawn to indicate the area of the previous scans. Neither inside nor outside the box residual domains are left over. This is in contrast to the results obtained in a similar experiment using a ferromagnetic tip at 800 mT where no residual domains were found inside the initial scan range but numerous of them could be observed outside the range after field removal (not shown here). Using the bare W tip the annihilation of the residual domains can clearly be attributed to the action of the applied field. We can thus give an estimate of the critical field necessary to break up residual domains and to drive the sample fully to saturation as 800 mT $<$ B_c $<$ 1000 mT. This value is two orders of magnitude smaller than the exchange field estimated in Sect. 8.1.3. It is thus suggested that the reorientation of the residual domains takes place by a mechanism which has not yet been considered. Indeed, recently performed micromagnetic simulations [109] indicate that the spins eventually rotate through the hard in-plane direction [001], cf. Fig. 8.13.

The sizes of residual domains as obtained with bare tungsten tips are displayed in Fig. 8.12. The values are determined, as was done in Fig 8.5, by measuring the distance between the centers of the bounding walls. We
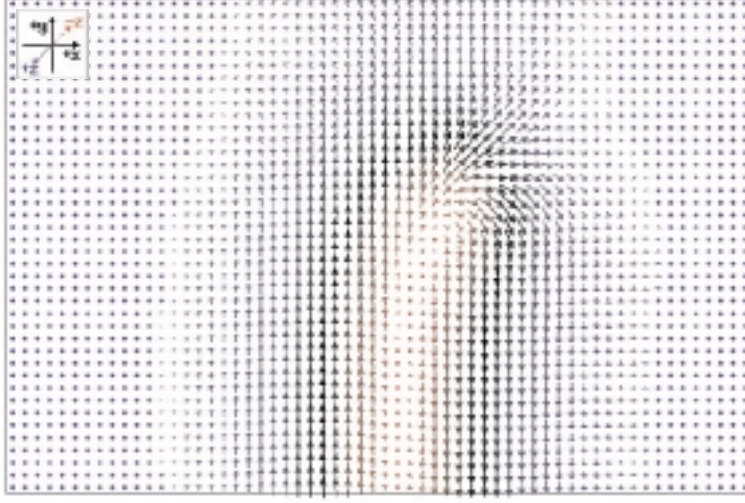
Figure 8.13: Computer simulated residual domain breakdown at $B = 900$ mT. The spin rotation eventually occurs via the hard in-plane direction [001] ($= x$). Parameters: Exchange stiffness $A = 1.5 \times 10^{-11}$ Jm^{-1}, saturation magnetization $M_s = 2 \times 10^6$ Am^{-1}, anisotropy constants $K_{u1} = 3.5 \times 10^6$ Jm^{-3} (out-of-plane), $K_{u2} = -2.5 \times 10^6$ Jm^{-3} (in-plane). Plot by courtesy of A. Kubetzka [109].

find $L_{rd} = 8.75 \pm 0.3$ nm for the W tip, which is about 35% larger than the value measured with an out-of-plane magnetized tip. Taking the distance of the atomic rows along [001] into account (two layers), $a_W/2 = 1.579$ Å, we conclude that a 180° spin rotation is observed over 52±5 atomic rows, i.e. on average 3.4° per row.

8.3.1 Domain Properties

From comparing the results of the complete hystersis loop to the experiment using the bare W tip we find that the lengths of the domains are much shorter for the latter case, and hence the density of domain walls much greater. The hysteresis loop was measured on substrate #1 while the experiments with the W tip were performed on substrate #2, and we recall the different terrace widths of the substrates, 9 nm and 25 nm on average, respectively. Since the nominal coverage in the experiments was about equal ($\Theta = 1.75 \pm 0.1$ ML) the conclusion can be drawn that the terrace width, in determining the stripe width for a given nominal coverage, plays a decisive role for the average domain length, and this should affect the remagnetization process. The influence of roughness at the descending step edges is expected to scale inversely with the stripe width, also the number of constrictions or even disruptions per unit stripe length will certainly be much higher in narrow stripes, giving rise to an increased pinning of domain walls. The latter parameters can be controlled to a large degree by appropriate growth conditions such as the temperature during growth and anneal, and orien-

tation of the substrate miscut. Growth at elevated temperatures provides considerably smoother stripe edges while growth at room temperature with subsequent annealing (cf. Fig. 7.3) leads to stripes much more reminiscent of the initial island morphology. In the latter type domain wall movement is more impeded, and a higher coercivity than in smooth stripes is expected.

The results shown in Fig. 8.11 clearly indicate that the length of domains is greatly reduced ($l \approx 25 - 60$ nm) as compared to the case of the narrower stripes. Fig. 8.9 shows an intermediate average value of $l \approx 100$ nm with a large distribution at a slightly lower nominal coverage. Very recent experiments on closed or nearly closed DL films confirm the described trend to shorter domains at higher coverages on substrate #2 leading eventually to a qualitatively different pattern of domains extending across numerous DL stripes in $[1\bar{1}0]$ direction (not elaborated here). As a consequence of shorter domains we find a much higher density of domain walls. On field application, the densely spaced walls encounter fewer pinning centers and hence exhibit an enhanced mobility; also, they have to travel much shorter distances to form pairs than in narrow stripes with longer domains like on substrate #1. On the other hand, the longer the distance to travel for the walls the higher the probability for *domain creation* to occur as a concurrent mechanism of magnetization reversal. The few events observed so far allow only a rough estimate of the nucleation field value, 50 mT$< B_{\mathrm{n}} < 150$ mT. In the case of densely spaced walls domain creation is very unlikely as long as residual domains are not destroyed and has not been observed yet.

Summarizing, we find a two-stage process leading to saturation. The first stage is characterized by domain wall motion with the mobility of the domain walls strongly determined by structural conditions of the stripe system such as terrace width, Fe stripe width (coverage), smoothness, density of constrictions. Also, the experimental temperature will influence the wall mobility. Depending on the particular domain length domain creation may occur as a concurrent remagnetization mechanism the probability of which increases with increasing domain length and reduced wall mobility. The first step is concluded when all remaining domain walls have formed pairs confining a residual domain. At the temperature of our experiment this state is reached at a field strength of $B \approx 400$ mT in the narrower stripes. If the applied field is not increased any further the residual domains will, on decrease of the field, provide intact nuclei of oppositely magnetized domains. In the case of short domains this process can be expected to be reversible to a large degree.

The second step requires an annihilation of the residual domains occuring at field strengths as high as 800 mT$< B_{\mathrm{s}} < 1000$ mT. This process is highly irreversible. In samples with densely spaced walls this should be observable in the hysteresis loop as a kink since the walls with the residual domains trapped between them occupy a considerable fraction of the overall DL area. On the other hand, in samples exhibiting long domains with few domain

walls the effect is certainly too small to be observed in a hysteresis loop; only SP-STM provides the ultrahigh spatial resolution required to observe the emergence and annihilation of residual domains in this case.

Two different shapes of hysteresis loops can be expected for the two types of samples. If the applied field does not exceed the critical value for residual domain annihilation the loop will be much narrower in wide stripes than in narrow stripes, with smaller values for coercivity and remanence. Concerning the saturated state, the arguments given may lead to the peculiar situation that, if hysteresis loops are acquired by spatially averaging methods, an apparent saturation field of about 400 mT may be found for the case of long domains, and the remaining residual domains will be overlooked easily. In samples exhibiting densely spaced walls a saturation field twice as high may be determined if the contribution of residual domain breaking to the overall magnetization can be detected.

The shape of the hysteresis loop posterior to full saturation will depend on the details of the re-nucleation process which has not been observed yet. It appears possible that the narrow stripes may end up with a higher wall density and thus shorter domains than the wide stripes since domain creation is more likely in narrow stripes as compared to the wider stripes. Reduced wall mobility favours enhanced domain creation.

8.3.2 Outlook

It remains open for further investigations to observe the highly interesting process of initial nucleation after a total annihilation of all residual domains. How will it start? Where will it start? At which field value? How many newly created walls are required to eventually establish wall motion as the leading process in the magnetization reversal of the stripes? What will the domain structure look like? Will a state of uniform chirality reoccur?

Another field widely open to systematic studies is given by a variation of the coverage. Especially in the low DL coverage regime new effects may arise from interactions with the in-plane magnetized ML stripes. Last but not least, the ML system itself deserves a closer investigation in its own right by means of SP-STS.

Chapter 9

Summary

Magnetic imaging based on spin polarized scanning tunneling microscopy
has become a mature technique. The resolution achievable is two orders of
magnitude better than that of the most advanced methods currently in use.
Magnetic sensitivity at the ultimate, atomic scale has already been demon-
strated by imaging the antiferromagnetic superstructure of a single atomic
layer Mn on W(110) [29]. In the present work, focus has been put on the the-
ory of SP-STM and SP-STS, on the instrumental setup required for magnetic
imaging, and on domain imaging of a system of Fe nanowires on W(110)
exhibiting a highly complex magnetic structure with a "nanoscale spatial
switching of anisotropy" [94]. Both the domain structures magnetized in the
film plane and perpendicular to the plane have been imaged in great detail.
The magnetic images provide clear, strong contrasts. The main problem
of earlier attempts to achieve spin polarized tunneling, namely to separate
topographic and magnetic information, can be regarded resolved. More-
over, by measuring the sample topography in constant current mode and the
magnetization map by a method derived from tunneling spectroscopy, simul-
taneously but separately pixel by pixel, we can now correlate structural and
magnetic properties at a resolution that allows to identify single adsorbate
molecules as pinning centers of domain boundaries.

SP-STS can be performed in strong applied magnetic fields. For the first
time, it was possible to observe a complete hysteresis loop at the nanometer
scale and to identify the complex processes that are responsible for hysteretic
behavior: domain wall motion, domain nucleation and domain annihilation.
While the processes themselves are well known on the scale of microns it
was a surprise to find them at a scale where magnetism, for a long time,
was supposed to become simple. We found a residual domain of enhanced
stability in saturation fields which is the outcome of a $360°$ spin rotation.
Due to its small size of 6×6 nm^2 it can be observed only by SP-STS.

Spin polarized imaging has become possible by combining two essential
ingredients: tunneling tips coated by thin magnetic films, and a spectroscopic

approach. By choosing the appropriate material for tip coating one can determine at will a sensitivity of the tip to either the in-plane or out-of-plane magnetization component of the sample, or to both simultaneously. Once an understanding of the domain structure under study had been achieved, even non-magnetic tips could be used to study certain magnetic phenomena. In the future, various other tip coating materials may be tried out for the sake of their particular properties, e.g. magnetic hardness, extraordinary high spin polarization, high Curie or spin reorientation temperatures, etc. It has been demonstrated that Fe coated tips also allow room temperature spin polarized imaging of the antiferromagnetic Cr(001) surface [110] using the in-plane component. On the other hand, antiferromagnetic materials for tip coating are of special interest since they promise to allow imaging without any influence of tip induced stray fields. Recently, first encouraging experiments have been performed with such tips.

Imagining future experimental setups, it would be desirable to have the ability to control the azimuthal orientation of the tip magnetization in order to maximize magnetic in-plane contrasts. A vector field SP-STM would provide the freedom to apply magnetic fields in any desired direction. A variable temperature SP-STM would allow to study thermal energy dependent phase transition phenomena.

The new method of SP-STM in conjunction with state-of-the-art epitaxial methods to produce well ordered magnetic structures of two, one, and zero dimensions opens new vistas for the study of magnetic phenomena like exchange bias, tunneling magneto-resistance, or spin injection. When Feynman gave his landmark talk in 1959 calling for an exploration of the nano-world [111] he repeatedly highlighted the important role of adequate microscopes: "The problems ... can be greatly helped if our ability to see what we are doing, and to do things on an atomic level, is ultimately developed." It took another twenty years until the STM was invented, providing exactly the ability to look into the world of atoms, and to arrange atoms at will to write letters or to build atomic corrals fencing in electrons, and we can watch them interfering as quantum mirages [112]. Now the STM can also be used to routinely visualize the spin information of the tunneling electrons. It has come within reach to achieve what was envisioned by Pierce [17] in 1988: to image the magnetic moments of individual atoms at the surface of a sample.

Bibliography

[1] P. Grünberg, R. Schreiber, and Y. Pang, Phys. Rev. Lett. **57**, 2442 (1986).

[2] M.N. Baibich, J.M. Broto, A. Fert, F. Nguyen Van Dau, and F. Petroff, Phys. Rev. Lett. **61**, 2472 (1988).

[3] G. Binasch, P. Grünberg, F. Saurenbach, and W. Zinn, Phys. Rev. B **39**, 4828 (1989).

[4] R. Wood, IEEE Trans. Magn. **36** No. 1, 36 (2000).

[5] F. J. Himpsel, J.E. Ortega, G.J. Mankey, and R.F. Willis, Advances in Physics **47**, 511 (1998).

[6] E. Betzig, J.K. Trautmann, R. Wolfe, E.M. Gyorgy, and P.L. Flinn, Appl. Phys. Lett. **61**, 142 (1992).

[7] J. Unguris, M.R. Scheinfein, M.H. Kelley, A. Gavrin, R.J. Celotta, and D.T. Pierce, in *Handbook of Microscopy*, VCH Verlagsgesellschaft, 735-749 (1997). See also http://physics.nist.gov/Divisions/Div841/Gp3/epg_files/sempa.html.

[8] J. Kirschner, in: A. Howie, and U. Valdré, *Surface and Interface Characterization by Electron Optical Methods*, New York, London, Plenum Press (1998).

[9] P.R. Aitchison, J.N. Chapman, V. Gehanno, I.S. Weir, M.R. Scheinfein, S. McVitie, and A. Marty, J. Magn. Magn. Mater. **223**, 138 (2001).

[10] A. Hubert and R. Schäfer, *Magnetic Domains*, Springer, Berlin, Heidelberg, New York (1998) p. 54–66.

[11] P. Fischer, G. Schütz, G. Schmahl, P. Guttmann, D. Raasch, Z. Phys. **101**, 313 (1996).

[12] M. Köhler, T. Schweinbröck, T. Schmidt, J. Zweck, G. Bayreuther, P. Fischer, G. Schütz, T. Eimüller, P. Guttmann, and G. Schmahl, J. Appl. Phys. **87**, 6481 (2000).

[13] A. Scholl, J. Stöhr, J. Lüning, J.W. Seo, J.Fompeyrine, H. Siegwart, J.-P. Locquet, F. Nolting, S. Anders, E.E. Fullerton, M.R. Scheinfein, and H.A. Padmore, Science **287**, 1014 (2000).

[14] F. Nolting, A. Scholl, J. Stöhr, J.W. Seo, J. Fompeyrine, H. Siegwart, J.-P. Louquet, S. Anders, J. Lünig, E.E. Fullerton, M.F. Toney, M.R. Scheinfein, and H.A. Padmore, Nature **405**, 767 (2000).

[15] M. Dreyer, M. Kleiber, A. Wadas, and R. Wiesendanger, Phys. Rev. B. **59**, 4273 (1999).

[16] U. Hartmann, Magnetisch abbildende Rastersondenverfahren, in *Magnetische Schichtsysteme in Forschung und Anwendung*, ed. by Forschungszentrum Jülich GmbH, Jülich (1999), p. B7.1-30.

[17] D.T. Pierce, Physica Scripta **38**, 291 (1988).

[18] R. Wiesendanger, H.-J. Güntherodt, G. Güntherodt, R.J. Gambino, and R. Ruf, Phys. Rev. Lett. **65**, 247 (1990).

[19] R. Wiesendanger, D. Bürgler, G. Tarrach, A. Wadas, D. Brodbeck, D. Güntherrodt, R.J. Gambino, and R. Ruf, J. Vac. Sci. Technol. B **9**, 519 (1991).

[20] R. Wiesendanger, I.V. Shvets, D. Bürgler, G. Tarrach, H.-J. Güntherrodt, J.M.D. Coey, and S. Gräser, Science **255**, 583 (1992).

[21] J.A. Stroscio, D.T. Pierce, A. Davies, R.J. Celotta, and M. Weinert, Phys. Rev. Lett. **75**, 2960 (1995).

[22] M. Bode, M. Getzlaff, and R. Wiesendanger, Phys. Rev. Lett. **81**, 4256 (1998).

[23] S.F. Alvarado and P. Renaud, Phys. Rev. Lett. **68** 1387 (1992).

[24] R. Jansen, M.C.M.M. van der Wielen, M.W.J. Prins, D.L. Abraham, and H. van Kempen, J. Vac. Sci. Technol. B **12**, 2133 (1994).

[25] M.W.J. Prins, R. Jansen, H. van Kempen, Phys. Rev. B **53**, 8105 (1996).

[26] W. Wulfhekel and J. Kirschner, Appl. Phys. Lett. **75**, 1944 (1999).

[27] W. Wulfhekel, H.F. Ding, W. Lutzke, G. Steierl, M. Vásquez, P. Marín, A. Hernando, J. Kirschner, Appl. Phys. A **72**, 463 (2001).

[28] S. Blügel, M. Weinert, and P.H. Dederichs, Phys. Rev. Lett. **60**, 1077 (1988).

[29] S. Heinze, M. Bode, A. Kubetzka, O. Pietzsch, X. Nie, S. Blügel, and R. Wiesendanger, Science **288**, 1805 (2000).

[30] Stefan Heinze, *First-Principles Theory of Scanning Tunneling Microscopy Applied to Transition-Metal Surfaces*, Ph.D. thesis, University of Hamburg, Germany, (2000).

[31] M. Bode, M. Hennefarth, D. Haude, M. Getzlaff, and R. Wiesendanger, Surf. Sci. **432**, 8 (1999).

[32] T. Asada, G. Bihlmayer, S. Handschuh, S. Heinze, Ph. Kurz, and S. Bluegel, *First-principles theory of ultrathin magnetic films*, Journal of Physics C **11**, 9347 (1999).

[33] J. Tersoff, and D.R. Hamann, Phys. Rev. B **31**, 805 (1985).

[34] G. Binnig and H. Rohrer, Helv. Phys. Acta **55**, 726 (1982).

[35] J. Bardeen, Phys. Rev. Lett. **6**, 57 (1961).

[36] J. Tersoff, and D.R. Hamann, Phys. Rev. Lett. **50**, 1998 (1983).

[37] N. García, C. Ocal, and F. Flores, Phys. Rev. Lett. **50**, 2002 (1983).

[38] C.J. Chen, Phys. Rev. B **42**, 8841 (1990).

[39] R. Wiesendanger, *Scanning Probe Microscopy and Spectroscopy*, Cambridge University Press, Cambridge (1994), p. 113.

[40] Matthias Bode, *Strukturelle und lokale elektronische Eigenschaften ultradünner Eisenfilme auf W(110)*, Ph.D. thesis (1996), University of Hamburg, Germany.

[41] R. J. Hamers, Ann. Rev. Phys. Chem. **40**, 531 (1989).

[42] D. Wortmann, S. Heinze, Ph. Kurz, G. Bihlmayer, and S. Blügel, Phys. Rev. Lett. **86**, 4132 (2001).

[43] O. Pietzsch, A. Kubetzka, D. Haude, M. Bode, and R. Wiesendanger, Rev. Sci. Instrum. **71**, 424 (2000).

[44] Omicron Multiprobe *MX*.

[45] Omicron Variable Temperature STM.

[46] Oxford Instruments, Cambridge CB4 4WZ, United Kingdom.

[47] Ceramic Products, Palisades Park, NJ 07650, USA.

[48] S.H. Pan, S. Behler, M. Bernasconi, and H.-J. Güntherodt, Bull. Am. Phys. Soc. **37**, 167 (1992).

[49] Ch. Witt, U. Mick, M. Bode, and R. Wiesendanger, Rev. Sci. Instrum. **68**, 1455 (1997).

[50] M. Bode, M. Hennefarth, D. Haude, M. Getzlaff, and R. Wiesendanger, Surf. Sci. **432**, 8 (1999).

[51] Staveley Sensors, East Hartford, CT 06108, USA.

[52] Ch. Wittneven, R. Dombrowski, S.H. Pan, and R. Wiesendanger, Rev. Sci. Instrum. **68**, 3806 (1997).

[53] S.H. Pan, E.W. Hudson, and J.C. Davis, Rev. Sci. Instrum. **70**, 1459 (1999).

[54] W. Allers, A. Schwarz, U.D. Schwarz, and R. Wiesendanger, Rev. Sci. Instrum. **69**, 221 (1998).

[55] Lakeshore Cryotronics, Westerville, OH 43081, USA.

[56] A. Kubetzka, Diploma thesis, University of Hamburg, Germany (1999).

[57] Vacuum Generators, Hastings, E Sussex, England.

[58] M. Getzlaff, M. Bode, S. Heinze, R. Pascal, and R. Wiesendanger, J. Magn. Magn. Mat. **184**, 155 (1998).

[59] E. Weschke, C. Schüssler-Langeheine, R. Meier, A.V. Fedorov, K. Starke, F. Hübinger, and G. Kaindl, Phys. Rev. Lett. **77**, 3415 (1996).

[60] D. Li, C.W. Hutchings, P.A. Dowben, C. Hwang, R.T. Wu, M. Onellion, A.B. Andrews, and J.L. Erskine, J. Magn. Magn. Mater. **99**, 85 (1991).

[61] D. Li, C.W. Hutchings, P.A. Dowben, C. Hwang, R.T. Wu, M. Onellion, A.B. Andrews, and J.L. Erskine, J. Appl. Phys. **70**, 6565 (1991).

[62] E. Vescovo, O. Rader, T. Kachel, U. Alkemer, and C. Carbone, Phys. Rev. B **47**,13899 (1993).

[63] D. Li, P.A. Dowben, J.E. Ortega, and F.J. Himpsel, Phys. Rev. B **49**, 7734 (1994).

[64] M. Donath, B. Gubanka, and F. Passek, Phys. Rev. Lett. **77**, 5138 (1996).

[65] M. Bode, R. Pascal, M. Getzlaff, and R. Wiesendanger, Acta Phys. Pol. A **93**, 273 (1998).

[66] M. Bode, M. Getzlaff, S. Heinze, R. Pascal, and R. Wiesendanger, Appl. Phys. A **66**, S121 (1998).

[67] M. Farle and K. Baberschke, Curie Temperatures and Magnetic Anisotropies as a Function of Growth Conditions for Gd(0001)/W(110), in M. Donath, P.A. Dowben, and W. Nolting (eds.), *Magnetism and Electronic Correlations in Local Moment Systems: Rare Earth Elements and Compounds*, Singapore, New Jersey, London, Hong Kong, World Scientific (1998).

[68] G. André, A. Aspelmeier, B. Schulz, M. Farle, and K. Baberschke, Surf. Sci. **326**, 275 (1995).

[69] H.J. Elmers and U. Gradmann, Appl. Phys. A **51**, 255 (1990).

[70] P. M. Tedrow and R. Meservey, Phys. Rev. B **7**, 318 (1973).

[71] B. Sincović, E. Shekel, and S. L. Hulbert, Phys. Rev. B **52** 8696 (1995).

[72] M. Bode, R. Pascal, M. Getzlaff, and R. Wiesendanger, Acta Physica Polonica A **93**, 273 (1998).

[73] U. Gradmann and G. Waller, Surf. Sci. **116** 539 (1982).

[74] P.J. Berlowitz, J.-W. He and D.W. Goodmann, Surf. Sci. **231**, 315 (1990).

[75] J. Kolaczkiewicz and E. Bauer, Surf. Sci. **450**, 106 (2000).

[76] H.J. Elmers, J. Hauschild, H. Höche, U. Gradmann, H. Bethge, D. Heuer, and U. Köhler, Phys. Rev. Lett. **73**, 898 (1994).

[77] H. Bethge, D. Heuer, Ch. Jensen, K. Reshöft, and U. Köhler, Surf. Sci. **331-333**, 878 (1995).

[78] C. Jensen, K. Reshöft, and U. Köhler, Appl. Phys. A **62**, 217 (1996).

[79] D. Sander, R. Skomski, C. Schmidthals, A. Enders, and J. Kirschner, Phys. Rev. Lett. **77** 2566 (1996).

[80] M. Bode, R. Pascal, and R. Wiesendanger, J. Vac. Sci. Technol. A **15**(3), 1285 (1997).

[81] M. Przybylski and U. Gradmann, Phys. Rev. Lett. **59**, 1152 (1987).

[82] J. Hauschild, H.J. Elmers, and U. Gradmann, Phys. Rev. B **57**, R677 (1998).

[83] H.J. Elmers, J. Hauschild, and U. Gradmann, J. Magn. Magn. Mater. **177-181**, 827 (1998).

[84] J. Hauschild, U. Gradmann, and H.J. Elmers, Appl. Phys. Lett. **72**, 3211 (1998).

[85] H.J. Elmers, J. Hauschild, and U. Gradmann, Phys. Rev. B **59**, 3688 (1999).

[86] *Crystal Data*, edited by J.D.H. Donnay and H.M. Ondik (National Bureau of Standards), Gaithersburg, MD, 1973.

[87] L.Z. Mezey, and J. Giber, Jpn. J. Appl. Phys. **21**, 1569 (1980).

[88] H.J. Elmers, J. Hauschild, and U. Gradmann, J. Magn. Magn. Mat. **198-199**, 222 (1999).

[89] H.J. Elmers, J. Hauschild, and U. Gradmann, J. Magn. Magn. Mat. **221**, 219 (2000).

[90] D. Stünkel, Z. Physik **176**, 207 (1963).

[91] H.J. Elmers, J. Hauschild, H. Fritsche, G. Liu, U. Gradmann, and U. Köhler, Phys. Rev. Lett. **75**, 2031 (1995).

[92] H.J. Elmers, G. Liu, and U. Gradmann, Phys. Rev. Lett. **63**, 566 (1989).

[93] C.H. Back, C. Würsch, D. Kerkmann, and D. Pescia, Z. Phys. B **96**, 1 (1994).

[94] N. Weber, K. Wagner, H.J. Elmers, J. Hauschild, and U. Gradmann, Phys. Rev. B**55**, 14121 (1997).

[95] T. Dürkop, H.J. Elmers, and U. Gradmann, J. Magn. Magn. Mat. **172**, L1 (1997).

[96] H.J. Elmers, J. Magn. Magn. Mat. **185**, 274 (1998).

[97] A. Kubetzka, O. Pietzsch, M. Bode, and R. Wiesendanger, Phys. Rev. B **63**, 140407 (2001).

[98] O. Pietzsch, A. Kubetzka, M. Bode, and R. Wiesendanger, Phys. Rev. Lett. **84**, 5212 (2000).

[99] P. Bruno, Phys. Rev. Lett. **83**, 2425 (1999).

[100] M. Bode, O. Pietzsch, A. Kubetzka, and R. Wiesendanger, Phys. Rev. Lett. **86**, 2142 (2001).

[101] H.J. Elmers, Magnetismus dünner Filme, in *Magnetische Schichtsysteme in Forschung und Anwendung*, ed. by Forschungszentrum Jülich GmbH, Jülich (1999), p. B1.41.

[102] Soon C. Hong and A.J. Freeman, Phys. Rev. B **38**, 12156 (1988).

[103] E. Ising, Z. Physik **31**, 253 (1925).

[104] W. Nolting, *Quantentheorie des Magnetismus* Vol. 1, Teubner, Stuttgart (1986), p. 229.

[105] see Ref. [10], p. 217.

[106] M. Jullière, Phys. Lett. **54A**, 225 (1975).

[107] J. C. Slonczewski, Phys. Rev. B **39**, 6995 (1989).

[108] R. Wiesendanger, M. Bode, and M. Getzlaff, Appl. Phys. Lett. **75**, 124 (1999).

[109] A. Kubetzka, to be published.

[110] M. Kleiber, M. Bode, R. Ravlić, and R. Wiesendanger, Phys. Rev. Lett. **85**, 4606 (2000).

[111] R. Feynman, *There's Plenty of Room at the Bottom*, talk given on December 29th 1959. Sci. Eng. **23**, 22 (1960). See also the transcript at http://www.zyvex.com/nanotech/feynman.html.

[112] H.C. Manoharan, C.P. Lutz, and D.M. Eigler, Nature **403**, 512 (2000).

Appendix A

Original Publications and Conference Contributions

Journal Papers

1. M. Bode, M. Getzlaff, A. Kubetzka, R. Pascal, O. Pietzsch, and R. Wiesendanger, *Temperature dependent surface electronic structure of a local-moment magnet: Tb(0001)*, Phys. Rev. Lett. **83**, 3017 (1999).

2. O. Pietzsch, A. Kubetzka, D. Haude, M. Bode, and R. Wiesendanger, *A low-temperature UHV scanning tunneling microscope with a split-coil magnet and a rotary motion stepper motor for high spatial resolution studies of surface magnetism*, Rev. Sci. Instr. **71**, 424 (2000).

3. O. Pietzsch, A. Kubetzka, M. Bode, and R. Wiesendanger, *Real-space observation of dipolar antiferromagnetism in magnetic nanowires by spin-polarized scanning tunneling spectroscopy*, Phys. Rev. Lett. **84**, 5212 (2000).

4. S. Heinze, M. Bode, A. Kubetzka, O. Pietzsch, X. Nie, S. Blügel, and R. Wiesendanger, *Real-space imaging of two-dimensional antiferromagnetism on the atomic scale*, Science **288**, 1805 (2000).

5. M. Bode, O. Pietzsch, A. Kubetzka, S. Heinze, and R. Wiesendanger, *Experimental evidence for intra-atomic non-collinear magnetism at thin film probe tips*, Phys. Rev. Lett. **86**, 2142 (2001).

6. A. Kubetzka, O. Pietzsch, M. Bode, and R. Wiesendanger, *Magnetism of nanoscale Fe islands studied by spin-polarized scanning tunneling spectroscopy*, Phys. Rev. B **63**, 140407 (2001).

7. O. Pietzsch, A. Kubetzka, M. Bode, and R. Wiesendanger, *Magnetic Hysteresis observed at the Nano-Scale by Spin Polarized Scanning Tunneling Spectroscopy*, Science (submitted).

Conference Proceedings

1. M. Bode, M. Getzlaff, A. Kubetzka, O. Pietzsch, and R. Wiesendanger, in: *Magnetoelektronik*, ed. VDI-Technologiezentrum, Düsseldorf (2000) p. 165: "Observation of in-plane and out-of-plane Magnetization in magnetic nanostructures".

2. M. Bode, O. Pietzsch, A. Kubetzka, and R. Wiesendanger, *Imaging magnetic nanostructures by spin-polarized scanning tunneling spectroscopy*, J. Electr. Spectr. Relat. Phenom. **114-116**, 1055 (2001).

3. M. Bode, O. Pietzsch, A. Kubetzka, and R. Wiesendanger, *Spin-polarized scanning tunneling spectroscopy on Fe-nanowires*, Appl. Phys. A **72**, S 149 (2001).

Conference Contributions

Talks

28.03.00 O. Pietzsch, A. Kubetzka, M. Bode, and R. Wiesendanger, Regensburg, Germany (Spring Conference, Deutsche Physikalische Gesellschaft): *Direkte Visualisierung von dipolar antiferromagnetisch gekoppelten Nanostreifen mittels spinpolarisierter Rastertunnelmikroskopie.*

03.10.00 O. Pietzsch, A. Kubetzka, M. Bode, and R. Wiesendanger, Boston, USA (47th International Symposium, American Vacuum Society, and NANO 6): *Direct Visualization of Magnetic Nanowires by Spin Polarized Scanning Tunneling Spectroscopy.*

29.03.01 O. Pietzsch, A. Kubetzka, M. Bode, and R. Wiesendanger, Hamburg, Germany (Spring Conference, Deutsche Physikalische Gesellschaft): *Ummagnetisierung von Fe-Nanodrähten beobachtet mit dem Rastertunnelmikroskop.*

Posters

25.03.99 O. Pietzsch, A. Kubetzka, M. Bode, and R. Wiesendanger, Münster, Germany (Spring Conference, Deutsche Physikalische Gesellschaft): *Neues UHV-Tieftemperatur-STM mit Magnetkryostat.*

16.03.00 O. Pietzsch, A. Kubetzka, M. Bode, and R. Wiesendanger, Montreux, Switzerland (18th General Conference of the Condensed Matter Division, European Physical Society): *Direct Visualization of Dipolar Antiferromagnetically coupled Nanowires by Spin Polarized Scanning Tunneling Spectroscopy.*

Danksagung

Mein Dank gilt an erster Stelle den beiden Kollegen, mit denen ich in den vergangenen Jahren täglich aufs Engste zusammengearbeitet habe: Dr. Matthias Bode und André Kubetzka. Eine Anlage so komplex wie die im Labor 013 kann kaum von einer einzelnen Person bedient werden. Aber es geht um viel mehr als um die Organisierung einer vielschichtigen praktischen Arbeit. Es ist das kontinuierliche Gespräch, der ständige Austausch von Gedanken, Ideen, gegenseitigen Anregungen, Kritik und Ansporn – die kreative und produktive Atmosphäre, die ich in unserer Zusammenarbeit erfahren konnte, und die für eine fruchtbare Arbeit so unerlässlich ist. Die Ergebnisse, die ich in dieser Schrift vorstellen konnte, sind vor allem Resultat dieser gemeinsamen Arbeit.

Prof. Dr. R. Wiesendanger hat mit großer Weitsicht auf die jetzt erzielten Ergebnisse hin geplant und die entsprechende instrumentelle Ausstattung bereitgestellt. Ich bin ihm sehr dankbar, dass ich unter diesen hervorragenden Bedingungen zunächst meine Diplomarbeit und nun auch die vorliegende Arbeit anfertigen konnte.

Stefan Heinze hat uns bei einem nicht ganz unwichtigen Experiment die Augen geöffnet: "Streifen seht ihr? Streifen sind gut!" Aber auch ohne dies wäre er in diese Danksagung geraten: Niemand kann einen so gut aufmuntern und motivieren, wenn es mal Schwierigkeiten gibt.

Der Gruppe R möchte ich meinen Dank für die gute Arbeitsatmosphäre und die ständige Bereitschaft zur gegenseitigen Unterstützung aussprechen. Und danke auch für die Kuchenberge. Mampf!

Ein besonderer Dank gilt den Kollegen der mechanischen Werkstatt unter der Leitung von Herrn Benecke und Herrn Schmidt, die beim Bau des Mikroskops und vieler wichtiger Komponenten hervorragende Arbeit geleistet haben. In alten Zeiten sprach man von "goldenen Händen", wenn Arbeiter sich Fähigkeiten angeeignet hatten, die man nur in langen Jahren der Erfahrung und der Liebe zum Beruf erwerben kann. Dass es die goldenen Hände heute noch gibt, hat uns Peter Czernicki mehrfach bewiesen.

In den zum Glück überwundenen Zeiten der Helium-Knappheit hat Wolfang Hatje so manches wichtige Experiment ermöglicht, indem er uns fast aus dem Nichts doch noch eine Kanne des kostbaren Tranks herbeizauberte. Ich möchte ihm danken, dass er für uns so manche Extra-Meile gegangen ist.

Als ich mich im Wintersemester 1989/90 nach zwanzigjähriger Berufstätigkeit in das Abenteuer Physik-Studium stürzte, hatte ich das unwahrscheinliche Glück, auf Torsten Prietz und Sven Mildahn zu treffen, die mich davon abhielten, nach dem ersten Semester alles hinzuschmeißen: "Kein Problem, wir schleppen dich schon mit durch." Ihnen verdanke ich, dass ich

schließlich selber laufen lernte. Aus der Übungsgruppe entstand eine bis heute anhaltende Freundschaft.

Besonders herzlich bedanken möchte ich mich bei meiner Freundin Ulla Baxmann, die in den letzten Monaten mit Engelsgeduld meine Launen ertragen und mich trotz eigener großer beruflicher Belastung in jeder Hinsicht unterstützt hat. Aber da ist noch ein Grund zum Danke-Sagen: Bei unserer ersten Begegnung war sie studentische Gutachterin der Hans-Böckler-Stiftung, und sie schrieb mir das Gutachten, das mir das wunderbare Jahr in Berkeley ermöglichte. Danke, Ulla.